Experimental and first-principles study of point defects, domain walls, and point-defect / domain-wall interactions in ferroelectric oxides

THÈSE N^O 6931 (2016)

PRÉSENTÉE LE 4 FÉVRIER 2016
À LA FACULTÉ DES SCIENCES ET TECHNIQUES DE L'INGÉNIEUR
LABORATOIRE DE THÉORIE ET SIMULATION DES MATÉRIAUX
ET
LABORATOIRE DE CERAMIQUE

ÉCOLE POLYTECHNIQUE FÉDÉRALE DE LAUSANNE

POUR L'OBTENTION DU GRADE DE DOCTEUR ÈS SCIENCES

PAR

Anand CHANDRASEKARAN

acceptée sur proposition du jury:

Prof. V. Michaud, présidente du jury
Prof. N. Marzari, Prof. D. Damjanovic, directeurs de thèse
Prof. P. Paruch, rapporteuse
Prof. B. Meyer, rapporteur
Prof. A. Pasqurello, rapporteur

EPFL

ÉCOLE POLYTECHNIQUE
FÉDÉRALE DE LAUSANNE

Suisse
2016

To my parents...

Acknowledgements

Abstract

Ferroelectric oxides, such as lead zirconate titanate, have proved invaluable due to their excellent dielectric and piezoelectric properties. These classes of materials possess a large electric polarization below the Curie temperature. Regions of the crystal lattice having different directions of polarization are separated by nano-scale interfaces known as domain walls. These interfaces, which can be moved by electric and mechanical fields, are not only important for electromechanical properties but they also exhibit unique structural and electronic properties that may be exploited through novel application in nanoelectronics and photovoltaics.

The mobility of domain walls is strongly dependent on the defect chemistry of the material due to defect-domain wall interactions. Indeed, aliovalent doping of these materials has been used to tune the properties of ferroelectric oxides for specific applications. In this work, we investigate the origin of the so-called "hard" and "soft" behavior in lead zirconate titanate. Experimental evidence suggests that small concentrations of donor dopants (such as niobium) results in enhanced domain wall motion while doping with acceptor dopants (such as iron) leads to an inhibited domain wall response. The microscopic origin of this phenomena is best investigated using first-principles simulations of the atomistic properties of defects and domain wall in these materials to bring to light novel structural and electronic properties.

First, we show that polar defect complexes are likely to exist in both acceptor-doped and undoped $PbTiO_3$. These defects and defect associates are attracted to 180° domain walls and cause pinning of such interfaces. Donor- doped materials, on the other hand, do not show the presence of polar defect complexes. A closer investigation of the 180° domain wall in $PbTiO_3$ reveals the presence of a "Bloch" component of polarization at the domain wall. In other words, due to polarization rotation, there exists a ferroelectric phase *within* the domain wall itself. We characterize the strain dependence of this phenomena and calculate the piezoelectric properties of such domain walls.

A complete study of domain walls in $PbTiO_3$ also entails looking closer at the properties of the ferroelastic "head-to-tail" 90° domain boundary. We show the presence of an asymmetry in the variation of the lattice parameter across the domain wall. This asymmetry is verified using high resolution aberration corrected electron microscopy. We look at the energy landscape of oxygen vacancies in the vicinity of these walls to explain the pinning effect in terms of random-bond and random-field defects.

Next we look at the electronic properties of the recently discovered charged domain walls. We characterize the band bending phenomena in 90° head-to-head and tail-to-tail domain wall in $PbTiO_3$. We then look at the long range effects of clusters of oxygen vacancies in $BaTiO_3$;

especially in terms of the formation of 180° tail-to-tail domain wall.

In parallel to the first priciples work, we also prepared high quality samples of PZT 50/50 with different concentrations of donor dopant. We characterized the microstructure and hysteresis loops as a function of donor dopant concentration. Based on experimental observations and ab initio calculations we propose ideas on the origins of hardening and softening in PZT.

Key words: Ferroelectric, domain walls, first-principles, defects, hard PZT, soft PZT

Résumé

Les oxydes ferroélectriques tels que le titano-zirconate de plomb, se sont révélés inestimables de part leurs excellentes propriétés diélectriques et piézoélectriques. Cette classe de matériaux possède une valeur élevée de la polarisation en-dessous de la température de Curie. Certaines régions du cristal ayant différentes directions de polarisation sont séparées, à l'échelle nanométrique, par des interfaces connues sous le nom de parois (ou mur) de domaine. Ces interfaces, qui peuvent être déplacées par des champs électriques et mécaniques, sont non seulement importantes pour les propriétés électromécaniques mais possèdent également une structure et des propriétés électroniques uniques qui peuvent être exploitées d'une façon nouvelle en nanoélectronique ou en photovoltaïque.

La mobilité des parois de domaine est fortement dépendante de la chimie des défauts du matériau, du fait des interactions entre défaut et paroi de domaine. En effet, un dopage aliovalent de ces matériaux a déjà été utilisé pour mettre au point les propriétés des oxydes ferroélectriques dans le cas d'applications spécifiques. Dans le travail présenté ici, nous examinons l'origine des comportements appelés "dur" et "doux" dans le titano-zirconate de plomb. Des expériences suggèrent que de petites concentrations de dopants donneurs (tels que le niobium) entraînent un mouvement accru des parois de domaine tandis que le dopage avec des accepteurs (tels que le fer) conduit à une inhibition de la réponse des parois de domaine. L'origine microscopique de ce phénomène est étudiée de façon optimale en utilisant des simulations ab initio des propriétés atomiques des défauts et des parois de domaine dans ces matériaux, afin de mettre en lumière de nouvelles structures et propriétés électroniques.

Pour commencer, nous montrons que des complexes polaires constitués de défauts, sont susceptibles d'exister aussi bien dans le $PbTiO_3$ non dopé que dans celui dopé par des accepteurs. Ces défauts et les complexes qu'ils forment, sont attirés à des parois de domaine à 180° et empêchent de telles interfaces de bouger. Au contraire, les matériaux dopés par des donneurs ne révèlent pas la présence de tels complexes polaires. Un examen plus poussé des parois de domaine à 180° dans le $PbTiO_3$ montre la présence d'une composante dite de "Bloch" dans la polarisation, au niveau de la paroi de domaine. En d'autres termes, du fait de la rotation de la polarisation, il existe une phase ferroélectrique *à l'intérieur* de la paroi de domaine elle-même. Nous caractérisons la dépendance de ce phénomène en fonction de la déformation et calculons les propriétés piézoélectriques de telles parois de domaine.

Une étude complète des parois de domaine dans le $PbTiO_3$ nécessite également une observation plus poussée des propriétés de l'interface de domaine à 90° "tête-bêche". Nous montrons

Résumé

la présence d'une asymétrie dans la variation du paramètre de maille à travers la paroi de domaine. Cette asymétrie est vérifiée par microscopie électronique à haute résolution avec correction des aberrations. Nous étudions l'énergétique des lacunes en oxygène à proximité de ces parois pour expliquer l'effet de blocage en termes de défauts de type liaisons aléatoires et champ aléatoire.

Ensuite nous étudions les propriétés électroniques des parois de domaine chargées, découvertes récemment. Nous caractérisons le phénomène de flexion des bandes dans les parois de domaine à 90°, face-à-face et dos-à-dos, dans le $PbTiO_3$. Nous observons ensuite les effets à longue portée des amas de lacunes d'oxygène dans le $BaTiO_3$, particulièrement en terme de formation des parois de domaine à 180° dos-à-dos.

En parallèle des études ab initio, nous avons également préparé des échantillons de haute qualité de PZT 50/50 avec différentes concentrations de dopant donneur. Nous avons caractérisé la microstructure et les cycles d'hystérèse en fonction de la concentration de dopant donneur. Nous proposons un certain nombre d'idées sur l'origine du durcissement et de l'adoucissement dans le PZT, basées sur les observations expérimentales ainsi que les calculs ab initio.

Key words: Ferroelectric, domain walls, first-principles, defects, hard PZT, soft PZT

Contents

Contents

List of Figures

List of Tables

1 Introduction - ferroelectrics

Ferroelectric materials show a spontaneous electric polarization that can be reversed/altered by the application of an external electric field [1]. The most important class of ferroelectric materials are the ABO_3 perovskites such as $BaTiO_3$ and $PbTiO_3$. At high temperatures such oxides possess a non-polar simple cubic structure that can be described on average, as having the metal A located on the corners of the cube, the metal B at the cube center and the O atoms at the cubic faces. At lower temperatures, a phase transition occurs where the positively charged B atom is displaced off-center with respect to the surrounding negatively charged oxygen octahedra. Hence a phase transition has occurred from a paraelectric phase to a ferroelectric phase possessing a spontaneous electric polarization. A classic example of a ferroelectric is $PbTiO_3$ which exhibits a high temperature centrosymmetric cubic phase and low temperature tetragonal phase as shown in Fig. 1.1.
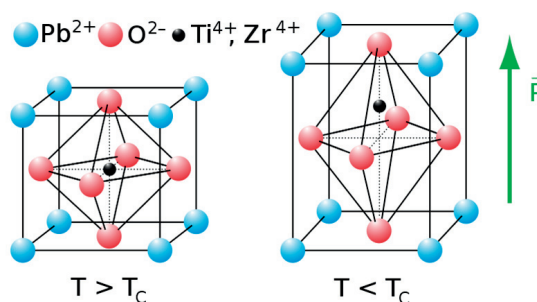
Figure 1.1: Structure of $PbTiO_3$/tetragonal PZT (lead zirconate titanate) at different temperatures.

In the ferroelectric phase, these materials are non-centrosymmetric and exhibit piezoelectricity. Ferroelectric materials also show variation of spontaneous polarization with temperature hence they are also pyroelectric. This relation is best illustrated in Fig. 1.2.

The first observation of the ferroelectric phenomenon was reported by Valasek [2] in Rochelle salt in 1921 but there was not much development in this field until a few decades after. The need for higher-dielectric constant capacitors spurred the development of the first ferroelectric
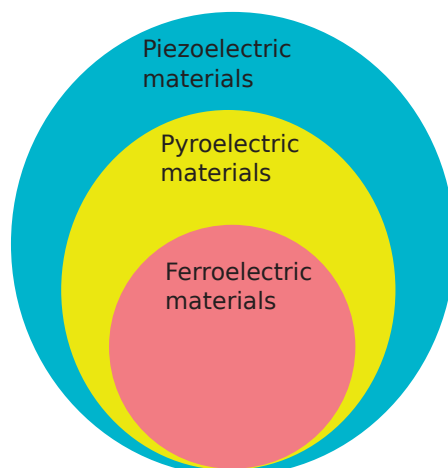
Figure 1.2: The relation between piezoelectric, pyroelectric and ferroelectric materials.

ceramics during the 1940s [3]. The elucidation of the ferroelectric properties of $BaTiO_3$ by Gray in 1949 [4] attracted much interest. The electrical aligning ("poling") of domains within grains of polycrystalline $BaTiO_3$ ceramics allowed the electromechanical properties of these ceramics to be exploited for industrial and commercial applications. Soon after, ferroelectric activity was reported in other oxides such as $KNbO_3$, $LiNbO_3$, $LiTaO_3$ and $PbTiO_3$ [5].

1.1 Applications

Ferroelectric materials have wide-ranging applications for modern technology from Ferroelectric Random Access Memories (FeRAM) to high dielectric constant capacitors. They have been extensively used for piezoelectric applications; exploiting both direct and converse piezoelectric effects. Using the direct effect, they have been put to use in accelerometers, gas lighters, microphones, photo-flash actuators and pressure sensors. The converse piezoelectric effect has been exploited in devices such as loud speakers, camera shutter, buzzers, ink jet printer etc. They have also been used as high frequency transformers and resonant devices such as transducers, sonar, ultrasonic welders, filters etc.

1.2 Lead zirconate titanate

Lead zirconate titanate (PZT) is the most widely used ferroelectric ceramic for piezoelectric application. It is a solid solution of $PbTiO_3$ and $PbZrO_3$. It possess many advantageous properties like

1. High electromechanical coupling coefficient

2. A relatively high Curie temperature (T_c) which allows operation at temperatures up to 200^oC

3. Wide range of dielectric constants

4. Capability to form solid-solutions with different compositions

5. Easily poled

6. Ability to sinter at low temperature

The phase diagram of PZT is shown in Fig. 1.3 and is summarized by Jaffe Cook and Jaffe in their treatise on piezoelectric ceramics [6]. The end-members of this binary solid solution are $PbTiO_3$ and $PbZrO_3$ which possess a tetragonal ferroelectric phase and an orthorhombic antiferroelectric phase at room temperature respectively.
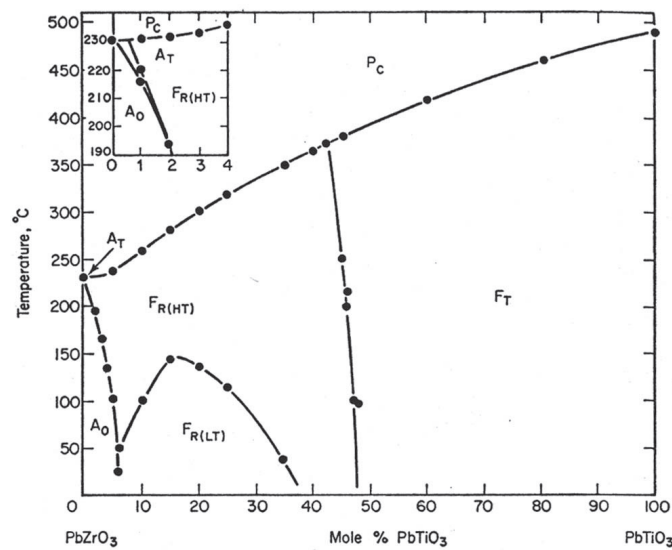
Figure 1.3: Phase diagram of Lead zirconate titanate [6]. F_T is the ferroelectric tetragonal phase, $F_{R(HT)}$ is the high temperature rhombohedral ferroelectric phase, $F_{R(LT)}$ is the low temperature rhombohedral ferroelectric phase. A_O is antiferroelectric orthorhombic phase. P_C is the paraelectric cubic phase.

Replacement of the Ti^{4+} ion with the Zr^{4+} ion in $PbTiO_3$ results in a reduction in c/a ratio and is accompanied by a decrease in T_C. The transition between the rhombohedral region and the tetragonal region occurs at around 52% Zr and 48% Ti. This area, known as the the morphotropic phase boundary (MPB), possesses enhanced piezoelectric and dielectric properties and it has been the subject of intense study over the years. It was assumed for many years that, in this region, there was a co-existence of both tetragonal and rhombohedral phases, depending on the homogeneity of the powders [7–10] and grain size [11]. The observation of a monoclinic phase in the MPB region using high-resolution synchrotron X-ray powder by Noheda *et al.* [12] sparked a debate about the nature of the MPB. Using first-principles derived effective Hamiltonian methods, Bellaiche *et al.* demonstrated the stability of this monoclinic phase in disordered PZT [13]. The dependence of diffraction patterns on the domain structure makes this issue difficult to resolve [14]. In 2007, it was suggested that

presence of nanodomains of tetragonal and rhombohedral symmetry produced monoclinic-like diffraction pattern due to coherence effects [15, 16]. However, the same authors later claimed that the internal symmetry of the domains was indeed monoclinic [17].

1.3 Domain walls

In the ferroelectric state, different regions of the crystal (known as domains) show the presence of any one of the degenerate directions of polarization. The interfaces separating two such regions are known as domain walls. Domain walls exist to minimize electrostatic and elastic energy due to formation of spontaneous polarization and strain. Fousek and Janovec made a list of different types of domain walls possible, based on electrostatic and elastic compatibility conditions [18]. Hence, there exist only two types of domain walls in tetragonal materials: 90° domain walls and 180° domain walls. 180° domain walls are purely ferroelectric and thus do not interact with stress fields. 90° domain walls are both ferroelectric and ferroelastic and they respond to both electric and stress fields. The dielectric and piezoelectric response of poled bulk ferroelectric ceramics is dominated by the motion of 90° domain walls. However, the controlled growth and nucleation of both 90° and 180° domain walls may be important for nano-scale applications such as in FeRAM.

The properties arising from a single domain ferroelectric material are referred to as the intrinsic properties of the material while the contributions from domain walls/grains are labeled as extrinsic properties of the materials [19–22]. Reports by Artl *et al.* indicated that domain wall motion is indeed extremely important for the dielectric and piezoelectric ceramics such as PZT [23–26]. Experiments suggest that the domain wall contribution to the dielectric and piezoelectric properties may be as large as 50% [27].

However, due to their unique properties, domain walls are now seen as functional interfaces for applications in a broader technological spectrum. For example, the presence of switch-able ferroic order within 180° domain walls of $PbTiO_3$ was reported recently by Wojdeł and Íñiguez [28]. Strongly charged domain walls have been discovered which show the presence of quantum 2D electron gas [29, 30] reminiscent of the phenomenon observed in $LaAlO_3$/$SrTiO$ heterostructures [31, 32]. Charge separation in such domain walls has been exploited not only in oxides [33] but also in organometallic perovskites; it is thought that domain wall engineering is a promising approach to optimize photovoltaic devices [34]. More and more effort is being devoted to achieve the controlled growth and functionalization of such domain wall interfaces, especially in thin films [35–37]. More details about domain walls, especially from the first-principles perspective, are discussed in Sec. 3.4

1.4 Hard and soft ferroelectrics

Electromechanical hardening and softening of ferroelectric materials through the addition of dopants is a key technique to tailor their properties [38–41]. The best known examples are

hard and soft $Pb(Zr,Ti)O_3$. Hardening can be caused by the addition of acceptor dopants and softening by the addition of donor dopants [6]. Hard ferroelectric materials exhibit strong aging (see later), a pinched hysteresis loop, lower electromechanical coupling coefficients, low dielectric losses, and moderate conductivity. Soft materials on the other hand exhibit large electromechanical coefficients, a square hysteresis loop, weak aging, low conductivity, and high dielectric losses. The hysteresis loop for undoped, hard and soft PZT are shown in Fig. 1.4. While the mechanisms of softening are still not clearly understood, there is a relatively better understanding of the phenomenon of hardening. It is thought that dopants (and their associated defects) affect properties through their interactions with domain walls, rather than influencing the intrinsic properties. The properties of acceptor-doped hard materials have been attributed to inhibited domain wall movement [42–45, 45–50], whereas softening is thought to be associated with highly mobile domain walls.
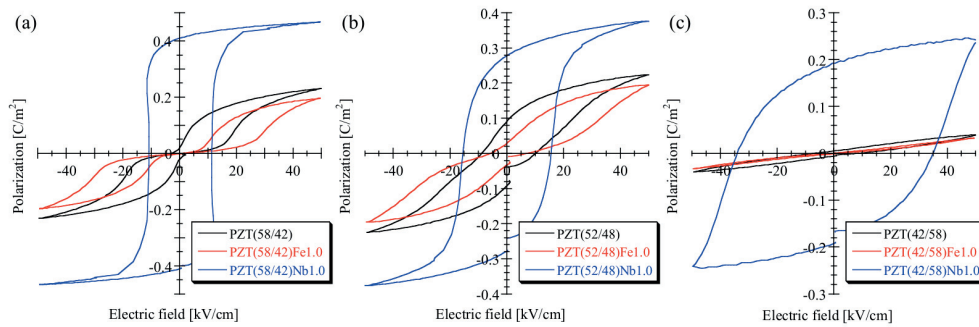
Figure 1.4: Room temperature ferroelectric hysteresis loops for representative undoped, hard and soft PZT ceramics in (a) rhombohedral, (b) MPB and (c) tetragonal regions [51].

There have been many experimental observations regarding the so called "aging" of hard acceptor-doped ferroelectric materials, starting from the reports of Carl and Härdtl in 1977 [52]. It was observed that many of the properties of acceptor-doped PZT ceramics change over time, with in particular the hysteresis loop becoming more pinched and more asymmetric. The reasons for this behavior can be threefold.

1. *Volume effect:* In this case defects occupy energetically preferred sites in the lattice and form anisotropic centers which favor a certain direction of spontaneous polarization. The defects behave as "random-field" defects. The volume effect has been recently studied by Ren and co-workers [45, 53] and has been referred to as a "symmetry-conforming" mechanism.

2. *Domain wall effect:* Here, the defects are thought to migrate to domain walls and remain fixed there in their positions [54, 55, 55, 56]. The defects behave as "random-bond" defects.

3. *Grain boundary effect:* During the sintering process there is a build-up of defects and surface charges at the grain boundaries which then affect the electromechanical response

of the material [46, 47, 57].

These scenarios involve different distances for charge displacement: over a unit cell (bulk effect), over a domain width (domain-wall effect) or over part of a grain or a crystal (interface effect). Although more than one mechanism may be at play, recent work seems to point to the bulk effect [58, 59] as the dominant mechanism. There is, in fact, EPR evidence for the coupling of acceptor dopants [60, 61] to oxygen vacancies and the alignment of this defect complex produces an internal field for which there is also experimental evidence [52, 62]. The presence of aging in single-domain acceptor-doped $BaTiO_3$ shows that the aging phenomena does not require the presence of grain boundaries [63].

One can also study the process of "deaging" to better understand the dynamics of defect/-domain interactions. Deaging is the process of reconstructing the domain structure in an aged sample by misaligning the defect associates. This can be accomplished, for example, by cycling with an electric field [52], quenching from a high temperature [64–66] or by illumination [55]. Deaging of hard PZT by electric fields is the best documented case [52, 67]. For a fixed amplitude of the applied field, the deaging time depends on the temperature and cycling field frequency and can be described as an Arrhenius-type process with a characteristic activation energy.

The properties of soft PZT, on the other hand, have been attributed to higher domain wall-mobility [6]. It is not clear why soft materials have higher domain-wall mobilities compared to those of undoped materials, and several hypothesis have been suggested. For instance, donor dopants are thought to compensate the effects of acceptor cations or lead vacancies that are naturally present in the undoped materials [6], thus preventing the formation of oxygen vacancies which are suspected to be responsible for pinning domain walls [56]. The possibility that lead vacancies reduce internal stresses in ceramics and make domain walls more mobile has also been suggested [40]. Last, there is a possibility that electron transfer between defects could minimize the space charge at domain walls, thereby increasing domain-wall mobility [68]. It is highly likely that positively charged donor defects are compensated by lead vacancies [69];however, it is yet unclear whether donor dopants form defect associates with these vacancies. If indeed these are formed, it is of interest to see whether these defect associates interact with the polarization at the vicinity of domain walls, to understand why such defects do not have the same role as acceptor-based complexes in hard materials.

2 Introduction to first-principles methodology

Density-functional theory (DFT) has been one of the most versatile and popular computational electronic-structure methods over the past few decades. It has been heavily utilized in the fields of condensed-matter physics, materials science, chemistry, and molecular biology. The main goal for any electronic-structure method is to obtain expectation values for different observables through approximations of the ground-state many body problem. For a given external potential V the Schrödinger equation

$$\hat{H}\Psi(r_1,...,r_N) = \hat{E}(r_1,...,r_N)\Psi \tag{2.1}$$

is an eigenvalue equation for the N-electron many-body wavefunction $\Psi(r_1,...,r_N)$, where the the Hamiltonian $\hat{H}$ is

$$\hat{H} = \hat{T}_e + \hat{V}_{n-e} + \hat{U}_{e-e} + W_{n-n} \tag{2.2}$$

Here, $\hat{T}_e$ is the electronic kinetic energy operator, $\hat{V}_{n-e}$ is potential energy operator from the Coulombic interactions of the nuclei with the electrons, $\hat{U}_{e-e}$ is the electrostatic repulsion of the electrons and W_{n-n} is the electrostatic (classical) repulsion of nuclei.

The first Hohenberg-Kohn theorem [70] showed that the ground state properties of a many-electron system are uniquely determined by the ground state electron density, reducing the problem from 3N spatial coordinates to 3 spatial coordinates. The second Hohenberg-Kohn theorem introduces a variational principle on the total energy functional

$$E[\rho] = E_{n-e}[\rho] + T[\rho] + E_{e-e}[\rho] = \int \rho(r)V_{n-e}(r)dr + F_{HK}[\rho] \tag{2.3}$$

through the introduction of the universal Hohenberg-Kohn functional $F_{HK}[\rho]$, that contains the many-body kinetic energy $T[\rho]$ and electron-electron interactions, E_{e-e}. The explicit form of this functional is unknown. The electron-electron interaction E_{e-e} can be decomposed into a combination of the Hartree/classical part and the non-classical part

$$E_{e-e}[\rho] = \frac{1}{2} \int \int \frac{\rho(r_1)\rho(r_2)}{r_{12}} dr_1 dr_2 + E_{ncl}[\rho] = J[\rho] + E_{ncl} \tag{2.4}$$

E_{ncl} is the non-classical contribution to the electron-electron interaction: it contains the self-interaction correction, and exchange-and-correlation terms.

Since, the second Hohenberg-Kohn theorem states that the ground state energy can be obtained variationally (i.e. the density that minimizes the total energy is the ground state density), we have that

$$E_0 = min_{\rho \to N}\left(F[\rho] + \int \rho(r)V_{n-e}dr\right) \tag{2.5}$$

where

$$F[\rho] = T[\rho] + J[\rho] + E_{ncl}[\rho] \tag{2.6}$$

In 1965 Kohn and Sham [71] proposed to approximate Eqn.2.6 by introducing the exact kinetic energy of a non-interacting reference system with the same density as the real, interacting one. The kinetic energy of this non-interacting ("Kohn-Sham") system is

$$T_S = -\frac{1}{2} \sum_i^N \langle \psi_i | \nabla^2 | \psi_i \rangle, \tag{2.7}$$

and

$$\rho_s(r) = \sum_i^N |\psi_i(r)|^2 = \rho(r) \tag{2.8}$$

where ψ_i are the orbitals of the non-interacting system. Since T_S is not the true kinetic energy

of the system, Kohn and Sham introduced the following decomposition of the $F[\rho]$

$$F[\rho] = T_S[\rho] + J[\rho] + E_{XC}[\rho] \tag{2.9}$$

where T_S and J are well defined, and E_{XC} is the exchange-correlation energy that is hence defined by subtraction as,

$$E_{XC}[\rho] = (T[\rho] - T_S[\rho]) + (E_{ee}[\rho] - J[\rho]) \tag{2.10}$$

The exchange and correlation energy E_{XC} is the term where everything that is unknown is pushed into. When the variational principle is applied to the total energy expression we obtain the Kohn-Sham equations,

$$\left[-\frac{1}{2}\nabla^2 + V_{tot}(r) \right] \psi_i = \epsilon_i \psi_i(r) \tag{2.11}$$

with

$$V_{tot}(r) = V_n(r) + V_H(r) + V_{xc}(r) \tag{2.12}$$

and where

$$V_n(r) = -\sum_I \frac{Z_I}{|r - R_I|} \tag{2.13}$$

is the electrostatic potential of ions with charge Z_I at position at R_I

$$\nabla^2 V_H(r) = -4\pi\rho(r) \tag{2.14}$$

and the exchange-correlation potential is

$$V_{xc}(r) = -\frac{\delta E_{xc}[\rho]}{\delta n}(r) \tag{2.15}$$

$$\rho(r) = \sum_i |\psi_i(r)|^2 \tag{2.16}$$

Eqn.2.11 is the single-particle Schrödinger equation which can be solved as a standard eigen-value problem. However, in order to determine the eigenfunctions, $\psi-i$ and the eigenvalues,ϵ_i, one has to first calculate the total potential V_{tot}(Eqn.2.12). From Eqn.2.14 and Eqn.2.15 we see that the Hartree potential V_H and the exchange-correlation potential V_{xc} depends on the density, ρ, which in turn depends on the unknown eigenfunctions, ψ_i. The presence of ρ in the Hamiltonian means that the Kohn-Sham equations have to be solved iteratively. The Kohn-Sham orbitals in the above equation do not have any physical significance, except the highest occupied orbital, which in an exact DFT formulation would equal the negative of the exact ionization energy.

2.1 Local Density Approximation (LDA)

As mentioned earlier, the exchange-correlation energy (E_{XC}) is in principle unknown. The local density approximation was the first approximate exchange-correlation functional. This approximation takes advantage of the properties of an uniform electron gas. An uniform electron gas is a system in which electrons move on a positive background charge distribution such that the total ensemble is neutral.

We approximate E_{XC} in the following way,

$$E_{XC}^{LDA}[\rho] = \int \rho(r)\epsilon_{XC}(\rho(r))dr \tag{2.17}$$

where $\epsilon_{XC}(\rho(r))$ is the exchange-correlation energy per particle of an uniform electron gas of density $\rho(r)$. The term $\epsilon_{XC}(\rho(r))$ is further decomposed into exchange and correlation contributions,

$$\epsilon_{XC}(\rho(r)) = \epsilon_X(\rho(r)) + \epsilon_C(\rho(r)) \tag{2.18}$$

The exchange part ϵ_X is defined as the exchange energy of an electron in a uniform electron gas of a particular density. The exact expression for non-interacting electrons was derived by Bloch and Dirac in the 1920's [72]

$$\epsilon_X = -\frac{3}{4}\left(\frac{3\rho(r)}{\pi}\right)^{1/3} \tag{2.19}$$

While no such expression is available for the correlation part of the uniform electron gas, ϵ_C, highly accurate numerical quantum Monte-Carlo simulations of the homogeneous electron gas have been performed by Ceperley and Alder [73]. Most local density approximations interpolate these accurate values and also reproduce the exactly known limiting behaviour. A few examples, using different analytic forms for ϵ_C are the interpolation of Vosko-Wilk-Nusair(VWN) [74], Perdew-Zunger (PZ81) [75], Cole-Perdew (CP) [76] and Perdew-Wang (PW92) [77].

The accuracy of the LDA for the exchange energy is typically within 10% while the correlation energy is generally overestimated by up to a factor of 2. However the correlation energy is much smaller in magnitude compared to the exchange energy. Also, the two errors typically cancel partially. LDA gives bond lengths of molecules and solids typically with a high accuracy of 1-2%.

2.2 Beyond LDA

The Generalized Gradient Approximation (GGA) not only takes into account the density $\rho(r)$ at a point r, but also includes the gradient of charge density $\nabla\rho(r)$ in order to account for the non-homogeneity of the true electron density. The GGA scheme corrects the over-binding observed in LDA. This effects is sometimes too large and GGA "softens" the bond in some cases. For example, in Sec. 3.5, we show that GGA functional are not suitable for ferroelectrics. Atomic and molecular total energies are improved, as are activation barriers for chemical reactions or hydrogen bonds. The PW91 formulation by Perdew and Wang [78] was the first reliable application of the GGA methodology. Perdew, Burke and Enzerhof reported their highly popular GGA scheme (PBE) in 1996 [79]. In 2008, Perdew *et al.* [80] introduced a revised PBE formulation that improves equilibrium properties of densely packed solids and their surfaces (PBEsol).

2.3 Periodic boundary conditions and Bloch's theorem

In order to solve the Kohn-Sham equations for a crystal one has to essentially handle an infinite number of interacting electrons moving in the static field of an infinite number of ions. However, ions in a perfect crystal are arranged in a regular periodic way. Therefore the external

potential felt by the electrons is also periodic (with periodicity equal to the dimensions of the unit cell).

Bloch's theorem uses the periodicity of a crystal to map the infinite number of one-electron wavefunctions into a finite number of continuous bands defined within the first Brillouin zone of the crystal. The wavefunction is written as the product of a periodic part and a plane-wave:

$$\psi_{ik}(r) = e^{ik.r} u_{ik}(r) \tag{2.20}$$

where u_{ik} is periodic:

$$u_{ik}(r + R) = u_{ik}(r) \tag{2.21}$$

As such, it can written as a linear combination of plane waves

$$u_{ik}(r) = \sum_G c_{ik,G} e^{i\vec{G}.\vec{r}} \tag{2.22}$$

where G are the reciprocal lattice vectors which are defined by $\vec{G}.\vec{R} = 2\pi n$ for all $\vec{R}$ where $\vec{R}$ is a lattice vector of the crystal and n is an integer.

The electronic wavefunctions at each k-point are now expressed in terms of a discrete plane wave basis set. In principle, this is an infinite Fourier series. However, the coefficients for the plane waves, $c_i, k + G$, each have a kinetic energy $(\hbar^2/2m)|k + G|^2$. The plane waves with smaller kinetic energy typically have a more important role that those with a very high kinetic energy. The introduction of a plane wave cutoff reduces the basis set to a finite size. By using Bloch's theorem, we calculate expectation values as sum over all bands and integrals over all $\vec{k}$ in the first Brilllouin Zone. This problem is dealt with by sampling the Brillouin zone at special sets of k-points. The two most common methods of k-point sampling are those of Chadi and Cohen [81] and Monkhorst and Pack [82].

2.4 Pseudopotentials

A plane wave basis set is inefficient at representing the electronic wavefunctions because a very large number is required to accurately describe the rapidly oscillating wavefunctions of electrons in the core regions. These oscillations maintain orthogonality between the core and valence electrons. However, most properties of a material just depend on the valence

electrons and are not affected by tightly bound core electrons. The pseudopotential is an effective potential that is constructed to replace the atomic all-electron potential such that the core states are eliminated and the valence electrons are described by pseudo-wavefunctions with significantly fewer nodes. This allows the pseudo-wavefunctions to be described by far few Fourier modes, thus making plane wave basis sets practical to use. Pseudopotentials are also constructed such that the scattering properties of the pseudo wavefunctions are identical to the scattering properties of the ion and core electrons.

2.5 Self-consistent calculations

A brief summary of the practical procedure to solve Eqns 1.12-1,17 is stated in this section. First, we specify the nuclear coordinates in such a way that we can calculate the nuclear potential V_n from Eqn 1.14. Next, we guess an electron density $\rho(r)$, in order to determine a preliminary approximation to the Hartree and exchange and correlation potentials. A simple approximation is to add up the densities corresponding to isolated atoms arranged in the specified coordinates. Hence, we now have the total potential V_{tot} to be used in Eqn 1.12. In our case, the Kohn-Sham equations are then solved numerically using the planewave representation. The solution gives us the new wavefunction ψ_i, which can then be used to construct a better estimate of the density ρ and total potential V_{tot}. The new density is usually mixed with the old density to improve convergence. This process is repeated until the new density matches the old density within a desired tolerance, at which point we say that we have achieved 'self-consistency'.

3 First-principles modelling of ferro-electrics

3.1   Electronic and Structural properties

One of the most direct applications of the first-principles methodology is to calculate the total energies as a function of the atomic coordinates, as the system undergoes distortions from some reference cubic perovskite structure. This may involve relative displacement of one of the ionic sublattices, linear combinations of such displacements (frozen phonons), or variations of lattice constants/angles. Once we obtain the energy landscape using this approach, we may then identify the distorted O K ground-state structure. The first LDA-DFT calculations on ferroelectrics were performed using the linear augmented plane-wave method [83–91] and soon after, ultrasoft pseudopotentials were also used [92–94]. Through these methods the ferroelectric instability was confirmed for $BaTiO_3$ [83, 84, 86, 92, 93], $KNbO_3$ [85, 87, 88, 90] and $PbTiO_3$ [84, 86, 93, 94].

3.2   Polarization and Born effective charges

The most important feature of a ferroelectric material is the presence of a spontaneous polarization $\vec{P}$. The macroscopic electric polarization of a crystal is often incorrectly defined as the dipole of a unit cell. In reality however, the quantity generally measured is the differential polarization with respect to a "reference state" of the same material. Owing to continuity, a polarization difference is equivalent to a macroscopic current, which can be computed as a bulk property [95]. Resta [96] emphasized that polarization is a quantum phenomenon and cannot be treated with a classical model , especially where delocalized electrons are present in the dielectric. In 1993, King-Smith and Vanderbilt [97] developed a direct way to compute the polarization difference between two structures by describing this property as a geometric quantum phase.

The first-order dependence of $\vec{P}$ upon atomic displacements and lattice strains is given by the dynamical Born effective charges (Z^*) and piezoelectric couplings. Anomalously large Born effective charges were observed for virtually all ferroelectric oxides [98]. In ABO_3 materials

this is due to borderline ionic-covalent bond between B and O atoms; Specifically, there is hybridization between the O $2p$ and B $3d/4d$ orbitals. Investigations of this phenomena have given insight into the origin of the ferroelectric instability and its relation to the long-range Coulomb interactions [99] and to many-body electron correlation effects [100, 101].

3.3 Defects and defect associates in oxides

Ferroelectric oxides usually contain a variety of vacancies that are formed during the growth processes. Ferroelectricity arises from a balance of short-range covalent interactions and long-range Coulombic interactions. The appearance of vacancies causes a partial loss in short-range interactions while charged vacancies also break long-range Coulombic interactions. Hence, vacancies have an important effect on many important properties such as polarization reversal, aging, fatigue etc. The pinning of domain walls by defects is further explored in Sec. 3.4.1. The characteristics of point defects in semiconductors and insulators is closely associated with their electronic structure. Park and Chadi [102], presented one of the earliest studies of the effect of oxygen vacancies on $PbTiO_3$. They observed the formation of tail-to-tail polarization in the case of an apical oxygen vacancies and observed that this effect was stronger when the vacancy was charged. In 2011, Yao and Fu [103] showed that, under oxygen-rich conditions, neutral oxygen vacancies have a large formation energy of 5.67 eV while doubly charged oxygen vacancies only had a formation energy of 0.28 eV. They also report that lead vacancies of different charge states had a formation energy of approximately 2 eV. The low formation energy of doubly charged oxygen vacancies in $PbTiO_3$ was verified using hybrid density-functional theory calculations by Shimada *et al.* [104]. Based on the defect-charge transition levels, they show that the oxygen vacancy acts as a double shallow donor over a wide range of Fermi energies under oxygen-poor conditions.

It is likely that certain vacancies exist as defect associates rather than isolated defects. For example, EPR measurements have shown that the oxygen vacancy is likely closely coordinated with iron and copper acceptor dopants in PZT [60, 61, 105]. Erhart *et al.* [106] used first-principles calculations to show that such type defect associates are preferentially aligned to the direction of spontaneous polarization. The presence of such polar defect associates is thought to be one of the causes of aging in hard ferroelectrics. It is not yet clear whether donor dopants form such defect associates. These issues are addressed in Chap. 5.8

3.4 Domain walls

One of the first attempts to model ferroelectric domain walls using first-principles based modelling was reported by Padilla *et al.* [107]. Using a first-principles effective Hamiltonian developed previously to study the phase transitions of $BaTiO_3$, the authors performed a Monte Carlo simulations to investigate the structure and energetics of 180° domain walls of (100) orientation in tetragonal $BaTiO_3$. Earlier phenomenological work indicated that domain walls

on the (110) plane had lower energy compared to those of (100) orientation. The authors also performed LDA calculations to show that the Ba-centered domain wall had an energy of 6.2 mJ/m^2 while Ti-centered walls had energies of 62.0 mJ/m^2. The calculations revealed that the domain wall entails only polarization reversal, instead of polarization rotation, with a domain wall thickness of 1.4 unit cells, or 5.6 Å. These results suggested a narrowing down the domain wall thickness from the experimental upper limit of 50 Å [108]. Earlier empirical calculation had suggested the thickness to be approximately 6.7Å [109]. Soon after, first-principles calculations were also performed by Pöykkö and Chadi [110] on 180° domain walls of PbTiO$_3$. They observed considerably higher 180° domain wall energies compared to that observed in BaTiO$_3$. This is to be expected since the energy difference between the ferroelectric and non-ferroelectric phase is much higher in the case in of PbTiO$_3$ compared to BaTiO$_3$ [83]. Very recently, Wojdeł and Íñiguez [28] showed the presence of Bloch component of polarization in 180° domain walls in PbTiO$_3$ (discussed in detail in Chap. 6). Using first-principles based model potentials [111], they verified the presence of a switchable ferroelectric phase within the domain wall. This is further supportive of the relative instability of the non-ferroelectric phase in PbTiO$_3$. The authors also investigated the temperature of the phase transition of this localized ferroic phase.

Meyer and Vanderbilt [112] were to the first to look at the structure of ferroelastic 90° walls in PbTiO$_3$ using first-principles calculations. Contrary to prior ideas [1], their calculations revealed fairly narrow domain walls of approximately 5 Å in length. This observation was in agreement with HRTEMs observation by Stemmer *et al.* [113], that reported a domain wall formation energy of 35 mJ/m^2 compared to a formation energy of 132 mJ/m^2 for the 180° domain wall. The barrier height for the movement of a 90° domain wall to a neighboring plane is also very small (approximately 1.6 mJ/m^2). Hence, at room temperatures, the domain wall is likely to be smeared out due to thermal fluctuations. Meyer and Vanderbilt also reported the presence of an electrostatic potential shift of 0.2 eV at the 90° domain wall. This is a result of a polarization discontinuity normal to the plane of the domain wall. The intrinsic asymmetry at 90° domain walls is described further in Chap.7.

The observation of steady conductivity at domain walls in BiFeO$_3$ by Seidel *et al.* [114] sparked intense efforts to take advantage of domain walls as nanoelectronic elements. Lubk *et al.* [115] looked closely at the electronic properties of these domain walls in BiFeO$_3$. They calculated the layer-by-layer density of states to see how the structural changes at the wall lead to changes of the band gap. The 180° domain wall showed the largest change in band gap by 0.2 eV. Just as in the case of Meyer and Vanderbilt, the step in potential was due to changes in the component of polarization normal to the domain wall [116]. Farokhipoor and Noheda [117] reported the presence of n-type defect states in BiFeO$_3$ due to oxygen vacancies. They suggest that the presence of these defect states result in two conduction-related phenomena. First, it allows thermally activated electrons from the defect state inside the band gap to be promoted to the conduction band. Second, defects accumulated at the domain wall reduce the Schottky barrier between the surface and the tip. In 2011, Guyonnet *et al.* [118] observed conductivity at the 180° domain walls of tetragonal PZT thin films and also attribute it to defect segregation

at these partially charged domain walls.

In 2013, Sluka *et al.* showed the presence of 2-dimensional electron gas at strongly charged domain walls in BaTiO$_3$. The observation of stable strongly charged head-to-head and tail-to-tail polarization was in itself extremely interesting due to the large formation energies [119]. The conductivity observed in head-to-head walls was several orders of magnitude higher than that of the bulk. The presence of strong metallic conductivity is likely due to the band bending close to the domain wall. However, conductivity was not observed at tail-to-tail domain walls and the authors attribute this to the presence of oxygen vacancies at such walls.

Hypothetical charged domain wall lattices were first investigated by Wu and Vanderbilt [120] using layers of donor and acceptor atoms to stabilize head-to-head and tail-to-tail 180° domain walls. A similar first-principles investigation was performed by Rahmanizadeh *et al.* [121] using fluorine/oxygen vacancies as donor at the tail-to-tail domain wall. At the resulting head-to-head domain wall, the additional electron is accommodated by the Ti d bands. They utilized the Hubbard parameter U to look at the possible electronic states at the charged domain wall. For vanishing U, they reported the presence of a broad conducting domain wall, while increasing U leads to localized Ti 3d states and the presence of an insulating, sharp domain wall.

3.4.1 Interaction with defects

It was long suspected that defects, especially oxygen vacancies, could pin domain walls and inhibit their movement [49]. As mentioned before, there is doubt as to whether defects exhibit random-bond or random-field pinning. Random-bond defects act symmetrically on the ferroelectric double well while random field defects result in an asymmetric variation of this double well. Random-field pinning implies that certain domain orientations are preferred over others because of the symmetry of the defect. Some experiments suggest that random field pinning is likely [45, 63], due to the formation of polar defect associates which align with the electric field. There has also been evidence of random bond pinning reported by Paruch *et al.* [122] through measurements of domain wall roughness. He and Vanderbilt demonstrated the lower formation energies of oxygen vacancies at 180° domain walls in PbTiO$_3$ [56]. However, they considered neutral oxygen vacancies and it has since been showed that doubly charged oxygen vacancies are much more likely [104]. Recently, Becher *et al.* [123] showed how coupling of oxygen vacancies with domain walls in SrMnO$_3$ altered the conductive properties of the wall with respect to the bulk. To our knowledge, there has been no report on the interaction of defects and defect associates with 90° domain walls. In Sec. 5.8 we examine the energy landscape of charged defects and defect associates in the vicinity 180° domain walls while in Chap. 7 we analyze the pinning of oxygen vacancies at 90° domain walls in terms of random-bond and random-field pinning.

Materials	Parameter	LDA	PBE	PBEsol	Experiment
$BaTiO_3$	a (Å)	3.93	3.99	3.96	3.98 [5]
	c (Å)	3.98	4.20	4.05	4.03 [5]
	c/a	1.011	1.052	1.023	1.012
$PbTiO_3$	a (Å)	3.86	3.84	3.88	3.90 [124]
	c (Å)	4.02	4.73	4.16	4.15 [124]
	c/a	1.041	1.230	1.072	1.064

Table 3.1: Cell parameters for lead titanate and barium titanate using different functionals.

3.5 Preliminary calculations

The lattice parameters and *c/a* ratio of lead titanate and barium titanate are compared for different functionals in Tab. 3.1. The equilibrium configuration is obtained by relaxing the cell degrees of freedom such that the components of the stress tensor all go to zero. Fitting the Birch-Murnaghan equation of state to the energy vs volume curve resulted in identical ground-state configurations.

The PBEsol ultrasoft pseudopotentials were taken from the pslibrary set developed by Prof. Andrea del Corso, SISSA, Italy. As shown, PBEsol was the best performing since it reproduced almost exactly the experimental lattice parameters and c/a ratio. LDA showed reasonable accuracy with respect to experiments while the PBE resulted in the presence of erroneously high tetragonality. In early stages of the thesis, LDA was utilized while we later switched to PBEsol. The different pseudopotentials used are shown in Tab. 3.2.

An effective Monkhorst-Pack k-point mesh of 8*8*8 per 5-atom cell and a plane wave cutoff of 60 Ry and a charge density cutoff 600 Ry are utilized for PBEsol. The plane wave cut-off is chosen to converge the forces on atoms to 10^{-4} Ry/bohr. The atoms were also allowed to relax until the forces were lower than 10^{-4} Ry/bohr. Unless stated otherwise, these were the parameters used for all calculations in this work.

Fig. 3.1 illustrates the ferroelectric instability in lead titanate. The centrosymmetric tetragonal structure possesses a significantly higher energy compared to the distorted structure. The two potential wells correspond to two types of relative displacements of the oxygen sublattice with respect to the lead sublattice. In $PbTiO_3$, one observes the effect of the partially covalent bonding between the lead and oxygen sublattices [84]. This type of interaction does not exist between barium and oxygen atoms in the case of $BaTiO_3$.

XC Approximation	Element	Pseudopotential
LDA	Pb	Pb.pz-rrkjus.UPF
	Ti	Ti.pz-rrkjus.UPF
	O	O.pz-rrkjus.UPF
	Nb	Nb.pz-rrkjus.UPF
	La	La.pz-rrkjus.UPF
	Fe	Fe.pz-rrkjus.UPF
PBEsol	Pb	Pb.pbesol-dn-rrkjus_psl.0.2.2.UPF
	Ba	Ba.pbesol-spn-rrkjus_psl.0.2.3.UPF
	Ti	Ti.pbesol-spn-rrkjus_psl.0.2.3.UPF
	O	O.pbesol-n-rrkjus_psl.0.1.UPF
	Nb	Nb.pbesol-spn-rrkjus_psl.0.3.0.UPF
	La	La.pbesol-spn-rrkjus_psl.0.2.3.UPF
	Fe	Fe.pbesol-spn-rrkjus_psl.0.2.1.UPF

Table 3.2: List of pseudopotentials used.
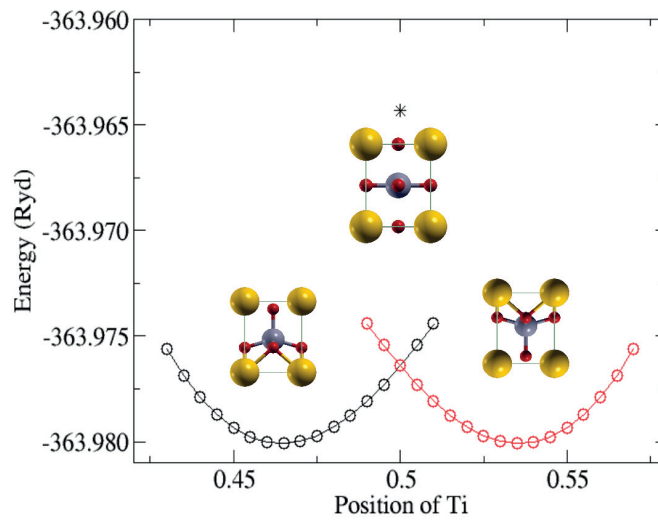
Figure 3.1: The double well potential energy landscape of lead titanate. Large yellow spheres represent lead, medium sized grey atoms are titanium and small red spheres are oxygen.

4 Preparation and characterization of PZT ceramics

One of the goals of this thesis is to understand the phenomena of softening in lead zirconate titanate (PZT). Specifically, it was important to understand how donor-doped materials differ from pure or acceptor-doped materials. Hence, it was decided to prepare high-quality PZT ceramics with a variety of donor-dopant concentrations. In parallel, we were looking at the defect-domain wall properties of $PbTiO_3$ using first-principles calculations. It order to compare experiments and theory, it was decided to prepare samples in the tetragonal regime of PZT. However, we observe greater domain wall contribution closer to the morphotropic phase boundary of the material. Hence, it was concluded that PZT 50/50 would be a reasonable composition to investigate. Besides undoped PZT, we investigated 0.1,0.2,0.5,1.0 and 2.0 at% Nb doped samples. We feel that the presence of grain boundaries do not significantly affect the electromechanical properties these ceramics. For example, aging has also been observed in single crystals of $BaTiO_3$ [63] and we also observed that the hysteretic properties of ceramics do not possess strong correlations with grain size.

4.1   Bulk ceramic processing

The mixed-oxide route is the most common route to synthesize ferroelectric ceramics. Shirane *et al.* [5, 125, 126] first adopted this technique to prepare solid-solution ceramics of PZT and this method was also utilized to determine the first full phase diagram of PZT [127]. The discovery of very high electro-mechanical properties at the morphotropic phase boundary by Jaffe *et al.* [128] also utilized samples prepared using the mixed-oxide route. Oxide powders

Materials	Grade	Manufacturer
Lead Oxide Litharge (PbO)	99.9+%	Sigma-Aldrich GmbH
Zirconium (ZrO_2)	99.96%	Tosoh Corporation
Titanium Oxide Anatase (TiO_2)	99.8%	Alfa Aesar GmbH
Niobium Pentoxide (Nb_2O_5)	99.9%	Alfa Aesar GmbH

Table 4.1: Oxide powders used in the synthesis of PZT ceramics.

were used as raw materials to synthesize the PZT ceramics. The purity and manufacturers of the oxide powders are shown in Table 4.1

The following steps were used to prepare the high-quality (low lead loss) samples of doped PZT:

1. The powders were mixed according to the stoichiometry $Pb(Zr_xTi_{1-x})_{1-y}Nb_yO_3$, where x is the at% of zirconium and y is the at% of niobium.

2. 80 gms of the mixture and 75 ml of isopropanol were ball-milled with 250 grams of zirconia balls for 8 hours. The mixture were dried on glass beakers at a slightly elevated temperature to increase the evaporation rate of the solvent.

3. The ball-milled mixture was calcined at 800^oC for 2 hours in a covered alumina crucible.

4. The ball-milling procedure was repeated to the calcined powder.

5. 5% binder solution of poly-vinyl alchohol (PVA) was added to the calcined powder and mixed thoroughly in a mortar.

6. The powder was uniaxially pressed into cylindrical pellets with a force of 4-5 kN, The diameter of the pellets were 7 mm and the thickness varied from 3-5 mm.

7. The pellets were placed into small covered alumina crucibles. The inner space of the crucibles were filled up with powders of the same composition as the pressed pellets to prevent evaporation of lead oxide during sintering.

8. The pellet was heated to 600^oC for 2 hours to release the binder and it was weighed before sintering.

9. The pellet was sintered at 1200^oC for 2 hours and cooled slowly (3^oC/min) till room temperature

A similar process was used to process lanthanum-doped samples.

4.2   Characterization

The samples were high quality and did not show the presence of black dots or cracks. Most of the samples showed a density between 96% and 98% (compared to theoretical density) as depicted in Fig. 4.1 and Fig. 4.2. A drop in density is observed at low concentrations of donor dopants. Room temperature $\theta - 2\theta$ coupling scannings were conducted on a Bruker D8 X-ray diffractometer from 20° to 60°. Fig. 4.3 shows the XRD spectra of sintered PZT powders with varying concentrations of Nb dopant. The powders were obtained by crushing the sintered pellets in a mortar. The XRD patterns were indexed using the appropriate powder diffraction files. No spurious peaks associated with the pyrochlore or PbO phase were detected.
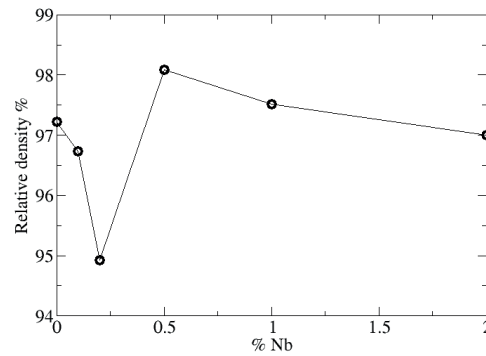
Figure 4.1: Density of PZT 50/50 with different concentrations of niobium
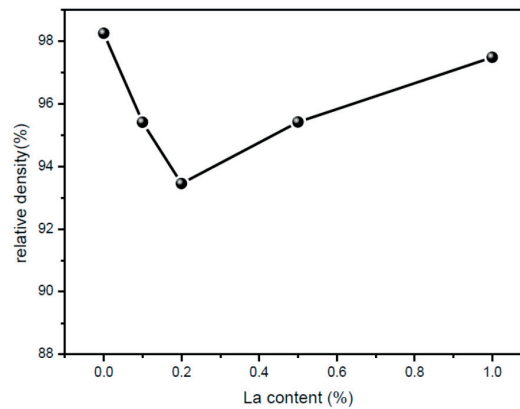
Figure 4.2: Density of PZT 50/50 with different concentrations of lanthanum

A few PZT samples were cracked and then thermally etched at 1050°C for 30 minutes in air. The SEM micrographs for the surfaces for 0.1,0.2,0.5 and 1%Nb are shown in Fig. 4.4(a), Fig. 4.4(b), Fig. 4.4(c) and Fig. 4.4(d). The 0.1 and 0.2% Nb showed clear signs of porosity as was indicated by the drop in density. The 0.5 and 1% Nb on the other hand did not show any signs of porosity. The grain size did not change significantly at low concentrations of donor dopants but at higher concentrations a reduction in grain size was observed.

4.3 Hysteresis loops

The characteristics of the hysteresis loops for the different PZT samples were carefully analyzed. Fig. 4.5 compares the different PZT 50/50 samples measured at different field strengths. It is evident that the loop becomes more open as we increase the donor-dopant concentration. Fig. 4.6 demonstrates the opening of the hysteresis loop for each of the samples while increasing the field strength. The effect of quenching and furnace cooling on the hysteretic behavior
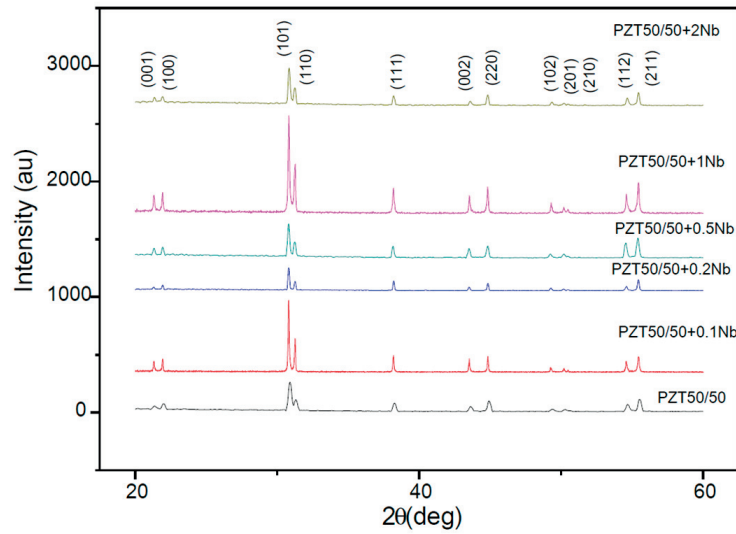
Figure 4.3: X-ray diffraction of PZT 50/50 peaks with different concentrations of Nb

of materials with different concentrations of donor dopants is analyzed. Since quenching in water results in a much faster cooling rate compared to furnace cooling, samples are likely to exhibit different domain configurations in either case. For pure PZT 50/50 quench cooling resulted in the opening of the hysteresis loop as depicted in Fig. 4.7. On the other hand, samples with 1%Nb showed near identical hysteresis loops for quench cooling and furnace cooling.

4.4 Summary

High-quality samples of pure and donor-doped PZT were prepared and characterized. At low concentrations of donor dopants we observe the presence of porosity and lack of densification. Very similar results have also been observed by Hammer and Hoffmann [129, 130]. The densification during sintering depends on volume diffusion which in turn is affected by the vacancy concentration. In undoped pure PZT, it is highly likely there exists an intrinsic concentration of lead and oxygen vacancies due to the evaporation of lead oxide. The presence of lead vacancies especially allows volume diffusion to occur and hence pure PZT has a density of more than 97%. The addition of small amounts of donor dopants likely reduces the concentrations of vacancies in two possible ways. As suggested by Hammer and Hoffmann, these donor additives may directly occupy lead vacancy sites at low concentrations. In Chap. 9 we also propose that donor dopants suppress the evaporation of lead oxide and therefore reduce the number of lead and oxygen vacancies created due to this evaporation process. Using either explanation, we feel that a reduction of vacancy concentration is the likely mechanism for the observed behavior at low donor dopant concentration.

As shown earlier, the hysteresis of pure undoped PZT shows a large dependence on whether
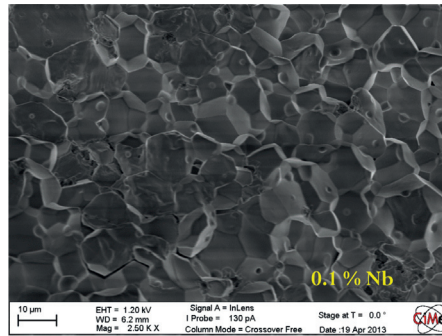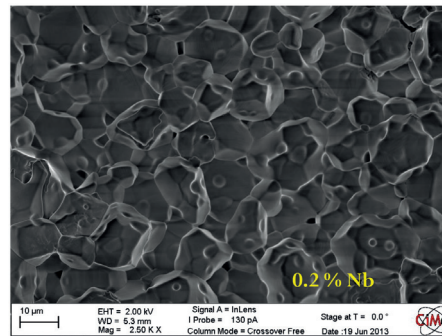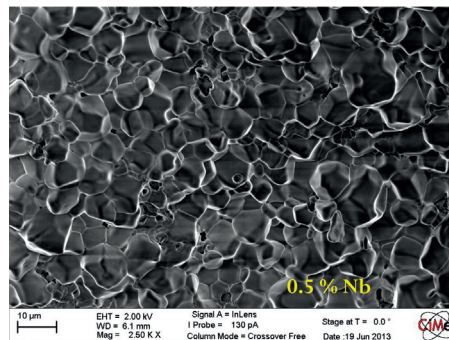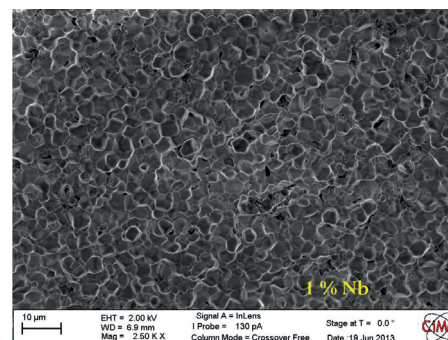
Figure 4.4: SEM micrographs for (a) 0.1 (b) 0.2 (c) 0.5 and (d) 1.0%Nb.

the sample is quenched or furnace cooled. At high temperatures in the cubic phase, vacancies and defect associates are randomly oriented homogeneously throughout the sample. When the sample is cooled slowly in the furnace two phenomena are likely to happen. First, polar defect associates align with the surrounding lattice polarization and stabilize certain domain orientations. Second, mobile defects such as oxygen vacancies may tend to migrate to domain walls. The pinning of domain walls results in inhibited domain wall movement characterized by a closed hysteresis loop as observed in furnace cooled pure PZT.

However, when the sample is quenched we observe an open hysteresis loop which is explained by increased domain wall mobility. This is because due to the fast cooling rate the defect

(a)

(b)

(c)
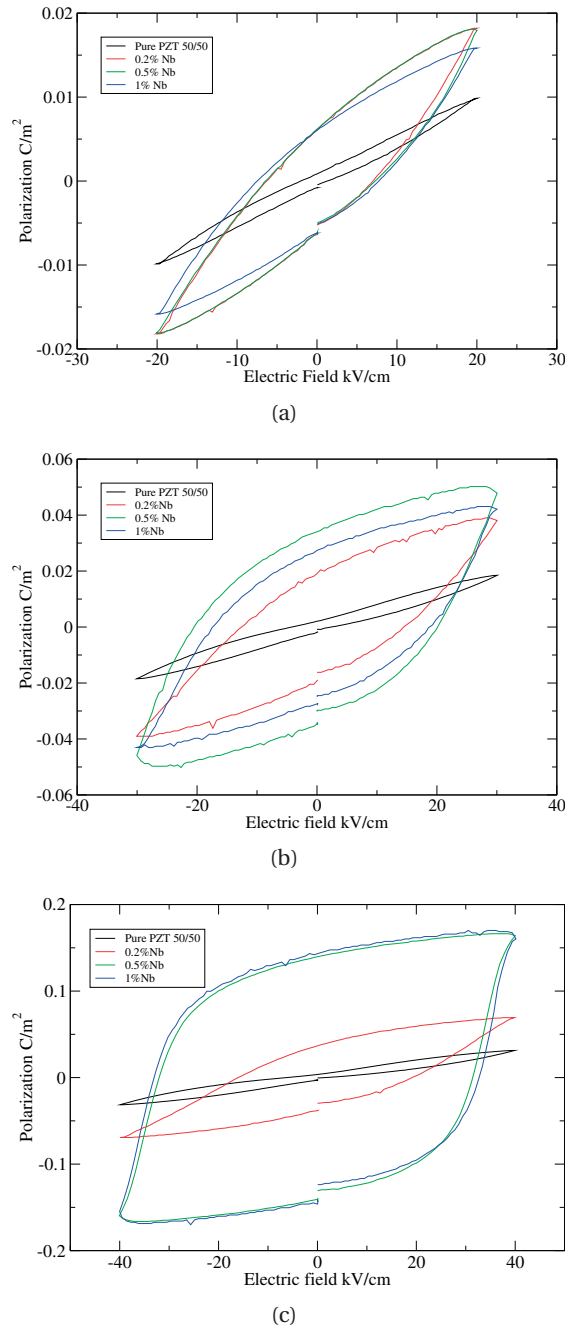
Figure 4.5: Hysteresis loops of PZT 50/50 as a function of dopant concentration at an electric field of (a) 20kV/cm (b) 30kV/cm (c) 40kV/cm.

associates do not have time to align with lattice polarization, and oxygen vacancies also do not have sufficient mobility to migrate to domain walls at lower temperatures. The fact that the hysteresis of 1%-donor doped samples does not show any dependence on cooling points to the fact that donor doped samples do not possess mobile polar defects and they also have a reduced concentration of mobile oxygen vacancies. These issues are discussed further in

Chap. 9.
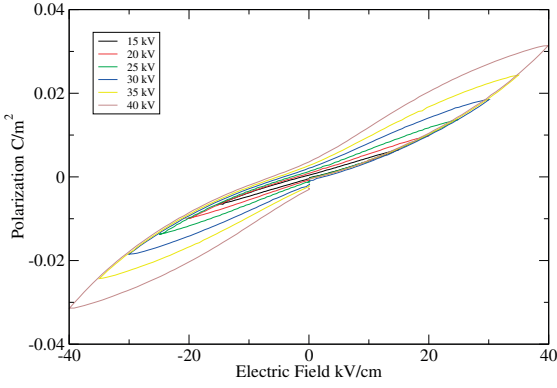
(a)
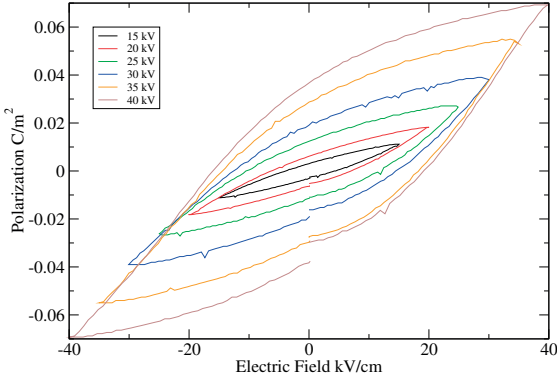
(b)
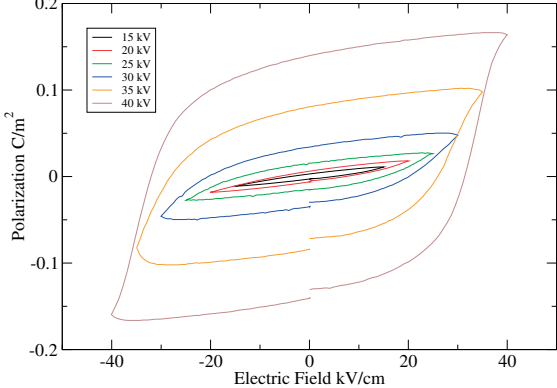
(c)
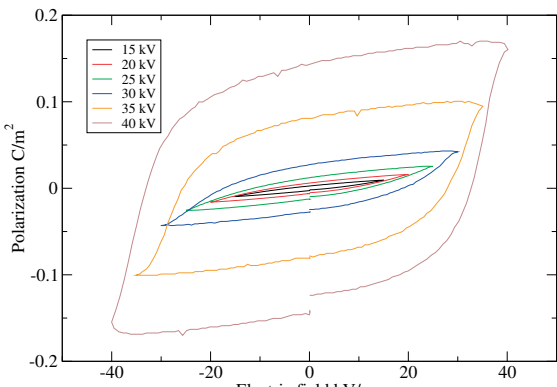
(d)

Figure 4.6: Opening of hysteresis loops for different dopant concentrations: (a) Pure PZT 50/50 (b) 0.2% Nb (c) 0.5%Nb (d) 1%Nb.
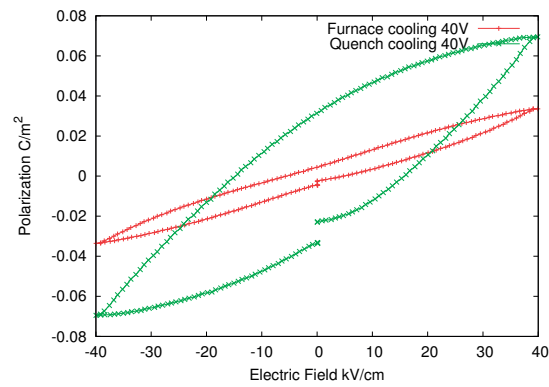
(a)
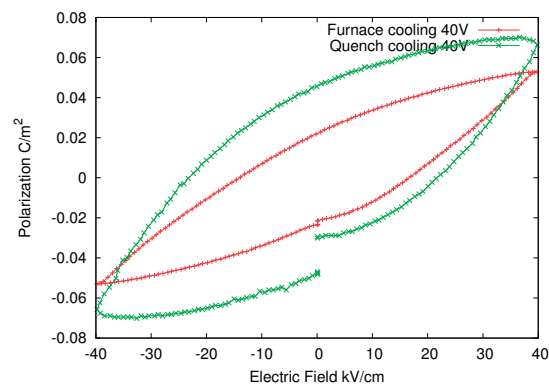
(b)
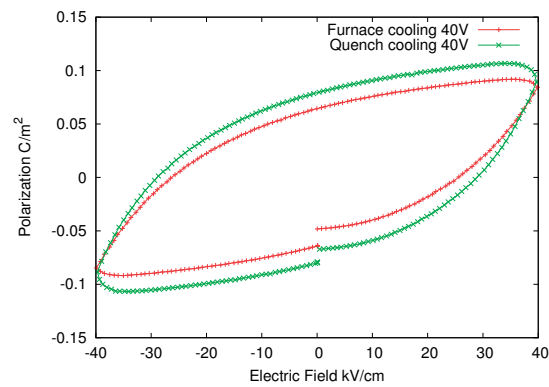
(c)

Figure 4.7: Hysteresis loops after quenching and furnace cooling for different dopant concentrations: (a) Pure PZT 50/50 (b) 0.2% Nb (c) 1.0%Nb .

5 Ordered defect complexes and interaction with 180° domain walls

This chapter investigates the nature of defects/defect associates in acceptor-doped, pure and donor-doped PbTiO$_3$ and also shows how these entities interact with 180° domain walls. Lead titanate is chosen because it is an end member of the most important family of piezoelectric and ferroelectric solid solutions (e.g., Pb(Zr,Ti)O$_3$ and Pb(Mg$_{1/3}$Nb$_{2/3}$O$_3$-PbTiO$_3$) [131] and doped PbTiO$_3$ itself is employed in some applications [132, 133] . While Pb(Zr,Ti)O$_3$ is structurally more complex near its morphotropic phase boundary, it is expected to behave as PbTiO$_3$ on the tetragonal side of the phase diagram. Although a lot of work has been done on the preferential alignment of metal-oxygen vacancy complexes [106, 112, 134], it is not yet clear whether lead-oxygen divacancies (presumed to be the most common defects in pure lead titanate and in PZT) display similar behavior. We also look at defect associates involving donor substitutional so as to compare how they differ in comparison to defects in pure and acceptor doped PbTiO$_3$.

5.1 Iron-oxygen vacancy defect associate

For the calculation of the acceptor-oxygen vacancy defect associate, one Ti atom in the 3*3*3 supercell was replaced by a Fe atom and the stability of oxygen vacancies at different positions with respect to the Fe atom was investigated. EPR experiments have shown that iron is in the trivalent state [60] and hence the substitutional defect is negatively charged. Recently, first-principles calculations have also confirmed that oxygen vacancies are doubly (positively) charged [103]. Thus, calculations on supercells containing the Fe$'_{Ti}$-V$_O^{..}$ defect associate (Kröger-Vink notation, where prime symbol denotes -1 charge and dot +1 charge relative to the charge of the host ion) are performed with a net positive charge +1. Fig. 5.1(a) shows the apical configuration of the Fe$'_{Ti}$-V$_O^{..}$ defect associate along the direction of polarization, Fig. 5.1(b) shows the equatorial configuration and Fig. 5.1(c) anti-apical configuration The lowest energy configuration is the one in which the defect associate is oriented in the direction of polarization (i.e. the apical configuration). The equatorial configuration of the Fe$'_{Ti}$-V$_O^{..}$ defect associate has a higher energy than the anti-apical state, suggesting that elastic effects are also important and the highest energy configuration is the one in which the two defects are

separated from each other (not shown). These results shows that the two defects indeed are driven to form a defect associate rather than remaining separated. All these calculations are in agreement with those performed by Erhart *et al.* [106], and with both the bulk stabilization effect of defect associates and the symmetry conforming mechanisms [45, 135].

Aging is then related to the time it takes for oxygen vacancies to hop from randomly oriented configurations to the aligned configuration below the Curie temperature, and deaging is the electromechanical process required to reverse this alignment process. Morozov *et al.* [67] observed that the AC conductivity for iron-doped PZT is a temperature-dependent Arrhenius process. The activation energy for this process was experimentally determined to be between 0.6 and 0.8 eV, in agreement with what was observed in deaging.

In order to verify if the energetics for oxygen vacancy migration matches that of conductivity and ageing we calculated all relevant barriers using nudged elastic-band calculations [136], and a minimum energy pathway was identified for the diffusion of the oxygen vacancy from the aligned state (Fig. 5.1(a)) to the equatorial state (Fig. 5.1(b)). Fig. 5.2 shows the potential energy surface for this process, with an activation energy of 0.89 eV in good agreement with Morozov *et al.* [67]. This value is slightly higher than the the barrier energy calculated very recently by Erhart *et al.* [134] (0.84 eV); the small discrepancies likely due to differences in pseudopotentials utilized.

(a)   (b)   (c)
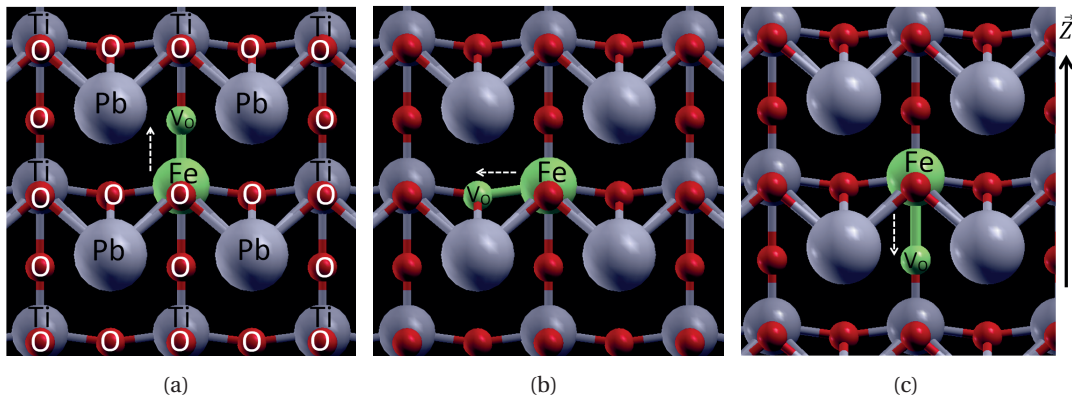
Figure 5.1: The different configurations for the Fe'_{Ti}-$V^{\cdot\cdot}_O$ defect associates in PbTiO$_3$. The lattice polarization is along the positive z direction, as shown by the black arrow, while the expected defect polarization in each configuration is indicated by the small dashed arrow. (a) The apical ground-state structure, with the Fe'_{Ti}-$V^{\cdot\cdot}_O$ defect associate oriented in the direction of lattice polarization. Magnetization is 3 Bohr mag/cell (b)In the equatorial state, the defect associate is oriented perpendicular to the lattice polarization. The energy of this configuration is 0.52 eV higher than the ground-state structure. Magnetization is 5 Bohr mag/cell (c) The anti-apical state with Fe'_{Ti}-$V^{\cdot\cdot}_O$ oriented in the opposite direction has an energy of 0.38 eV higher than the ground-state. Magnetization is 3 Bohr mag/cell
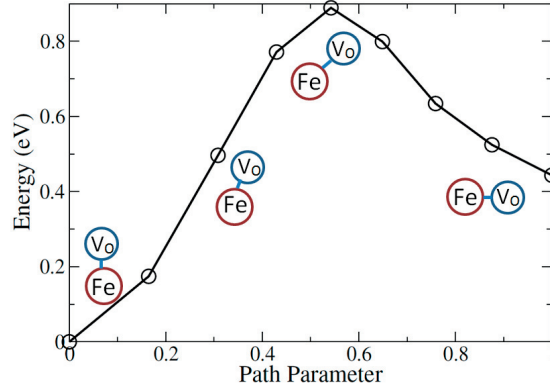
Figure 5.2: Energy barrier for the hopping of an oxygen vacancy from the apical to the equatorial configuration.

5.2 Lead-oxygen divacancy

Due to easy formation of lead and oxygen vacancies [103] in lead-based perovskites it is very likely that the V_{Pb}''-$V_O^{\cdot\cdot}$ divacancy could exist in an undoped material [137]. However, the structure of this divacancy is still controversial. Some authors claim the nearest-neighbor configuration to be the most stable [138], while others claim the two vacancies to be located further apart [139]. Cockayne *et al.* [138] calculated the polarization of the nearest-neighbor divacancy using the Berry-phase approach [96] and found it to be three times the bulk polarization. Here, we study the stability of different configurations of the lead-oxygen divacancy to understand its interactions with domain walls. The supercells were charge neutral since the lead vacancy is doubly (negatively) charged and the oxygen vacancy is doubly (positively) charged. Our calculations reveal that the next-nearest-neighbor apical configuration to be the ground-state, as shown in Fig. 5.3(a). The nearest neighbor apical configuration depicted in Fig. 5.3(b) is the next most stable. The equatorial configuration also shows a tendency to align along the polarization, as shown in Fig. 5.3(c), while the equatorial configuration opposing the polarization depicted in Fig. 5.3(d), is the least stable. Hence, we see a similarity between the behavior of the V_{Pb}''-$V_O^{\cdot\cdot}$ divancancy and the Fe_{Ti}'-$V_O^{\cdot\cdot}$ defect associate, where these defects are oriented preferably in the direction of polarization, explaining why nominally pure material containing lead and oxygen vacancies behave like hard, acceptor-doped materials.

5.3 Donor-lead vacancy defect associate

Donor-doped PZT is thought to be charge compensated by the formation of lead vacancies [40, 137, 140]. Currently, this defect complex has not been characterized although many conjectures on softening have been made, based on the formation of a $Nb_{Ti}^{\cdot}$-V_{Pb}'' associate. Here we investigate if this defect complex exhibits similar properties to the Fe_{Ti}'-$V_O^{\cdot\cdot}$ complex investigated earlier. For this system the supercell has a net negative charge, assuming the lead vacancy to be doubly negatively charged and the niobium substitutional defect to have a

(a)   (b)   (c)

(d)
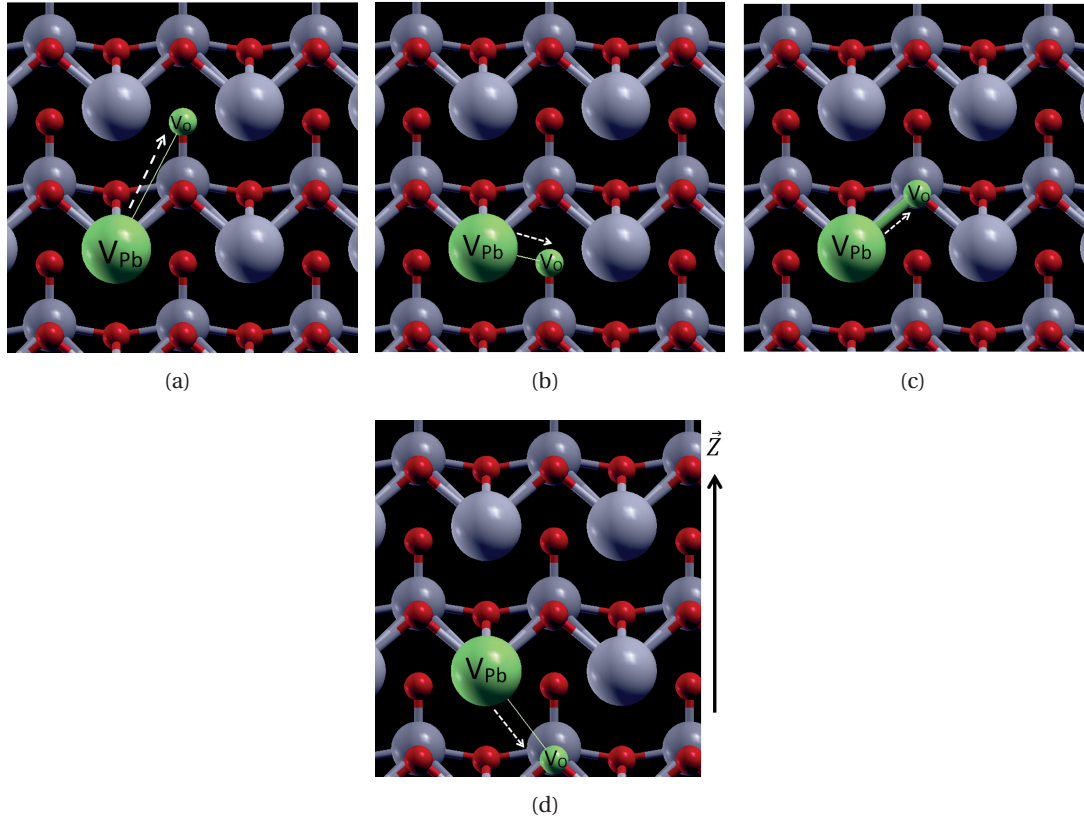
Figure 5.3: Different configurations of the V_{Pb}''-$V_O^{\cdot\cdot}$ defect associate relative to the lattice polarization shown with the black arrow. The expected defect polarization in each configuration is indicated by the small dashed arrow. (a) The next nearest-neighbor apical configuration of the V_{Pb}''-$V_O^{\cdot\cdot}$ divacancy is the ground-state structure. In this case there is a component of polarization pointing in the positive z direction which is the direction of the lattice polarization. (b) Nearest-neighbor apical configuration = 0.17 eV. In general it was observed that the oxygen vacancy prefers to be on an apical site. (c) Nearest-neighbor equatorial configuration = 0.30 eV. Even in this case, theres is a component of polarization pointing in the positive z direction. (d) Nearest-neighbor equatorial configuration with opposite polarization = 0.63 eV.

single positive charge. Fig. 5.4 shows the different configurations of the defect associate along with the relative differences in energy with respect to the ground-state. Fig. 5.4(a) depicts a schematic representation of the defect complex oriented along the direction of polarization, with the niobium substitutional defect at the center of the supercell. The configuration which is oriented away from the direction of polarization is shown in Fig. 5.4(b), and a configuration in which the two defects are located further away from each other is presented in Fig. 5.4(c). From these results we find that the selectivity for different configurations is much less than in acceptor-doped materials. Partial alignment for the defect associate in the direction of polarization is only 0.06 eV lower in energy than when oriented away from the bulk polarization. Even more interestingly, we find that that this defect complex is not tightly bound, unlike the acceptor defect associate, with a formation energy of just 0.04 eV

(Fig. 5.4(c)). EPR studies on Gd donor-doped soft PZT also seem to show no coupling with lead vacancies [141], and our results on PbTiO$_3$ agree well with this observation.
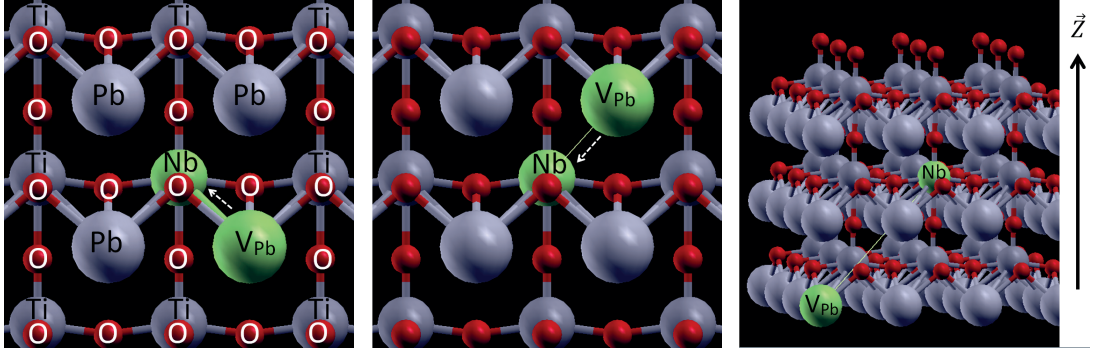
(a) The ground-state configuration of the Nb$^{\cdot}_{Ti}$-V$^{''}_{Pb}$ defect associate oriented in the direction of lattice polarization.

(b) Nb$^{\cdot}_{Ti}$-V$^{''}_{Pb}$ defect associate is oriented away from the direction of lattice polarization. It has an energy of just from polarization 0.06 eV higher than the ground-state.

(c) Dissociated defects = 0.04 eV higher than ground-state.

Figure 5.4: Different configurations of Nb$^{\cdot}_{Ti}$-V$^{''}_{Pb}$. There is almost no difference in the energy between the configuration oriented in the direction of lattice polarization (a), and the one oriented away from the polarization (b). Furthermore, this defect associate does not have significant binding energy as, shown in (c).

5.4 Defect interactions with 180° domain walls

In order to investigate the effect of dopants on domain walls, the structure and formation energy of a 180° domain wall in pure PbTiO$_3$ was calculated. Fig. 5.5 shows the schematics for this domain wall, centered on the (100) plane of lead and oxygen atoms. The formation energy is 116 mJ/m^2 and the barrier energy for the movement of the domain wall from one plane to the next is 28 mJ/m^2. The titanium centered configuration is the saddle point as shown in Fig. 5.6: The energies are plotted in eV and since we know the area of the domain wall in the supercell we report the barrier energy in mJ/m^2. The barrier energies reported here are slightly lower than those obtained by Meyer *et al.* [112], because in the present case the nudged elastic band is used to find the minimum energy pathway for domain wall movement, rather than using fixed atomic position calculations. This 180° domain wall is extremely sharp, extending only one unit cell in either direction of the interface before recovering bulk positions. We would like to highlight an interesting feature regarding the movement of a 180° domain wall. From Fig. 5.6, we see that the barrier energy for the movement of a domain wall is slightly asymmetric. The is because, due to periodic boundary conditions, the domain walls interact with each other. Specifically, during the movement of the domain wall it feels a slight repulsion from the adjacent domain wall. We observed that compressive strains decreased the repulsion of 180°domain walls with each other while tensile strains enhanced this repulsion.

To see how this barrier energy is affected by the presence of ordered defects, we repeated the nudged elastic band calculations with ordered defects at the domain wall. The supercell was similar to that shown in Fig. 5.5 but the dimensions in the y and z direction were doubled, with supercells made by 6*2*2 primitive cells.
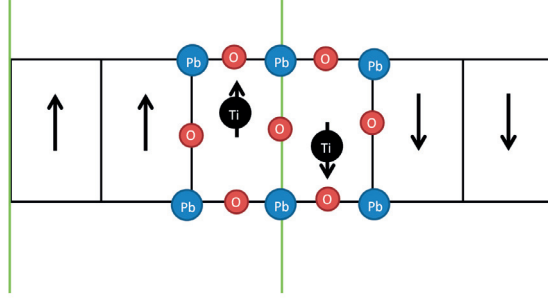
Figure 5.5: Schematics of a 180° domain wall supercell with arrows showing the direction of lattice polarization in each cell.
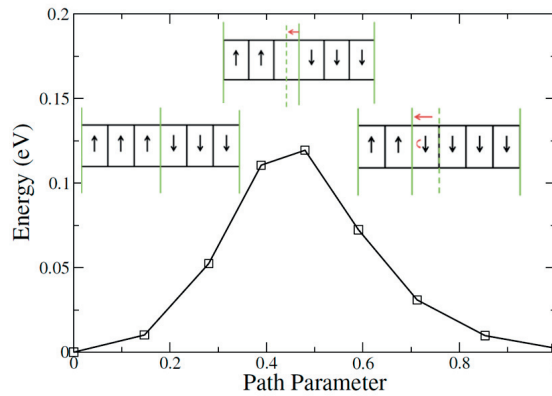
Figure 5.6: Energy barrier for the movement of the domain wall across one unit cell calculated using the nudged elastic band method. The three domain configurations (from left to right) correspond to starting,intermediate, and final positions respectively.

With this setup, we study the pinning effect of the Fe'_{Ti}-$V^{\cdot\cdot}_O$ defect complex and the V''_{Pb}-$V^{\cdot\cdot}_O$ divacancy. The Fe'_{Ti}-$V^{\cdot\cdot}_O$ defect associate is oriented in the +z direction (as depicted in Fig. 5.1(a)) and the V''_{Pb}-$V^{\cdot\cdot}_O$ defect associate also has a component in this direction (as shown in Fig. 5.3(c)).

Fig. 5.7 shows a schematic representation of the movement of the domain wall across the unit cell containing a defect associate. Once the domain wall moves, the defect polarization is oriented in the opposite direction of the lattice polarization. The nudged elastic band method is used to calculate the minimum energy pathway for this process. Fig. 5.8 depicts the energy barrier in the presence of defects, compared to the pure undoped case.

It is clear that there is an asymmetry in the barrier energy in both defect cases because of the

(a)   (b)
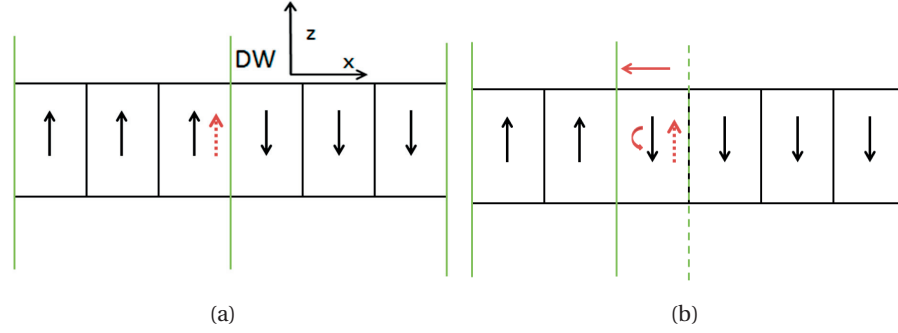
Figure 5.7: Schematics of the movement of the domain wall in the presence of a defect associate, whose position and polarization are represented by the small dashed arrow. (a)Initial state of supercell with the defect oriented in the direction of the cell polarization. (b)Final state after domain-wall motion where the defect is now oriented in the opposite direction to cell polarization.
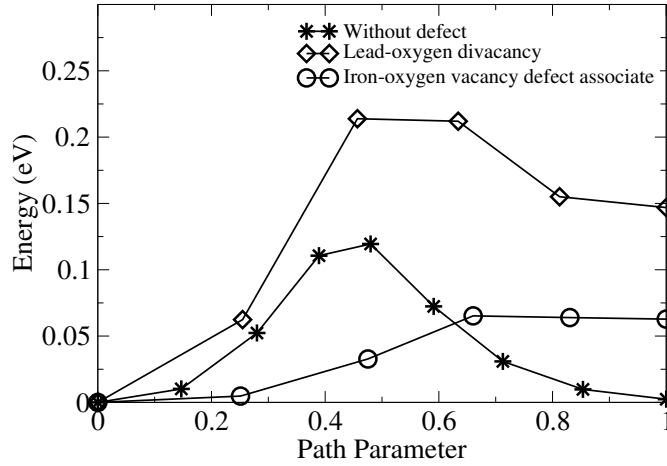
Figure 5.8: Energy barrier for the movement of a domain wall in the presence of different defects.

change in the relative polarization of the defect associates and the bulk. The V_{Pb}''-$V_O^{\cdot\cdot}$ divacancy also has a strong effect on the height of the barrier for the movement of the domain wall. To understand better the energy profile across the entire supercell, further calculations were performed to find out the position of these defects relative to the domain wall. Fig. 5.9 shows the energy of the supercell for four different positions of the Fe_{Ti}'-$V_O^{\cdot\cdot}$ defect associate with respect to the domain wall. The numbers on the x axis represent different configurations which vary in relative positions to this domain wall, as shown in Fig. 5.10. *Position -1* and *Position 0* represent configurations in which the defect polarization and lattice polarization are in the same direction, while *Position 1* and *Position 2* are configurations in which the two polarizations are in opposite directions; both *Position 0* and *Position 1* are at the interface of the domain wall. There are two main observations to be made from these calculations: First, a defect associate is least stable at the interior of the domain with opposing polarization. This

indeed points to the presence of a strong internal field effect which forces the domain wall to move. Second, the defect associate is more stable at the interface of the domain wall, rather than the interior of the domain with the same polarization direction. Hence it seems pinning is a combination of both bulk and domain wall effects.

The same calculations were repeated for the $V_{Pb}^{''}$-$V_O^{\cdot\cdot}$ defect associate and a similar profile was obtained (Fig. 5.11). The reduction in energy at *Position 2* arises from the fact that the pinning force is so high that the domain wall will shift its position relative to the defect. This result also agrees with strong domain-wall pinning observed in undoped PZT. To complete the study we also calculated the relative stability of isolated defects relative to the domain wall. In general, it was observed that all defects prefer to be at 180° domain walls. He and Vanderbilt [56] argued initially that neutral oxygen vacancies are more stable at such domain walls, but it has since been shown that oxygen vacancies with a double positive charge are the most stable moiety [103]. Neutral oxygen vacancies have a formation energy of around 10 eV [56] but doubly charged oxygen vacancies have been reported with a formation energy of just 0.28 eV [103] or even as low as -3.76 eV [104]. Hence, doubly positive-charged oxygen vacancies are investigated in this study. Fig. 5.12 shows the relative stability of the various oxygen vacancies (i.e x-V_O, y-V_O and z-V_O) at different positions from the domain wall. Energies are plotted with respect to the ground state of an oxygen vacancy in the z direction at the domain wall (z-V_O). From this potential energy surface we see that all types of oxygen vacancies have a lower energy at the domain wall. Fig. 5.13 shows a similar plot for a lead vacancy, a niobium defect on the titanium site, as well as a lanthanum defect on the lead site. All these isolated defects also have a lower energy at the domain wall. The energy difference between *Position 0* (Fig. 5.10(b)) and *Position 2* (Fig. 5.10(d)) is taken as a rough estimate of the pinning energy of a defect and Fig. 5.14 summarizes the pinning energies of defects and defect associates. Considering just the isolated defects, it can be seen that the oxygen vacancies (particularly z-V_O and x-V_O) have the greatest attraction to the domain wall and are hence the strongest pinning centers. However, the oxygen vacancy pinning is three times smaller than that of the $Fe_{Ti}^{'}$-$V_O^{\cdot\cdot}$ defect associate, as shown in Fig. 5.14. The calculations also indicate that the $V_{Pb}^{''}$-$V_O^{\cdot\cdot}$ divacancy could be an even stronger pinning center. As mentioned earlier, we could not calculate the pinning energy for this defect associate because of the movement of the domain wall to a new equilibrium position in the presence of the $V_{Pb}^{''}$-$V_O^{\cdot\cdot}$ defect associate.
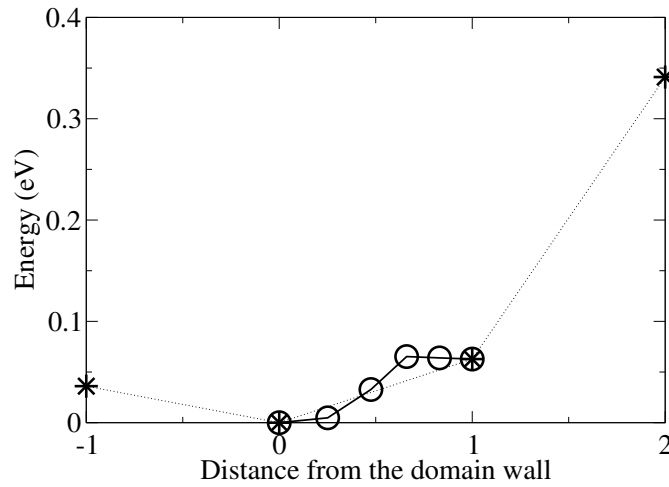
Figure 5.9: Energy profile of the supercell for different positions of Fe'_{Ti}-$V^{..}_O$ relative to the domain wall. The labels -1,0,1 and 2 are explained in Fig. 5.10. The solid curve shows the NEB calculation for the local movement between Positions 0 and 1. The dashed lines are only guidelines for the eyes.

(a) Position -1   (b) Position 0   (c) Position 1   (d) Position 2
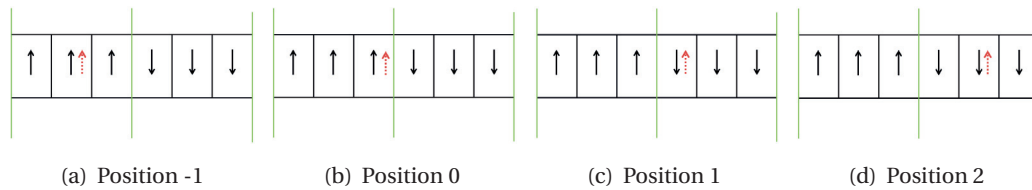
Figure 5.10: Configurations which differ in relative distance between defect and domain wall. The defect positions and polarizations are represented by the small dashed arrows.

5.5 Summary

In Fe acceptor-doped $PbTiO_3$, a defect associate is formed between the iron substitutional defect and a charged oxygen vacancy (Fe'_{Ti}-$V^{..}_O$). This defect associate aligns in the direction of the bulk polarization; this alignment is due to both electrostatic and elastic effects. The polarization direction of the defect associate can be changed by hopping of oxygen vacancies, and nudged elastic band calculations reveal that the activation energy for this process (0.8 eV) matches that of the experimentally determined AC conductivity and deaging process in hard PZT (0.89 eV). A similar ordering phenomena is also observed in the case of the lead-oxygen divacancy. However, in the case of Nb donor-doped $PbTiO_3$, the defect associate between the niobium substitutional defect and lead vacancy shows no binding energy and no preferential alignment with polarization. Hence, the $Nb^{.}_{Ti}$-V''_{Pb} defect associate is unlikely to exist and even if such defect complexes exist, it is clear that they do not interact strongly with the lattice polarization. It was also observed that ordered defect associates have a very strong effect on
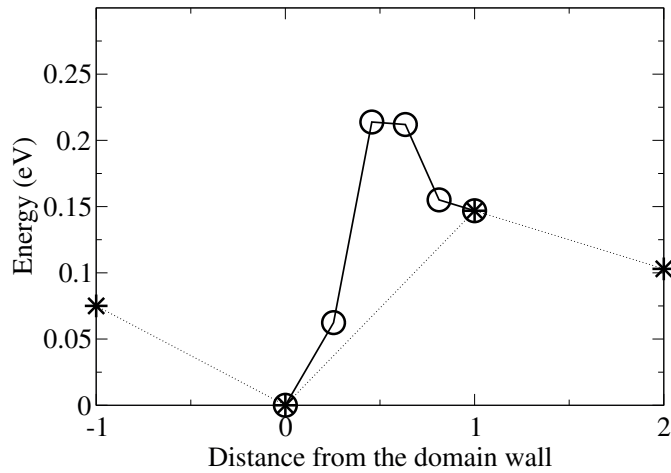
Figure 5.11: Energy profile of the supercell for different positions of V$''_{Pb}$-V$_O^{\cdot\cdot}$ relative to the domain wall. The solid curve shows the NEB calculation for the local movement of domain wall between Positions 0 and 1. The reduction in energy for *Position 2* is because the pinning strength is so high that it forces the domain wall to move towards the defect.
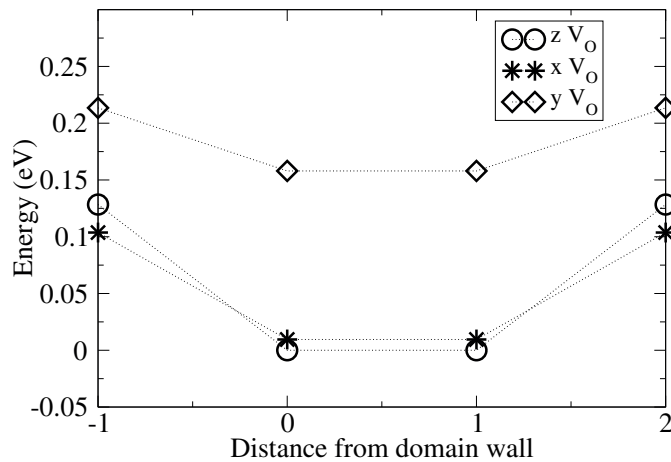
Figure 5.12: Stability of oxygen vacancies at different distances from the domain wall.

180° domain walls. They are not only more stable at domain walls but they also exhibit the characteristics of a random field defect, i.e. they break the degeneracy of polarization states to prefer a certain orientation. Oxygen vacancies, lead vacancies, niobium substitutional defects, and lanthanum substitutional defects are also more stable at domain walls. Amongst isolated defects, oxygen vacancies showed the greatest preference to be at domain walls. However, defect associates showed 3 times higher pinning strength compared to lone oxygen vacancies.

Finally, it is clear from this work that oxygen vacancies are key in forming polar defect complexes leading to pinched hysteresis loops and aging in both undoped and hard PZT. It is also shown that both the "bulk effect" and "domain-wall effect" are likely to contribute to the hardening phenomenon. The fact that polar defect associates are more stable at 180° domain
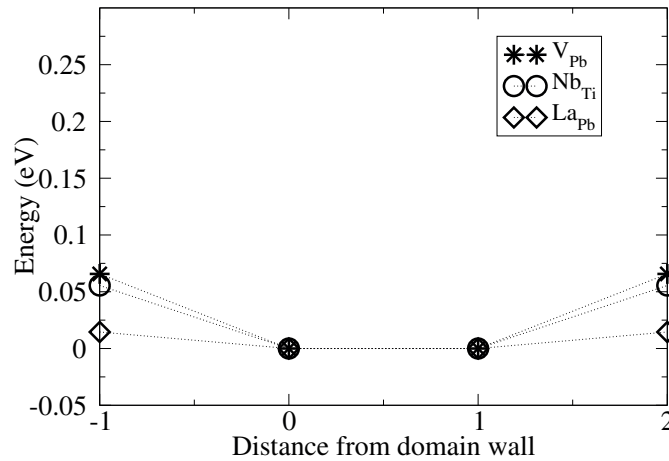
Figure 5.13: Stability of lead vacancy, substitutional niobium defect and substitutional lanthanum defect at different distances from the domain wall. The energies are plotted with respect to the ground-state structure in each case.
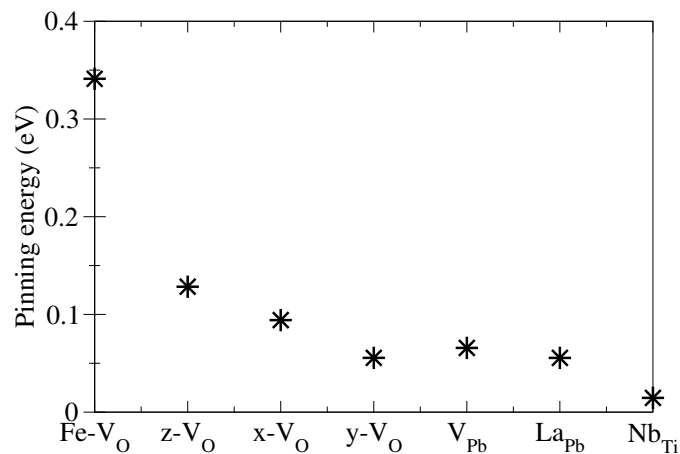
Figure 5.14: Pinning energies (see text for definition) of defects and defect associates.

walls has interesting consequences. It may explain why nano-domains are observed in Fe doped bulk ceramics [142]. The possibility of tuning domain size and domain orientation by the orientation of defect dipoles is technologically intriguing: Controlled nanodomains could produce higher density FeRAM storage devices. It may also give rise to the possibility of stabilizing charged domain walls which would otherwise be unstable.

6 Bloch walls in PbTiO$_3$

The change of an order parameter, like the polarization, over an interface can occur in a variety of ways. We can classify the resulting structures into 3 different types of interfaces/domain walls, as shown in Fig. 6.1. In an Ising wall, the polarization vector diminishes in magnitude close to the wall but does not rotate. In a Bloch wall, the polarization vector rotates along/within the plane of the domain wall. In a Néel wall, the polarization vector rotates perpendicular to the plane of the domain wall. Ferroelectric oxides were generally thought to possess domain walls of the Ising type [112]. Over the past few years, however, there have been a few theoretical predictions of the presence of Bloch and Néel components in some ferroelectric materials and heterostructures [143, 144]. Behera *et al.* [144] showed the presence of a vary small Néel component in the ferroelectric 180° domain walls of PbTiO$_3$ while Taherinejad *et al.* [145] showed the presence of Bloch components in 180° domain walls of rhombohedral BaTiO$_3$
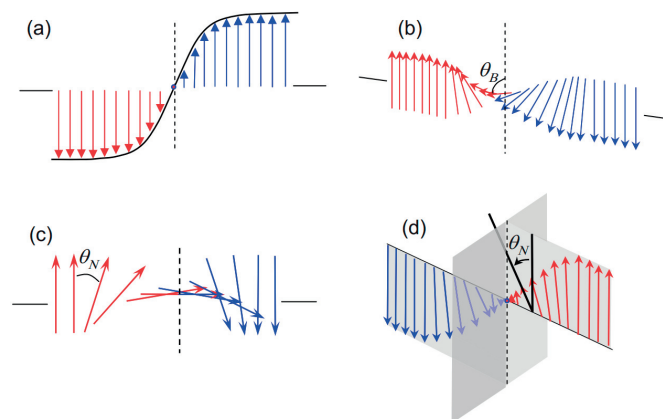
Figure 6.1: Different types of domain walls (a) Ising, (b) Bloch, (c) Néel, and (d) mixed Ising-Néel type [143].

In this chapter we will carefully examine the structure of 180° domain walls in PbTiO$_3$, finding a strong Bloch component of polarization, in contrast with earlier work [112, 144].

An 8*1*1 supercell was constructed with the ground state structure of lead titanate. We also performed a few calculations with a 24*1*1 supercell to verify convergence of our atomic positions. A schematic of the domain wall is shown in Fig. 6.2. The polarization vector is depicted by green arrows and a rotation of polarization at the domain wall is clearly visible. The effective polarization per unit cell is calculated using Born effective charges calculated for a single unit cell of PbTiO$_3$, as shown in Tab.6.1. These are in good agreement with literature [146]. We used a Ti-centered unit cell for the calculation of the local polarization. The spontaneous polarization of lead titanate is in the +P$_z$ and -P$_z$ in the two domains. The Bloch component of polarization is in the +y direction. Fig. 6.3 shows the variation of P$_z$ and P$_y$ components along the supercell.

From Fig. 6.3 we see that the Bloch component of polarization is confined to two unit cells, with the local displacement of individual atoms in the vicinity of the domain wall shown in Fig. 6.4. The Bloch domain wall is mostly localized on a plane of Pb and O atoms and the displacement of the lead atom and of the equatorial oxygen p_z Wannier function are the most prominent [147] features. The lead atom is displaced in y direction by 0.14 Å relative to its high symmetry position in the Ising wall. The Bloch wall is mainly localized to a single Pb-O plane separating the two domains and one may even label this as a two dimensional ferroelectric state. However, in order to classify as a ferroelectric state one should be able to switch polarization from the $+y$ direction to the $-y$ direction.

To verify this, we performed a nudged elastic band calculation to calculate the energy barrier needed to switch between the Ising state and the Bloch state of the domain wall. The energy landscape is extremely flat and the energy difference between the Bloch and Ising states is less than 1 meV per 8-atom cell as shown in Fig. 6.5. The polarization for all the images was calculated using the Berry-phase approach. The flatness of this potential energy well implies that at higher temperatures the Bloch polarization is likely to be on average zero due to thermal fluctuations.

We looked at development of the Bloch state w.r.t different strains for the lattice parameters a and c. This is done by looking at the displacement profile for the lead atoms at different strains, as depicted in Fig. 6.6 and Tab. 6.2. We see that tensile strains on the lattice parameter are very effective in increasing the Bloch component of polarization. Tensile strains on the c axis and compressive stresses on the a lattice parameter suppress the displacement of lead atoms. Fig. 6.7 illustrates the effect of strain on the energy barrier needed to switch between the Bloch and Ising states. We see that one may stabilize the interfacial ferroelectric state by increasing the c/a aspect ratio. Perhaps, by depositing on a suitable substrate, one may stabilize the Bloch domain wall in PbTiO$_3$ even at higher temperatures. Another interesting avenue to explore would be to observe the effects of solid solution alloying on the stability these types of Bloch domain walls.

Atom	Z_{xx} (Å)	Z_{yy}	Z_{zz}
Pb	3.75	3.75	3.43
Ti	6.19	6.19	5.2
O_{eq}	-2.63	-5.18	-2.07
O_{ax}	-2.14	-2.14	-4.48

Table 6.1: Born effective charges calculated on the ground state tetragonal unit cell of PbTiO$_3$.
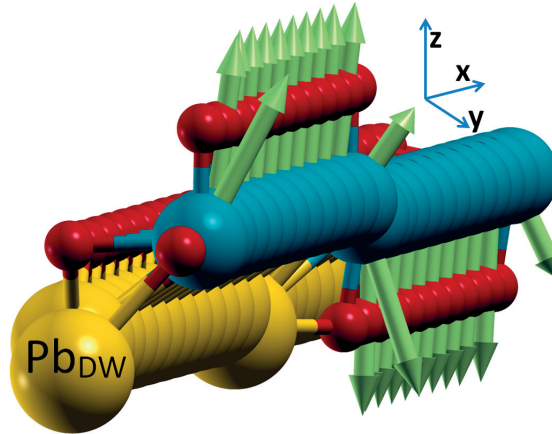
Figure 6.2: Relaxed structure of the domain wall supercell showing rotation of polarization at the domain wall. The displacement of the lead atom at the domain wall (Pb$_{DW}$) in the y direction is clearly visible.
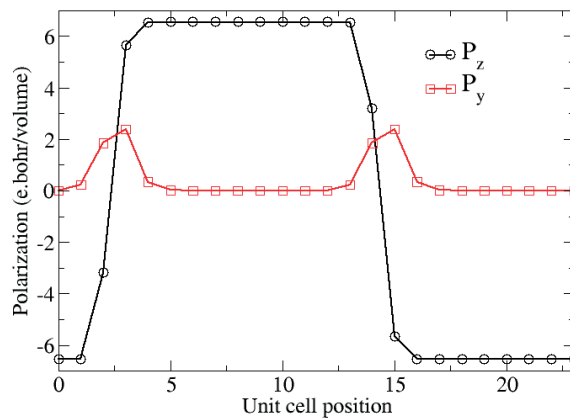
Figure 6.3: The variation of the P$_z$ and P$_y$ components of polarization along the supercell. The development of the P_y component of polarization at the domain wall is indicative of the Bloch type of wall.

6.1 Bloch walls in PZT

Recently, Yudin *et al.* [148] have explored the stability of Bloch walls in the vicinity of the morphotropic phase boundary using phenomenological methods. The addition of zirconium
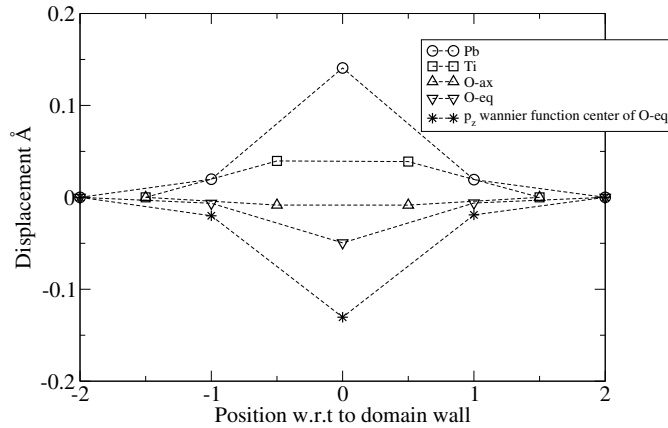
Figure 6.4: Displacements of different atoms across the domain wall. The anomalous strong displacement of the equatorial oxygen vacancy p-orbital Wannier function is also shown
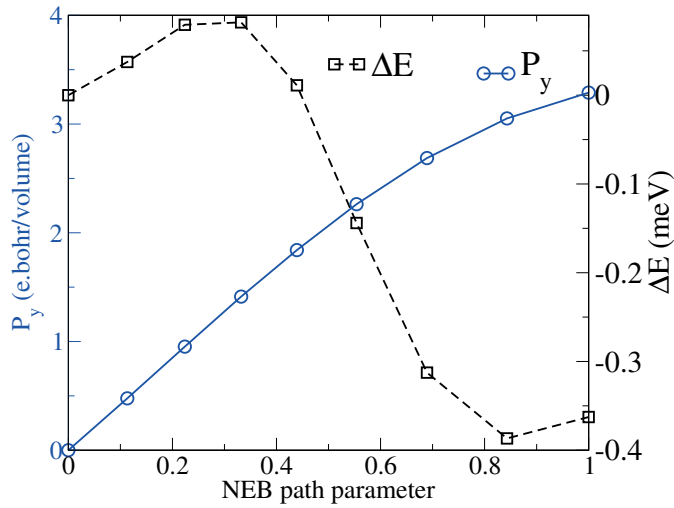
Figure 6.5: Change in polarization and energy when switching from an Ising state to a Bloch state.

to PbTiO$_3$ increases the *a* lattice parameter while more or less maintaining the same *c* lattice parameter. There is approximately a 4% increase in the *a* lattice parameter for tetragonal PZT 50/50 [149] compared to case of PbTiO$_3$. Based on this information and the results of the previous section, we would expect a strong Bloch polarization in PZT as well. We constructed an 8*2*2 supercell with an ordered checkerboard structure of zirconium and titanium atoms. The lattice parameter *a* and *c/a* ratio was kept at the ambient temperature experimental value [149]. Once the forces were minimized, we observed a strong displacement of the lead atom in the *y*-direction of 0.26Å which indicates the presence of Bloch polarization in PZT 50/50 as well.
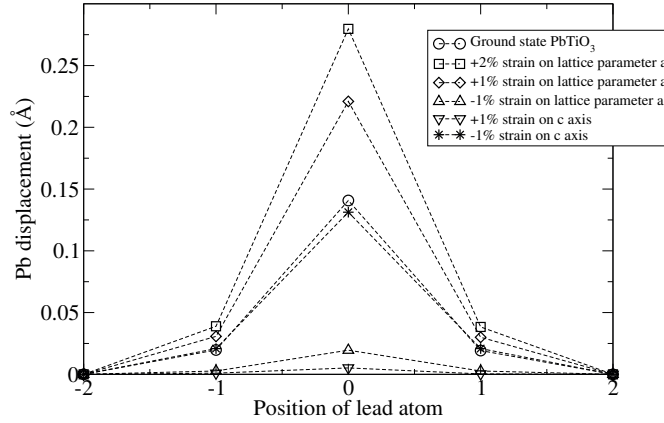
Figure 6.6: Displacement of the lead atom with respect to different strains on the *a* and *c* lattice parameters.
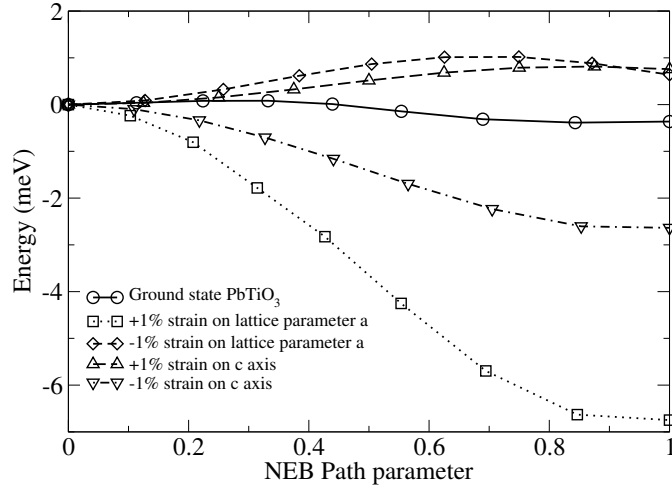
Figure 6.7: Energy barrier to switch between Ising and Bloch walls at different strains.

6.2 Piezoelectric properties

Polarization rotation has long been shown to increase piezoelectric properties [150]. For example, the presence of a flat energy landscape at the morphotropic phase boundary of PZT is known to be responsible for enhanced properties [151]. Since the energy landscape for the rotation of polarization at the $PbTiO_3$ domain wall is extremely flat, it was of interest to calculate the piezoelectric properties of Bloch domain walls. The spontaneous polarization, P_y, of the Bloch wall is in the y direction and we calculated the polarization response in the y direction due to a strain applied in the same direction, i.e. the longitudinal piezoelectric constant. We calculate first e_{33} for the 5 atom unit cell of $PbTiO_3$ that is 4.5 C/m^2 in good agreement with experimental values of e_{33} which range from 3.35 C/m^2 [152] to 5.0 C/m^2 [153]. The piezoelectric coefficients are calculated by performing Berry-phase calculations as a function of small tensile strains from the initial equilibrium configuration.

Strain	Lead atom displacement (Å)	Polarization (e.bohr/Vol)
0 strain state	0.14	3.27
+1% strain on lattice parameter a	0.22	5.39
+2% strain on lattice parameter a	0.35	7.29
-1% strain on lattice parameter a	0.02	0.5
+1% strain on c axis	0.005	0.168
-1% strain on c axis	0.13	3.47

Table 6.2: Lead displacements for different strains on the *a* and *c* lattice parameters of lead titanate

For the domain wall calculations we used 8*1*1 and 24*1*1 supercells. The respective e$_{22}$ values were 6.3 C/m^2 and 1.72 C/m^2. It is important to note that the main contribution to the piezoelectric constant arises mainly from the domain wall, hence the total piezoelectric constants go down as we reduce the density of domain walls. However, it is interesting to note that an 8*1*1 domain wall supercell is sufficient to produce an effective longitudinal piezoelectric constant higher than that of bulk lead titanate. Hence a dense array of patterned domain walls can producer a higher piezoelectric response than mono-oriented films of lead titanate PbTiO$_3$.

7 90° "neutral" walls in PbTiO$_3$ and interactions with defects

The interaction of oxygen vacancies with domain walls has long been thought to be responsible for influencing the properties of ferroelectric materials. For example, the orientation of metal-oxygen vacancy defect associates causes the phenomena of "aging" in doped ferroelectric ceramics [43, 49, 154]. The ordering of oxygen vacancies is believed to be one of the causes behind the phenomenon of ferroelectric fatigue [102, 155]. More recently, Sluka *et al.* [29] suggested that oxygen vacancies accumulate at tail-to-tail charged domain walls in BaTiO$_3$. Becher *et al.* [123] showed how coupling of oxygen vacancies with domain walls in SrMnO$_3$ altered the conductive properties of the wall with respect to the bulk. Surprisingly, no first-principles calculations have yet been reported on the interaction of 90° domain walls with oxygen vacancies in PbTiO$_3$ or PZT (lead zirconate titanate), despite the latter being the technologically most relevant ferroelectric material.

In this chapter we first report observations on the structure of the 90° domain wall in PbTiO$_3$. A structural asymmetry in lattice parameter variation across the domain wall is shown. We then investigate the interaction of such walls with different types of oxygen vacancies. The possible pinning mechanisms involving oxygen vacancies are studied.

7.1   Structure of 90° domain wall

We performed calculation on a 60-atom supercell containing two 90° domain walls. The construction of the cell is similar to that reported by Meyer and Vanderbilt [112]. In our simulation, the dimensions of the supercell were approximately $8.8a$*a*$1.45a$ (where a is the lattice parameter of 3.87 Å). We then looked at the lattice parameter variation across the supercell by measuring the Pb-to-Pb distance along a particular direction. Hence, as we move across the domain wall, one would expect a smooth inversion of the $a - c$ lattice parameters [113] (due to the 90° rotation at the wall). However, from Fig. 7.1(a) it is seen that this variation is not smooth at all and it is not symmetric with respect to the plane of the domain wall. We define the "tail" part as the side of the domain wall in which the polarization vector is pointing away from the wall. The "head" refers to the part in which the polarization

is pointing into the domain wall. We observe a large discontinuity of the lattice parameter variation at the domain walls; specifically at the "tail" part of the domain wall there is a sharp dip in the $a-c$ transition and a small peak in the $c-a$ transition. This leads to an unit cell with large c/a ratio of 1.11 close to the domain wall. In comparison, the right side of the domain wall (i.e. the head part) shows a very smooth variation of the lattice parameter. Calculations were also performed for longer supercells (upto 240 atoms) to verify that this discontinuity is independent of cell size. Earlier calculations by Meyer and Vanderbilt [112] showed the presence of a step in the electrostatic potential across the 90° domain wall leading to a band offset of 0.15-0.2 eV. The structural asymmetry reported in this work is likely a manifestation of the presence of bound charges at the 90° domain wall.

Probe-corrected scanning transmission electron microscope (STEM) was used to identify this asymmetry experimentally. PZT 10/90 (10% zirconium and 90% titanium) thin films were prepared for this purpose; the details of the sample preparation are mentioned in a recent work by Feigl *et al.* [35]. The films are 160 nm thick, likely sufficient to minimize substrate effects. The cross-sectional PZT 10/90 specimens used for electron microscopy were prepared by conventional methods including grinding, dimpling, polishing and milling by argon ions. The atom-resolved high-angle annular-dark-field (HAADF) experiments were performed on a probe-corrected FEI Titan 80-200 microscope, operated at 200 kV. Two-dimensional Gaussian profile fitting to each individual Pb column was used to determine the lattice parameters from the HAADF-STEM image.

Fig. 7.1(b) shows the lattice parameter variation across the domain wall measured in the PZT 10/90 thin film. This material is also tetragonal and has lattice parameters very close to those of PbTiO$_3$ as evident by the y-axis on both Fig. 7.1(b) and Fig. 7.1(a). Comparing with first-principles results we see the same dip in the $a-c$ transition (red circles) and we see a sharper peak than that predicted theoretically in the $c-a$ transition (blue squares). The c/a ratio of the unit cell (both experimental and first-principles) is presented in Fig. 7.2. We see quantitative agreement between the experimental and computational results.

These highly accurate measurements verify the presence of this asymmetry in the 90° domain wall structure. Stemmer at al. [113] were the first to observe the structure of the 90° domain wall in PbTiO$_3$ using conventional high-resolution transmission electron microscopy. However, the accuracy of such measurements was much lower and they predicted a continuous symmetric lattice parameter variation. On closer inspection of their data points we see hints of this discontinuity, which were verified by our more accurate STEM measurements.

Although this observation might seem surprising at first, reasons for it become clearer when considering the inherent asymmetric nature of most ferroelectric interfaces and surfaces. Let's consider a ferroelectric thin film with polarization pointing out of the plane of the film. This positively charged surface will show the presence of ionic reconstructions to minimize the bound polarization charge on the surface. Once the polarization is reversed, the surface will restructure in a completely different way. This was best illustrated in the recent work by Saidi
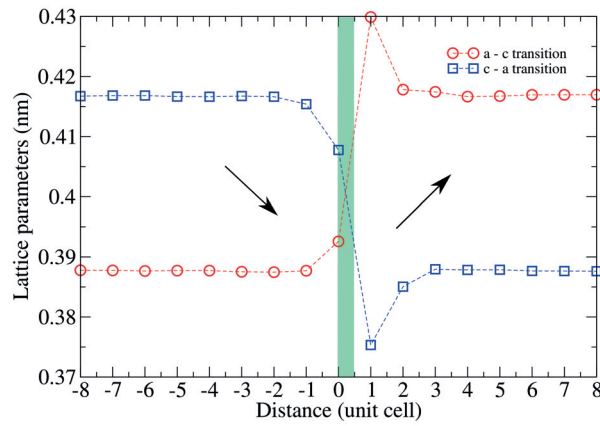
(a)
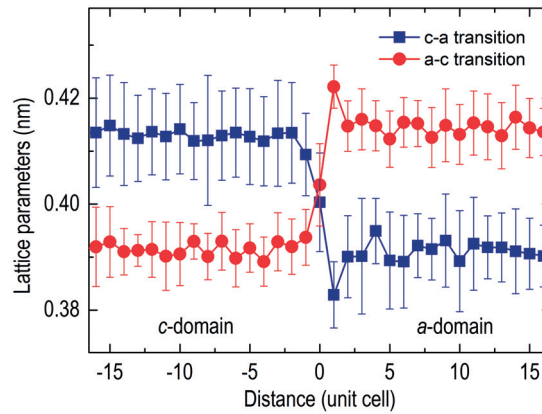
(b)
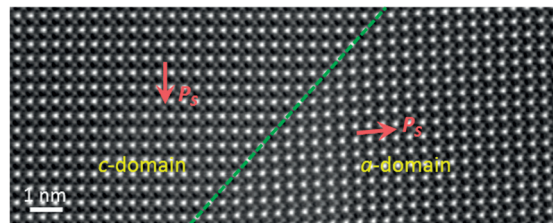
(c)

Figure 7.1: (a) Variation of the lattice parameter across the domain wall as found in first-principles calculation on PbTiO$_3$. The shaded green region represents the approximate region of the domain wall and the black arrows show the general direction of polarization in each domain. (b) Experimental measurements on PZT 10/90 thin film. (c) Atom-resolved HAADF-STEM image of a, c domain and domain wall viewed along [010] direction in 160 nm thick PZT 10/90 thin film. The red arrows indicate the direction of spontaneous polarization.

(a)

(b)
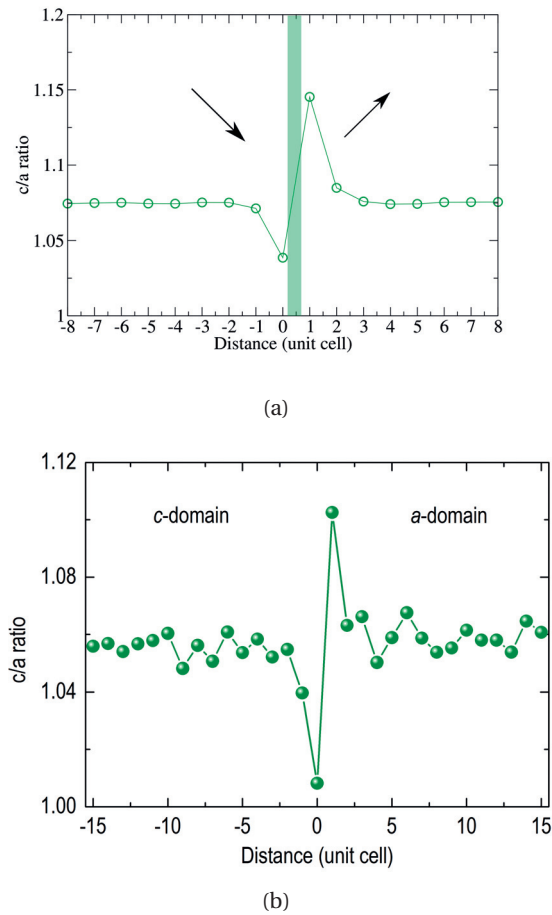
Figure 7.2: Variation of the c/a ratio across the domain wall as found in (a) first-principles calculation on PbTiO$_3$ and (b) experimental measurements on PZT 10/90 thin film.

et al. [156] on the interaction of the polarization with surface stoichiometries in PbTiO$_3$ and BaTiO$_3$.

Last, we would like mention that a measurement on another region of the sample revealed a domain wall in which a large tetragonality existed on the head side rather than the tail side of the domain. As yet we have no clear explanation for such types of domain walls. A detailed experimental investigation of the domain wall structure dependence on film thickness, domain wall bending angle and presence of defects will be addressed in a future work.

7.2 Interaction with oxygen vacancies

Next, it is of interest to understand the interaction of these domain walls with oxygen vacancies. Recent hybrid density-functional theory calculations on PbTiO$_3$ have established the oxygen vacancy as being doubly positively charged [104] in such ferroelectric oxides. In this work we

look at the interaction of charged oxygen vacancies with the 90° domain walls studied above. Due to the tetragonal symmetry of PbTiO$_3$ there are two types of oxygen vacancies: apical (V$_{ap}$) and equatorial (V$_{eq}$). The apical vacancies, located on the apex of the oxygen octahedra, are known to be energetically more favorable compared to the equatorial vacancies [103, 104, 157] located in the equatorial plane of the octahedra. First, we looked at the stability of apical oxygen vacancies at different positions with respect to the domain wall. The supercell studied in the previous section is doubled in the y and z directions to avoid strong interaction of vacancies with their periodic images and to reduce the effective planar concentration of vacancies in the y-z plane. The energy landscape is plotted in Fig. 7.3(a) and the most stable position of the apical oxygen vacancy (V$_{ap}$) is depicted in Fig. 7.4. Surprisingly, the ground state oxygen vacancy position is not located exactly on the plane of the domain wall but is in fact located on the adjacent plane (on the "tail" side of the domain wall). This result further supports the notion that the domain wall is asymmetric and behaves more like a capacitor with uncompensated polarization charges on either side of the wall [158]. It has also been postulated that oxygen vacancies can stabilize strongly charged tail-to-tail domain walls [30]. Indeed, from our calculations we observe that apical oxygen vacancies are more stable on the "tail" side of the domain rather than the "head" side. The relative stability of equatorial oxygen vacancies is shown in Fig. 7.3(b). These are also preferably positioned on the tail side but do not show as strong a specificity as the apical oxygens. This is mainly due to the fact that equatorial vacancies do not interact with the polarization as strongly as apical oxygen vacancies. Apical vacancies are even thought to invert the polarization locally [102, 155] due to these strong interactions.

Note that the ground state equatorial oxygen vacancy would prefer to migrate to an apical oxygen vacancy position since the energy difference between these two position is 0.44 eV (calculated but not shown here). As mentioned before, this energy difference is due to non-degenerate nature of apical and equatorial oxygen vacancies in tetragonal oxides. The movement of the 90° domain wall requires short-range displacement of atoms, while the movement of oxygen vacancies requires the migration of oxygen atoms. The two processes have vastly different energy scales. The barrier energy for the movement of 90° domain wall is less than 1 mJ/m^2 [56] (of the order of few meV per unit cell) while oxygen vacancies have migration activation energies of up to 0.9 eV [159]. Hence, at low temperatures, the defects are unlikely to move (or they move slowly) with respect to the domain walls. Consider a situation in which an apical oxygen vacancy exists in one domain a few nanometers from a 90° domain wall. The movement of a domain wall across the defect will cause it to transform into an energetically unfavorable equatorial vacancy. Hence it will oppose the motion of the domain wall towards its direction. We can capture this situation using first-principles calculations as depicted in Fig. 7.5. On the right side of the figure the oxygen vacancy is in the low-energy apical state. Close to the domain wall it is in its ground state position. If the domain wall continues to move, the vacancy transforms to the high energy equatorial state depicted on the left side of the figure. In other terms, the oxygen vacancy behaves both as a "random-bond" [56, 160] defect and "random-field" [49, 53] defect; It prefers to exist in
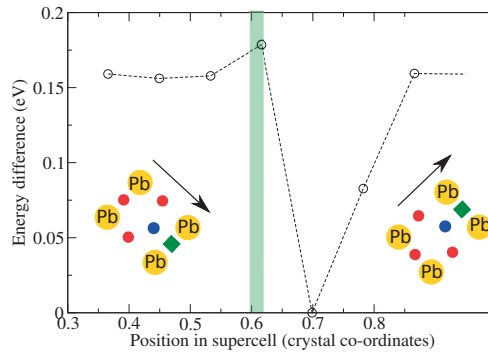
(a) Stability of the apical oxygen vacancy at different positions along the supercell.
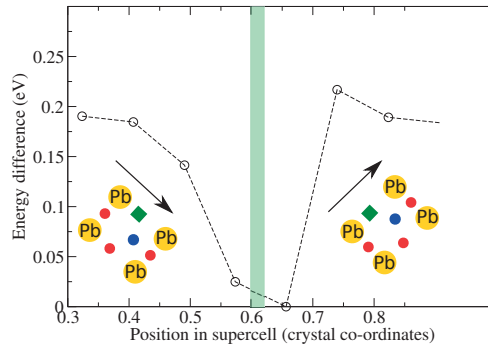
(b) Stability of an equatorial oxygen vacancy at different positions along the supercell.

Figure 7.3: Stability of two types of oxygen vacancies (V$_{ap}$ and V$_{eq}$) at different positions with respect to domain wall. The domain wall is represented by the shaded green region.

certain domain orientations compared to others (random-field) but it also prefers to exist close to the domain wall. Based on Fig. 7.5, we may say there are two pinning regimes. Starting from a low-temperature disordered state, there would be a spatially random distribution of vacancies acting as random-field defects. At higher temperatures and longer time scales, oxygen vacancies would aggregate close to the domain wall (the global minimum) and act as random-bond defects.

Finally, we sought to understand the effect of the ground state apical oxygen vacancy on the local structure of the domain wall. When vacancies accumulate at the domain wall, do they enhance/reduce the lattice parameter discontinuity at the domain wall? Fig. 7.6(a) shows the theoretical prediction for the variation of the lattice parameter across the domain wall in the presence of the apical oxygen vacancy on the tail side of the domain wall. The lead-to-lead
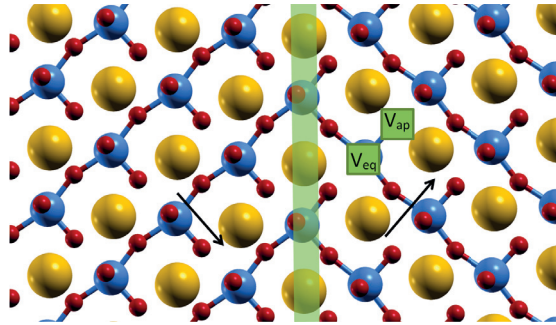
Figure 7.4: Schematics showing the ground state positions of the apical oxygen vacancy (V_{ap}) and equatorial oxygen vacancy (V_{eq}). The large yellow spheres are lead atoms, small blue spheres are titanium atoms, small red spheres are oxygen atoms. The plane of the domain wall is represented by the vertical green region across the middle of the figure. Black arrows in the figure shows the direction of polarization in each domain.
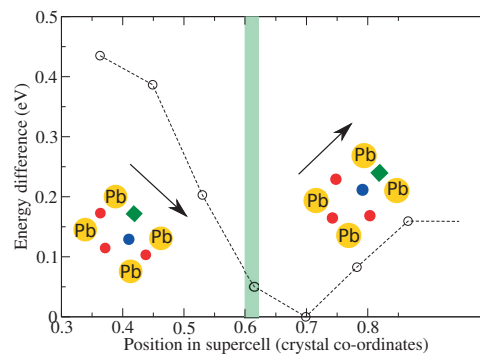
Figure 7.5: Graph illustrating the pinning of 90° domain walls by oxygen vacancies. On the right side of the figure the oxygen vacancy is in the low energy apical state. Close to the domain wall, on the tail side (crystal co-ordinates 0.7) it is in its ground state position. If the domain wall continues to move the vacancy transforms to the high-energy equatorial state depicted on the left side of the figure.

distances are measured in the column adjacent to that containing the oxygen vacancy. We see a much sharper peak in the c-to-a transition at the tail side of the domain wall than in the absence of oxygen vacancy (compare with Fig. 7.1(a)). This is qualitatively similar to experiments in Fig. 7.1(b). This seems to suggest that the structure of the 90° domain wall observed using STEM may already be influenced by the presence of oxygen vacancies. From Fig. 7.6(b) we see that oxygen vacancies induce a very large c/a ratio close to the domain wall. Such a large effect is due to our relatively small supercell limiting our study to a large vacancy concentration at the domain wall. At lower concentrations the extent of tetragonality increment induced at the domain wall would likely be smaller in magnitude and agree more with experimental observations.
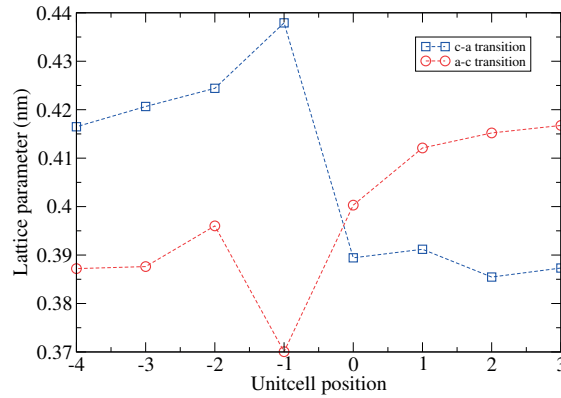
(a) Lattice parameter variation across the domain wall in the presence of an oxygen vacancy.
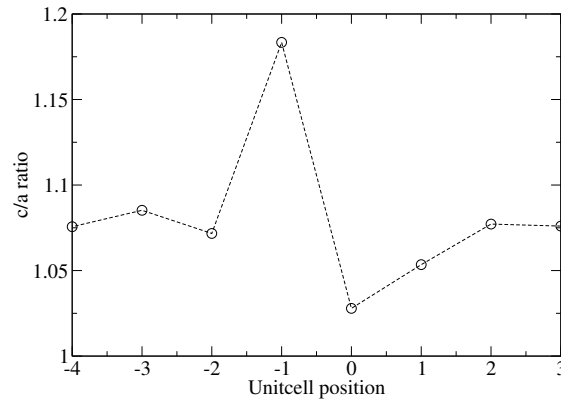
(b) c/a ratio across the domain wall in the presence of apical oxygen vacancy.

Figure 7.6: Effect of oxygen vacancies on the structure of the domain wall in first-principles calculations.

7.3 Interaction with lead vacancies and V''_{Pb}-$V^{\cdot\cdot}_O$

Besides oxygen vacancies there are a few other types of possible defects in undoped PbTiO$_3$ and PZT. Due to the evaporation of lead oxide, both lead vacancies as well as lead-oxygen divacancies are thought to be present. Fig. 7.7 depicts the stability of lead vacancies at the domain wall while Fig. 7.8 shows the stability of a particular type of lead-oxygen divacancy at the domain wall. We looked at divacancies between a lead vacancy and a nearest neighbor oxygen vacancy, as shown in Fig. 7.9.

7.4 Interaction with acceptor and donor dopants

In order to complete the investigation of defects with domain walls we looked at the interaction of domain walls with acceptor dopants (Fe) and donor dopants (Nb,La). The energy landscape of these substitutional defects in the vicinity of this domain wall is shown in Fig. 7.10.
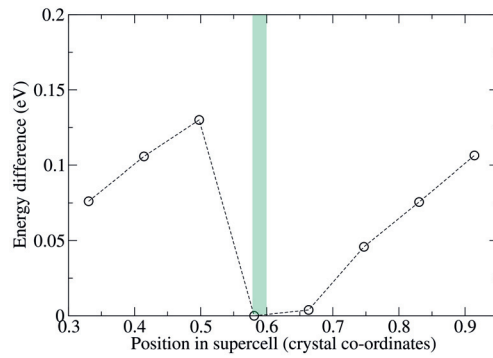
Figure 7.7: Graph illustrating the pinning of a 90° domain walls by lead vacancies.
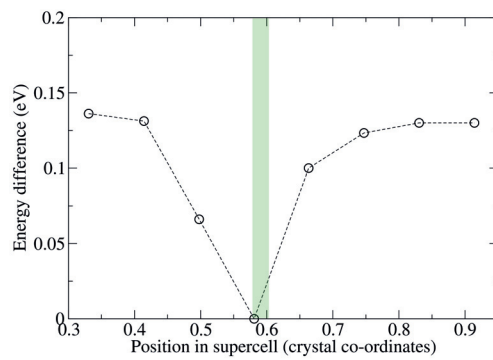
Figure 7.8: Graph illustrating the pinning of a 90° domain walls by a lead-oxygen divacancy V''_{Pb}-$V^{\cdot\cdot}_O$.
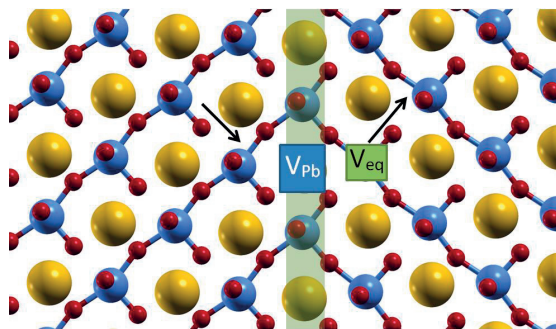
Figure 7.9: Schematics illustrating the ground state position of a V''_{Pb}-$V^{\cdot\cdot}_O$ divacancy.

We see that acceptor dopants exhibit much stronger pinning compared to donor dopants.
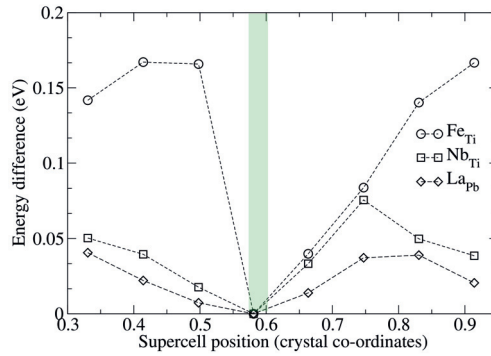
Figure 7.10: Graph illustrating the pinning of 90° domain walls by acceptor and donor dopants.

7.5   Summary

In conclusion, we observe a strong structural asymmetry at 90° domain walls in PbTiO$_3$; this is likely due to the polarization discontinuity predicted earlier for such interfaces [112]. We also highlight the presence of a plane with a large tetragonality on the tail side of the domain wall. These results indicate that modifications to the prevailing continuum theories of domain structure in ferroelectrics are required. The plane adjacent to the domain wall on the tail shows an attractive potential to oxygen vacancies. Due to energetically non-degenerate oxygen vacancies, the material is likely to exhibit two types of pinning depending on temperature. In a low-temperature disordered state, random-field pinning is likely. At higher temperatures and longer timescales, oxygen vacancies will accumulate on the tail side of the domain wall and cause random-bond pinning. The presence of aggregated vacancies at the domain wall may give rise to some unique behaviors. Conduction due to defect-mediated charge hopping is one of the phenomena that is thought to occur at certain domain wall interfaces [118]. Using a combination of temperature and directional electric field one may pin domain walls in specific locations using oxygen vacancies thus paving a way for domain-patterned nano-devices. Further calculations on the electronic properties of this wall are necessary to fully understand and take advantage of this phenomena.

Furthermore, lead vacancies, lead-oxygen divacancies and acceptor substitutional defects also have strong pinning effects on 90° ferroelectric domain walls. Donor substitutional defects on the other hand display very mild pinning characteristics. These results are discussed further in Chap. 9.

8 Charged domain walls

The presence of electrical conductance at ferroelectric domain walls has attracted much interest recently and opens the doors for nanoelectronics based on domain walls. In the seminal paper by Seidel *et al.* [114], nano-scale room temperature conductivity was observed in 109° and 180° domain walls of $BiFeO_3$. Using density-functional theory they attributed this conductivity to the presence of a jump in the electrostatic potential at such type of walls.This sparked extensive theoretical [161–164] and experimental [36, 165, 166] investigations of domain-wall based conductivity in $BiFeO_3$. In 2011, Guyonnet *et al.* [118] observed conductivity in nominally "neutral" 180° walls of PZT.

In the case of bulk $BaTiO_3$ crystals, Sluka *et al.* [29] controlled the applied electric field direction for a particular crystallographic orientation to single out charged domain walls and eliminate competing neutral domain-wall configurations. For many years, the existence of such charged domain walls had been questioned, due to associated large depolarizing fields. However, Sluka *et al.*, showed that head-to-head 90° domain walls displayed very strong metallic conductivity many orders of magnitude higher than the bulk. The position of such interfaces could also be controlled by the application of an electric field. Maksymovych *et al.* [167] reported tunable metallic conductivity in nano-domains of PZT and they attributed this to charged domain walls formed during polarization reversal. In the case of thin films, both 180° and 90° charged walls were present naturally in the sample without any external manipulations [168, 169].

8.1 90° charged domain wall in PbTiO$_3$

The calculation parameters were identical to that mentioned in Sec. 3.5. We first obtained a partially relaxed structure of a 60-atom charged domain-wall supercell as shown in Fig. 8.1. Due to the large electric fields across the domain wall, the configuration was not stable. Even with large supercell lengths the atoms would move and collapse the structure into a single domain state. To make progress, only the atoms in the region of the domain wall were allowed to relax. Supercells of different lengths were constructed and their electrostatic potentials are plotted in Fig. 8.2. We see the presence of a see-saw patterns due to the charges at the domain

walls. The density of states did not show a clear band gap and states were also present at the Fermi level. A projected density of states (PDOS) was then performed to pin-point any metallic behavior. We considered 5-atom unit cells at different positions in the supercell. The unit cells are labeled according to the legend shown in 8.1. Unit cell 1 is close to the tail-to-tail domain wall while the unit cell 7 is close to the head-to-head domain wall. Unit cell 4 is away from the two domain walls and displays a projected density of states very similar to bulk insulating $PbTiO_3$ (Fig. 8.3(b)). Unit cell 7 on the other hand has the Ti-d bands touching the Fermi level as depicted in Fig. 8.3(c) .These are the bands which contribute to the observed quantum 2-D electron gas. In unit cell 1 the Fermi level overlaps with the oxygen p states in the valence band as illustrated in Fig. 8.3(a).
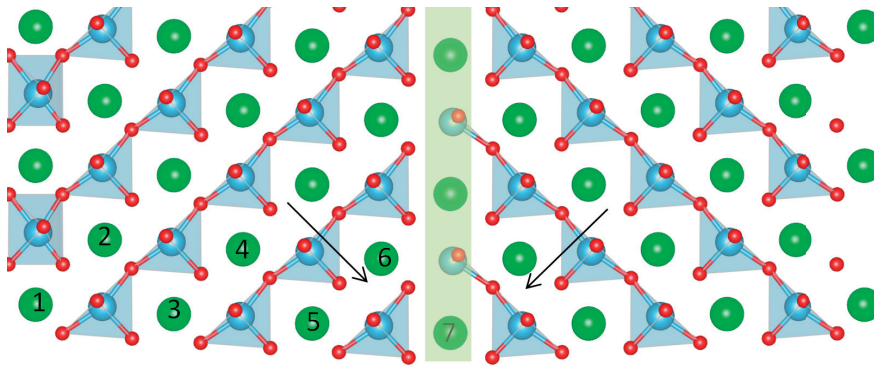
Figure 8.1: Schematic of a charged domain-wall supercell showing the positions of the head-to-head and tail-to-tail domain walls. Atom 1 is located at the tail-to-tail wall while atom 7 is located at the head-to-head wall.
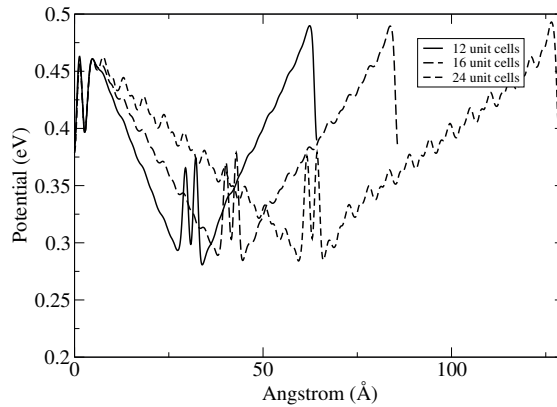
Figure 8.2: Potential across charged domain wall on supercells of different lengths.

8.2 180° charged domain wall and oxygen vacancy alignment in BaTiO$_3$

The polarization discontinuity at these domain walls gives rise to a large interface charge and associated electric field which should render these walls highly unstable. Hence, some type of charge compensation is required; either through electrons/holes or through charged

(a) PDOS at tail-to-tail domain wall.

(b) PDOS away from domain walls.

(c) PDOS at head-to-head domain wall in the bulk.

Figure 8.3: The projected density of states (PDOS) for different parts of the charged domain wall supercell.

defects. Experiments by Sluka *et al* [30]., have shown that head-to-head domain walls are at least partially stabilized by the appearance of a 2-D electron gas at the interface, reminiscent of that found at LaAlO$_3$/SrTiO$_3$ interfaces [31]. On the other hand, tail-to-tail domain walls displayed much smaller conductivity; the presence of charged oxygen vacancies at tail-to-tail domain walls may explain the lower values.

Oxygen vacancies are thought to be the most abundant defects in most perovskite oxides. Under many conditions, doubly charged oxygen vacancies have an exothermic formation energy [104]. The mobility/migration of these vacancies results in a variety of interesting phenomena in ferroelectrics. Such vacancies distribute inhomogeneously in the presence of an electric field [170–174]. Due to the symmetry-breaking ferroelectric phase transition, certain configurations of defects and defect associates [49, 61, 66, 105, 106, 134, 138, 141, 154, 175, 176] become more energetically favorable compared to others.

The atomistic interaction between defects and charged domain walls has not yet been reported and its experimental study is exceedingly difficult. To understand the compensation of charges within nominally charged walls, it thus becomes necessary to use computational methods in addition to indirect experimental studies. In this section we look at the behavior of clusters of oxygen vacancies through first-principles calculations. We show how different types of oxygen

vacancies prefer to align along certain directions and how such clusters can help nucleate arrays of charged domain walls in the paradigmatic ferroelectric $BaTiO_3$.

8.2.1 Oxygen vacancy alignment

Here, we study the higher temperature tetragonal phase of $BaTiO_3$; due to the tetragonal symmetry, there exist two oxygen positions: The first is the apical position (V_{ax}) at the apex of the oxygen cage and the second is the equatorial position (V_{eq}).

We investigate the structural deformations around both type of vacancies using a 3*3*3 super-cell containing 135 atoms. In this case, since supercells contain charged defects, a compensating jellium background of opposite charge is automatically included to remove electrostatic divergencies. In the case of the apical oxygen vacancy, there is a strong displacement of the titanium atom (0.36 Å with respect to its initial position) in the opposite direction of the bulk ferroelectric displacement, as shown in Fig.8.4(a), whereas for the equatorial oxygen vacancy there is a strong displacement of the neighboring Ti atoms in the direction perpendicular to polarization (0.21 Å with respect to the initial position), as depicted in Fig.8.4(b). The apical oxygen vacancy is only 78 meV more stable than the equatorial oxygen vacancy and this is in qualitative agreement with hybrid-DFT calculations by Shimada *et al.* [104]. What we observe is that such charged oxygen vacancies produce much stronger distortions of the surrounding polarization compared to neutral oxygen vacancies. Hence, it becomes interesting to see whether clusters of such defects would arrange themselves to optimize the electrostatic environment.

Thus, we look whether there is a tendency for pairs of such vacancies to order themselves. First, we compare the apical vacancy ordering in the [001] direction to the [100] direction as shown Fig. 8.5. Note that the [001] direction is along the polarization direction while the [100] direction is perpendicular to the polarization direction. If the two apical oxygen vacancies are ordered along the [001] direction, there is less space for lattice relaxation due to competing displacements of the titanium ion centered between the two vacancies. On the other hand, if the vacancies are ordered along the [100] direction, lattice relaxation can take place easily. Due to this, we observe that ordering along the [100] direction is 2.48 eV more stable compared to ordering along [001].

We realize that performing a calculation involving 2 vacancies in a 3*3*3 supercell could bring strong interactions with the periodic images of the defects. Hence, the same nearest-neighbor configuration shown in Fig. 8.5 was investigated in a 4*4*4 supercell. In this case, the energy difference between nearest-neighbor [001] ordering and [100] ordering was 2.4 eV. This shows that our calculations are reasonably well converged with respect to the size of supercell. Since the calculation of absolute defect formation energies requires even larger supercells [177], we consider here only energy differences for clusters of oxygen vacancies.

In order to see if long-range interactions are possible, we also looked at next nearest-neighbor

interactions in the 4*4*4 supercell, as depicted in Fig. 8.6. Even though the two vacancies are located relatively further apart, we still see strong defect interactions mediated through large lattice displacements. For the case of next neighbor interactions ordering along the [100] direction is 0.77 eV more favorable compared to ordering along [001]. Since 0.77 eV is qualitatively similar to the activation energy for oxygen vacancy migration [44, 59, 159], we may expect that long-range interaction and ordering may take place through oxygen-vacancy diffusion.

Equatorial vacancies, on the other hand, are preferably ordered in the [001] direction compared to the [100] direction, as shown in Fig. 8.7. The underlying principle of ordering is the same in both types of vacancies, and the only difference is that apical vacancies order perpendicular to the direction of lattice polarization, while equatorial vacancies are ordered along the direction of lattice polarization. From these results one may suspect that apical oxygen vacancies may nucleate tail-to-tail 180° domain walls. With this thought in mind, it is of interest to better understand the effect of a dense array of oxygen vacancies on the polarization of surrounding unit cells.
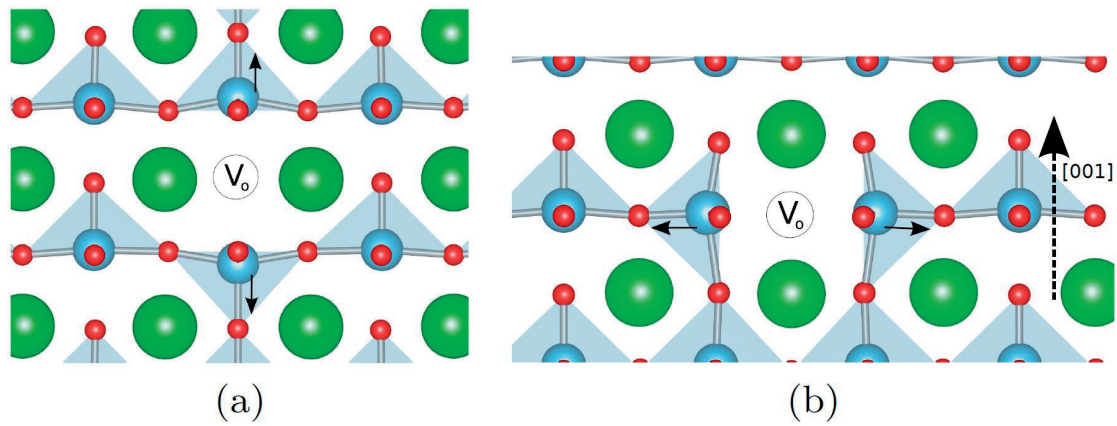
Figure 8.4: Displacements produced by two different types of oxygen vacancies - (a) apical and (b) equatorial. Black arrows indicate the direction of the titanium ions displacements. The large/green spheres are barium atoms, the smaller/blue ones are titanium atoms and the smallest/red are oxygen atoms. The lattice polarization in all figures in this chapter is in the [001] direction, as shown by the upward pointing translucent oxygen polyhedra, and, in this figure, the dashed black arrow.

8.2.2 Formation of tail-to-tail domain wall

We performed calculations on a 2*2*8 supercell of BaTiO$_3$ with one apical oxygen vacancy located at the central longitudinal plane of the supercell as depicted schematically in Fig.8.8(a) (the top view, is shown in Fig.8.8(b)). The columns are numbered I to IV and the oxygen vacancy is located in the middle of column I. The initial polarization of all the columns in the supercell is in the [001] direction. We allowed the atoms to relax to their equilibrium positions and then observed the effect of the oxygen vacancy on neighboring unit cells. Using Born
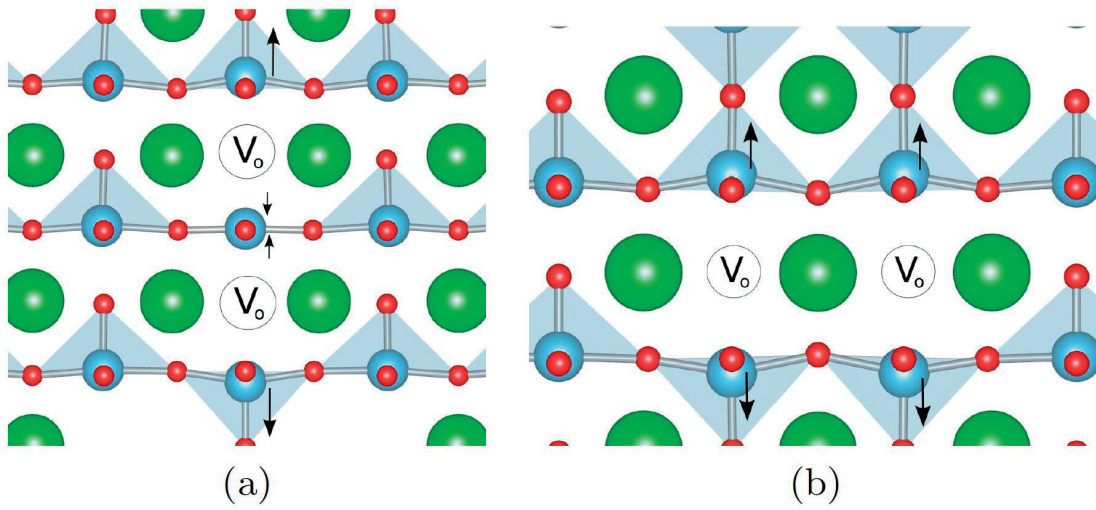
Figure 8.5: Aligning of apical oxygen vacancies in the (a) [001] and (b) [100] directions. Aligning along [100] is energetically more favorable by 2.48 eV.
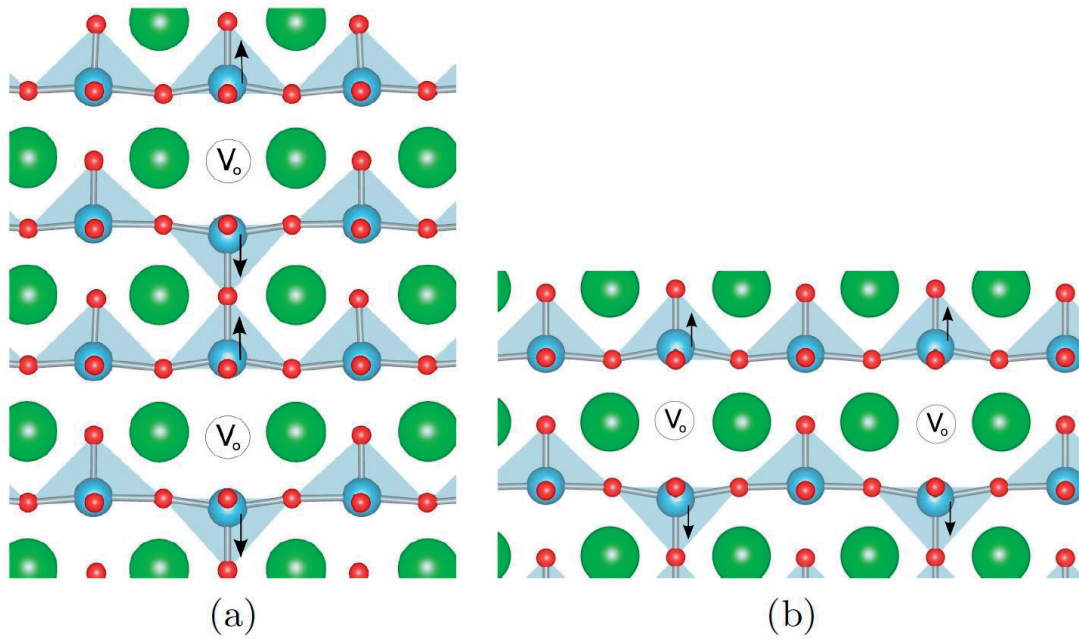
Figure 8.6: Aligning of next-nearest neighbor apical oxygen vacancies in the (a) [001] and (b) [100] directions. Aligning along [100] is energetically more favorable by 0.77 eV.

effective charges calculated for cubic $BaTiO_3$ [178], we analyzed the polarization per 5-atom Ti-centered unit cell across all four columns. To be specific, the 8 barium atoms were chosen as the corners of every unit cell and the titanium atoms were in the center of the 6-atom oxygen octahedra. The displacements of each atom in this unit cell were considered with respect to the lower basal Ba-O plane of each cell. The rows (unit cell position) are numbered
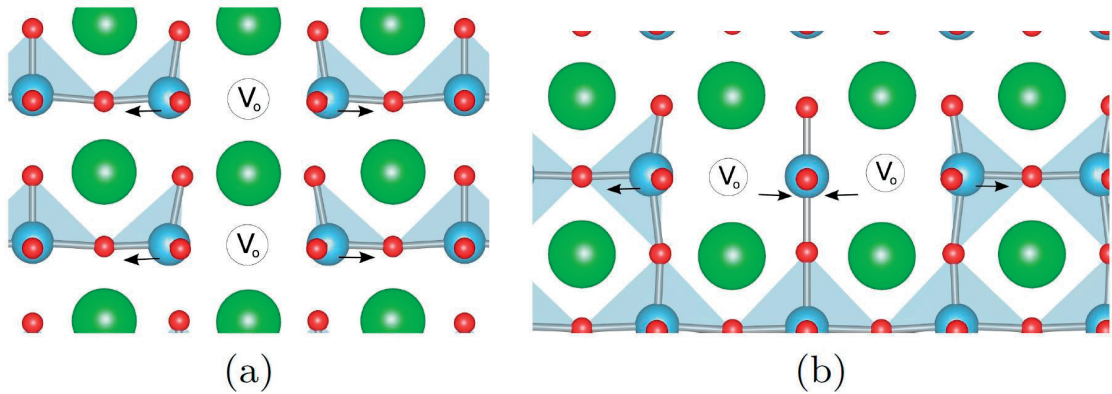
Figure 8.7: Aligning of equatorial oxygen vacancies in the (a) [001] and (b) [100] directions. Aligning along [001] is energetically more favorable by 2.35 eV.

according to Fig.8.8(a). The two unit cells adjacent to the oxygen vacancy (in column I) were not considered because of the ambiguity of the polarization in the vicinity of the oxygen vacancy. Note that using the cubic Born effective charges gives a bulk polarization of BaTiO$_3$ of 0.27 C/m^2 in good agreement with the experimental results [179] of 0.26 C/m^2. Due to charge screening effects and the localized nature of the charged oxygen vacancy (Fig.8.8(a)), the Born effective charges should still be approximately valid for this charged supercell, although the polarization presented here is just a convenient method to understand the structural deformations surrounding oxygen vacancy clusters. The polarization profiles for columns I, II and III are shown in Fig. 8.9. The oxygen vacancy itself is located in column I between rows 4 and 5. The rows 1-3 are located above the vacancy, while rows 6-8 are located below the vacancy. By symmetry, the columns II and IV display identical ionic displacements; hence, we do not show the polarization profile for column IV.

In the case of column I, the polarization is positive ($+z$ direction) above the vacancy and negative below the vacancy. We see that the positively charged oxygen vacancy can screen and invert the polarization charge within the same column. However, it is interesting to see the effect of the vacancies in neighboring columns. In the case of column II, we observe no reversal of polarization, which remains in the $+z$ direction. However, there is a decrease in the magnitude of the polarization below the vacancy (rows 5-7). Hence, the oxygen vacancy in column I cannot effectively invert the polarization in column II. However, we observe that in the case of column III there is a complete reversal of polarization across all rows, and that the oxygen vacancy has a much stronger effect across the [110] direction as compared to the [100] direction. The reason for this may be related to charge screening by negatively charged oxygen atoms. We see that there is a column of equatorial oxygen atoms separating columns I and II. However, there is no such screening effect in the [110] direction. This observation is very interesting as it gives insight into the polarization-switching dynamics. We see that polarization switching is more likely to propagate along the [110] direction compared to the [100] direction.
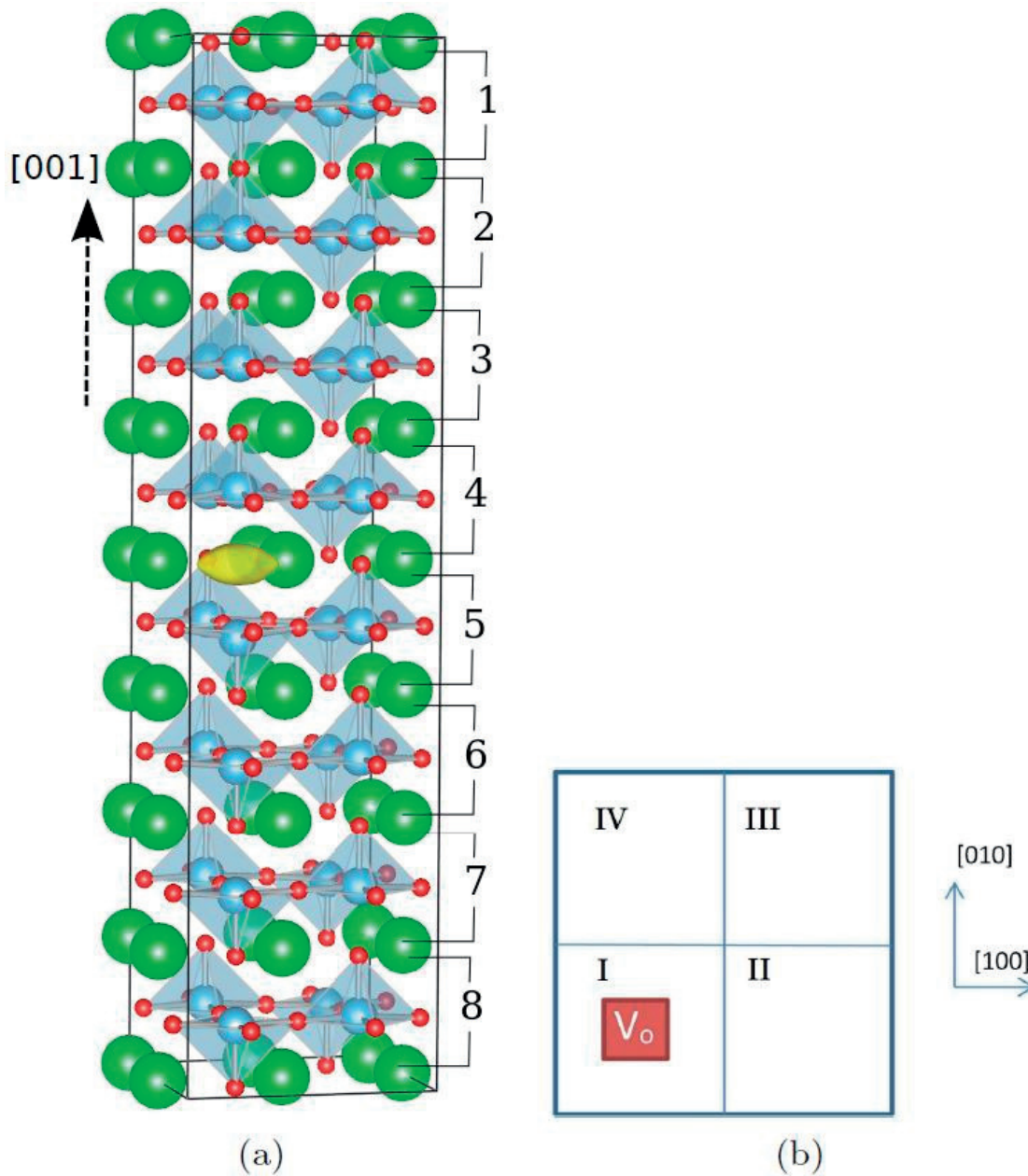
Figure 8.8: (a) 180° charged domain wall separated by an oxygen vacancy in the (001) plan. The oxygen vacancy charge density is shown by the yellow isosurface. The numbers label the unit cell positions for calculations of the local polarization as shown later in Fig. 8.9. (b)Top view of the (001) plane with the oxygen vacancy located in column I.

When a continuous line of two vacancies is placed on the plane, instead of just one (either in the [110] or [100] directions) we observe complete screening and inversion of polarization. Fig. 8.10 depicts the polarization profile for the [100] case, where we observe a clear tail-to-tail domain wall along the oxygen vacancies and a head-to-head domain wall at the boundaries of
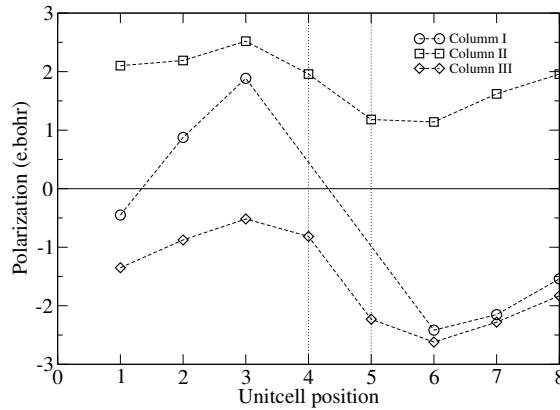
Figure 8.9: Polarization profile across the 2*2*8 supercell studied. The oxygen vacancy is located between rows 4 and 5. Rows 1-3 are located above the oxygen vacancy while rows 6-8 are located below.

the supercell. We see that a significant concentration of apical oxygen vacancies are required to create a charged 180° wall. We performed a density-of-states calculation to see if any of the planes of this charged domain-wall supercell are metallic. Fig. 8.11 shows the the density of states calculation for oxygen vacancies aligned continuously along [100] direction: We observe only a slight reduction of the band gap compared to bulk BaTiO$_3$. Hence, unlike charged 90° domain walls, the 180^0 head-to-head domain wall does not display metallic characteristics. Since the unit cells in the vicinity of the head-to-head wall are almost unpolarized, the head-to-head domain wall likely does not require any other form of compensation. In retrospect, the lack of metallic behavior in the supercell allows us to investigate meaningfully structural variations using Born effective charges.
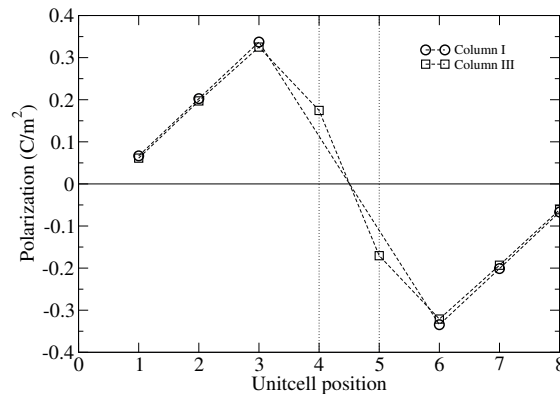
Figure 8.10: Polarization profile across the supercell containing two vacancies aligned in the [100] direction. The oxygen vacancies are located between rows 4 and 5. Rows 1-3 are located above the oxygen vacancies while rows 6-8 are located below. Columns II and IV are symmetrically equivalent to columns I and III, respectively; hence, their polarization profile is not shown.
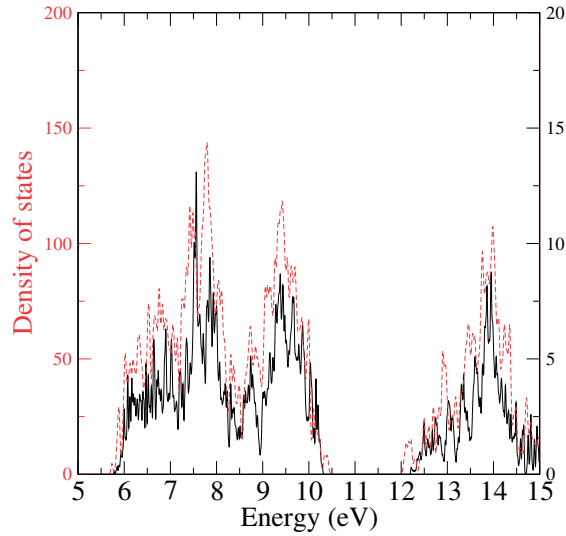
Figure 8.11: Density of states for a supercell containing oxygen vacancies aligned continuously along the [100] direction (dashed red line), in comparison with the density of states of bulk BaTiO$_3$ (black line). Only a slight reduction in band gap is observed.

8.3   Summary

To summarize, in our calculations we observe that different types of doubly-charged oxygen vacancies induce different lattice displacements in their vicinity. The apical oxygen vacancy induces strong displacement in the direction anti-parallel to that of the bulk polarization, while the equatorial vacancy induces a displacement perpendicular to the bulk polarization. We observed that both types of oxygen vacancies have certain relative positions to accommodate the lattice relaxation. We also consider the screening effects of apical oxygen vacancies and show that these defects are more effective in inverting polarization along the [110] direction compared to the [100] direction. The presence of a continuous line of oxygen vacancies can produce complete screening of the polarization charge and induces the formation of charged domain walls. Although such high densities of oxygen vacancies are unlikely to appear throughout the material, one may expect clusters with large concentration of oxygen vacancies, especially at the surfaces, thin film interfaces, and grain boundaries. Hence, we propose that local clusters of oxygen vacancies may help to spontaneously nucleate charged 180° domain walls. Oxygen vacancy aligning has been proposed by Brennan [180] and also by Dawber and Scott [160]; however, this was in a phenomenological context that sought to provide insights into fatigue in ferroelectric oxides. The present work provides further microscopic understanding into the driving forces for clustering and for the mechanisms of charge screening by oxygen vacancies at strongly charged domain walls by oxygen vacancies.

9 Effect of donor dopants/defects on softening

The addition of aliovalent dopants to PZT induces changes in the defect chemistry of the material. The addition of acceptor dopants such as iron is thought to increase the oxygen-vacancy concentration while decreasing the lead-vacancy concentration. Donor dopants on the other hand are thought to increase the lead-vacancy concentration while decreasing the oxygen-vacancy concentration. Undoped PZT may have both oxygen and lead vacancies at different concentrations depending on the oxygen partial pressure while sintering and also on the impurities present in the material. Quantitative and systematic measurements of these effects on PZT are exceedingly difficult. Direct experiments like positron lifetime measurements or electron paramagnetic resonance are not easy to interpret.

In this chapter we try to understand the effect of donor dopants on the defect chemistry by comparing ab intio calculations with experimental observations.

9.1 Effect of dopants on PbO evaporation

During the sintering process, a certain amount of PbO evaporation takes place even though one tries to minimize this process by controlling the sintering environment/atmosphere. This evaporation process inevitably results in the presence of oxygen and lead vacancies. Our idea was that acceptor/donor dopants may have different effects on the thermodynamics of this evaporation process.

The goal was to find the formation energy of the V_{Pb}''-$V_O^{\cdot\cdot}$ divacancy in the presence of both acceptor and donor dopants. For example, the formation energy of V_{Pb}''-$V_O^{\cdot\cdot}$ in the case of PbTiO$_3$ with iron acceptor dopant would be given by,

$$H_{V_{Pb}''-V_O^{\cdot\cdot}}^{formation} = E_{PbO} + E'_{\left(V_{Pb}''-V_O^{\cdot\cdot}-Fe'_{Ti}\right)} - E_{Fe'_{Ti}} \tag{9.1}$$

Dopant	Acceptor/Donor	Formation energy of $V_{Pb}^{''}$-$V_O^{\cdot\cdot}$ divacany
Fe	Acceptor	0.97
Undoped		2.16
Nb	Donor	2.55
La	Donor	2.69

Table 9.1: $V_{Pb}^{''}$-$V_O^{\cdot\cdot}$ divacany formation energy in the presence of acceptor and donor dopants.

There are three types of point defects involved in this calculation; the lead vacancy ($V_{Pb}^{''}$), the oxygen vacancy ($V_O^{\cdot\cdot}$) and the iron substitutional defect $Fe_{Ti}^{'}$. These three defects may be arranged in many different configurations. We calculated the energy for a variety of different configurations and looked for the minimum energy configuration. The ground state configuration for this defect associate in the presence of iron substitutional defect is depicted in Fig. 9.1. The total energy of the ground state PbO (litharge) (E_{PbO}) is also calculated.
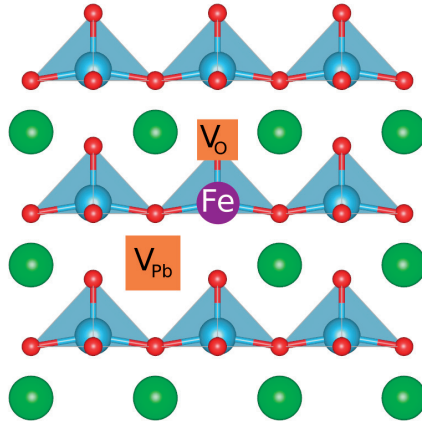
Figure 9.1: Ground state configuration of the lead-oxygen divacancy in the presence of iron substitutional dopant in a 3*3*3 supercell.

The same procedure was repeated for pure $PbTiO_3$ as well as niobium-doped and lanthanum-doped $PbTiO_3$. The aim of these calculations was to find a qualitative trend in the divacancy formation energies in the presence of different dopants. From Tab. 9.1, we see that acceptor dopants decrease the formation energy of the $V_{Pb}^{''}$-$V_O^{\cdot\cdot}$ divacancy. Donor dopants on the other hand hinder PbO evaporation.

9.2 Discussion on softening

Earlier in Chap. 4, we observed the effect of small donor-dopant concentrations on the properties of PZT. The addition of small quantities of La or Nb results in porosity, lower densification and higher grain size [130]. This was initially attributed to the fact that these

donor dopants occupy pre-existing lead vacancy sites and thus reduce the volume diffusion during sintering [129]. However, a very different behavior was observed by Morozov *et al.* [64] on addition of small amounts of acceptor dopants. Specifically, the addition of even 0.1% Fe acceptor-dopant resulted in very small grain sizes and good densification [64]. This observation may point to the fact that volume diffusion is higher in acceptor doped materials due to higher concentrations of lead vacancies. Indeed, based on our calculations, we see that lead oxide evaporation is significantly increased in the presence of acceptor dopants while it is hindered by the presence of donor dopants.

Traditionally, it is thought that acceptor dopants cause oxygen vacancies while hindering lead vacancy formation in order to preserve electroneutrality. While this may still be true, the formation of divacancies through PbO evaporation is an overall neutral process. Hence, for low dopant concentrations, samples with acceptor dopants are likely to have more lead and oxygen vacancies compared to pure PZT. Samples with low concentrations of donor dopants are likely to have lower lead-and oxygen-vacancy concentrations compared to pure PZT. At higher concentrations of donor dopants, electroneutrality conditions will lead to higher concentration of lead vacancies, while the oxygen-vacancy concentration will remain low. This is likely the reason why higher concentrations of donor dopants show an improvement in densification and lower grain sizes.

Based on the results of previous Chapters, we observe that pinning of both 90° and 180° domain walls is most likely caused by oxygen vacancies and also by polar defect associates involving oxygen vacancies. The suppression of lead oxide evaporation by donor dopant is likely to be the leading cause of softening. The lack of domain wall pinning, due to lower vacancy concentrations, explains why soft materials (even with just 0.5 at% Nb or La) have an open hysteresis loop. The lack of mobile oxygen vacancies also explains why the hysteresis loops of donor doped material is independent of the cooling rate. Softening is indeed caused by reduced pinning of domain walls; however one has to deviate from the simple traditional view that donor dopants cause lead vacancies and acceptor dopants cause oxygen vacancies. Rather, it is the opposing effects of donor and acceptor on PbO evaporation that leads to both the hardening and softening phenomena.

10 Conclusions and perspectives

An extensive investigation of the atomistic structure of domain walls in $PbTiO_3$ was conducted. Novel structural phenomena were observed both in the case of 180° and and 90° domain walls. The interactions of these domain walls with defects and defect associates were characterized. The behavior of oxygen-vacancy clusters and their relevance to tail-to-tail domain walls is also reported. Based on both experimental and computational evidence we propose novel ideas for the role of donor dopants in softening. The main results of this work may be listed as follows:

1. Polar defect associates such as Fe'_{Ti}-$V^{..}_O$ and V''_{Pb}-$V^{..}_O$ are likely to exist in Fe-acceptor doped and undoped $PbTiO_3$, respectively. These defect associates tend to align with the direction of lattice polarization. No such defect associate is formed in donor doped materials.

2. Both isolated defects and defect associates are attracted to 180° degree domain walls in $PbTiO_3$. Polar defect associates are very strong pinning centers and act as both random-bond and random-field defects due to their symmetry.

3. Contrary to prior reports, the 180° domain walls in $PbTiO_3$ are shown to have a large Bloch component for the polarization. The energy landscape for polarization rotation is very flat at the domain wall and it is sensitive to strain. Due to these characteristics, such walls are shown to have a large longitudinal piezoelecrtic coefficient.

4. An inherent asymmetry in the variation of the lattice parameter at neutral head-to-tail 90° domain walls of $PbTiO_3$ is identified and experimentally verified using aberration corrected high-resolution transmission-electron microscopy. Oxygen vacancies are attracted to the tail side of the wall and act as both random-bond and random-field defects. The energy landscapes of other defects and defect associates in the vicinity of 90° domain walls have also been characterized.

5. The electronic structure of a 90° charged domain wall in $PbTiO_3$ is analyzed. Due to the strong depolarizing field, the Fermi level overlaps with valence p-bands of the oxygen

73

at the tail-to-tail wall while the Fermi level overlaps with conduction d-bands of the titanium at the head-to-head domain wall.

6. Clusters of apical and equatorial oxygen vacancies are shown to align in [100] and [001] directions respectively in $BaTiO_3$. Apical oxygen vacancy alignment may result in the formation of tail-to-tail 180° domain walls. The polarization variation due to the presence of oxygen vacancies in such supercells is analyzed.

7. The effect of donor and acceptor dopant on PbO evaporation in $PbTiO_3$ is determined. Based on both experimental and computational results, acceptor dopants are shown to increase the concentration of lead and oxygen vacancies while donor dopants hinder the formation of such vacancies. Hence, samples with low dopant concentrations likely have a lower vacancy concentration compared to pure, undoped PZT. The lack of oxygen vacancies and polar defect associates allows unhindered domain wall movement in donor-doped soft PZT.

There are some foreseeable ways in which one may improve upon the calculations presented here. For example, we have avoided calculating absolute defect formation energies and charge transition levels. To obtain a quantitative estimation of such values, the use of hybrid functional [181] or many-body perturbation theory (GW) approaches is desired. Moreover, finite-size supercell correction schemes are also extremely important for such calculations [182]. Since we were interested in a qualitative comparison with experiments we utilized convention LDA and PBEsol functionals but performed calculations on system sizes of up to 240 atoms.

Besides shedding light on the phenomena of softening, the results of this work indeed point to the multi-faceted properties of domain walls. With a better understanding of the atomistic properties of these interfaces, one may try to capitalize on utilizing them as functional interfaces for nanoelectronics or even photovoltaics [183]. Although it may seem currently unfeasible, the flat energy landscape observed at 180° domains may possibly be utilized as a support for diffusion pathways in superionic materials.

.

[1] M. E. Lines and A. M. Glass, *Principles and applications of ferroelectrics and related materials*. Oxford University Press, 1977.

[2] J. Valasek, "Piezo-electric and allied phenomena in Rochelle salt," *Physical Review*, vol. 17, no. 4, p. 475, 1921.

[3] G. H. Haertling, "Ferroelectric ceramics: history and technology," *J. Am. Ceram. Soc.*, vol. 82, no. 4, pp. 797–818, 1999.

[4] R. Gray, "Transducer and method of making the same," 1949. US Patent 2,486,560.

[5] G. Shirane and S. Hoshino, "On the phase transition in lead titanate," *Journal of the Physical Society of Japan*, vol. 6, no. 4, pp. 265–270, 1951.

[6] B. Jaffe, W. R. Cook, and H. Jaffe, *Piezoelectric ceramics*. Academic press London, 1971.

[7] V. Isupov, "Comments on the paper "x-ray study of the PZT solid solutions near the morphotropic phase transition"," *Solid State Communications*, vol. 17, no. 11, pp. 1331–1333, 1975.

[8] K. Kakegawa, J. Mohri, T. Takahashi, H. Yamamura, and S. Shirasaki, "A compositional fluctuation and properties of Pb (Zr,Ti)O_3," *Solid State Communications*, vol. 24, no. 11, pp. 769–772, 1977.

[9] S. Mishra, D. Pandey, and A. P. Singh, "Effect of phase coexistence at morphotropic phase boundary on the properties of Pb($Zr_x Ti_{1-x}$)O_3 ceramics," *Applied Physics Letters*, vol. 69, no. 12, pp. 1707–1709, 1996.

[10] A. Glazer, P. Thomas, K. Baba-Kishi, G. Pang, and C. Tai, "Influence of short-range and long-range order on the evolution of the morphotropic phase boundary in Pb($Zr_{1-x} Ti_x$)O_3," *Physical Review B*, vol. 70, no. 18, p. 184123, 2004.

[11] W. Cao and L. E. Cross, "Theoretical model for the morphotropic phase boundary in lead zirconate–lead titanate solid solution," *Physical Review B*, vol. 47, no. 9, p. 4825, 1993.

[12] B. Noheda, D. Cox, G. Shirane, J. Gonzalo, L. Cross, and S. Park, "A monoclinic ferro-electric phase transition in the $Pb(Zr_{1-x}Ti_x)O_3$ solid solution," *Applied Physics Letters*, vol. 74, no. BNL–80697-2008-JA, 1999.

[13] L. Bellaiche, A. García, and D. Vanderbilt, "Finite-temperature properties of $Pb(Zr_{1-x}Ti_x)O_3$ alloys from first principles," *Physical Review Letters*, vol. 84, no. 23, p. 5427, 2000.

[14] G. Arlt, "Twinning in ferroelectric and ferroelastic ceramics: stress relief," *Journal of Materials Science*, vol. 25, no. 6, pp. 2655–2666, 1990.

[15] L. A. Schmitt, K. A. Schönau, R. Theissmann, H. Fuess, H. Kungl, and M. J. Hoffmann, "Composition dependence of the domain configuration and size in $Pb(Zr_{1-x}Ti_x)O_3$ ceramics," *Journal of Applied Physics*, vol. 101, no. 7, p. 074107, 2007.

[16] R. Theissmann, L. A. Schmitt, J. Kling, R. Schierholz, K. A. Schönau, H. Fuess, M. Knapp, H. Kungl, and M. J. Hoffmann, "Nanodomains in morphotropic lead zirconate titanate ceramics: On the origin of the strong piezoelectric effect," *Journal of Applied Physics*, vol. 102, no. 2, p. 024111, 2007.

[17] R. Schierholz, H. Fuess, K. Tsuda, Y. Ogata, M. Terauchi, and R. Theissmann, "Crystal symmetry in single domains of $PbZr_{0.54}Ti_{0.46}O_3$," *Physical Review B*, vol. 78, no. 2, p. 024118, 2008.

[18] J. Fousek and V. Janovec, "The orientation of domain walls in twinned ferroelectric crystals," *Journal of Applied Physics*, vol. 40, no. 1, pp. 135–142, 1969.

[19] Q. Zhang, W. Pan, S. Jang, and L. Cross, "Domain wall excitations and their contributions to the weak-signal response of doped lead zirconate titanate ceramics," *Journal of Applied Physics*, vol. 64, no. 11, pp. 6445–6451, 1988.

[20] Q. Zhang, H. Wang, N. Kim, and L. Cross, "Direct evaluation of domain-wall and intrinsic contributions to the dielectric and piezoelectric response and their temperature dependence on lead zirconate-titanate ceramics," *Journal of Applied Physics*, vol. 75, no. 1, pp. 454–459, 1994.

[21] C. A. Randall, N. Kim, J.-P. Kucera, W. Cao, and T. R. Shrout, "Intrinsic and extrinsic size effects in fine-grained morphotropic-phase-boundary lead zirconate titanate ceramics," *Journal of the American Ceramic Society*, vol. 81, no. 3, pp. 677–688, 1998.

[22] D. Damjanovic, "Contributions to the piezoelectric effect in ferroelectric single crystals and ceramics," *Journal of the American Ceramic society*, vol. 88, no. 10, pp. 2663–2676, 2005.

[23] G. Arlt, "The role of domain walls on the dielectric, elastic and piezoelectric properties of ferroelectric ceramics," *Ferroelectrics*, vol. 76, no. 1, pp. 451–458, 1987.

[24] R. Herbiet, U. Robels, H. Dederichs, and G. Arlt, "Domain wall and volume contributions to material properties of PZT ceramics," *Ferroelectrics*, vol. 98, no. 1, pp. 107–121, 1989.

[25] G. Arlt, "Microstructure and domain effects in ferroelectric ceramics," *Ferroelectrics*, vol. 91, no. 1, pp. 3–7, 1989.

[26] G. Arlt, "The influence of microstructure on the properties of ferroelectric ceramics," *Ferroelectrics*, vol. 104, no. 1, pp. 217–227, 1990.

[27] Q. Zhang, H. Wang, N. Kim, and L. Cross, "Direct evaluation of domain-wall and intrinsic contributions to the dielectric and piezoelectric response and their temperature dependence on lead zirconate-titanate ceramics," *Journal of Applied Physics*, vol. 75, no. 1, pp. 454–459, 1994.

[28] J. C. Wojdeł and J. Íñiguez, "Ferroelectric transitions at ferroelectric domain walls found from first principles," *Physical Review Letters*, vol. 112, no. 24, p. 247603, 2014.

[29] T. Sluka, A. K. Tagantsev, D. Damjanovic, M. Gureev, and N. Setter, "Enhanced electromechanical response of ferroelectrics due to charged domain walls," *Nature Communications*, vol. 3, p. 748, 2012.

[30] T. Sluka, A. K. Tagantsev, P. Bednyakov, and N. Setter, "Free-electron gas at charged domain walls in insulating $BaTiO_3$," *Nature Communications*, vol. 4, p. 1808, 2013.

[31] A. Ohtomo and H. Hwang, "A high-mobility electron gas at the $LaAlO_3/SrTiO_3$ heterointerface," *Nature*, vol. 427, no. 6973, pp. 423–426, 2004.

[32] J. A. Bert, B. Kalisky, C. Bell, M. Kim, Y. Hikita, H. Y. Hwang, and K. A. Moler, "Direct imaging of the coexistence of ferromagnetism and superconductivity at the $LaAlO_3/SrTiO_3$ interface," *Nature Physics*, vol. 7, no. 10, pp. 767–771, 2011.

[33] J. Seidel, D. Fu, S.-Y. Yang, E. Alarcón-Lladó, J. Wu, R. Ramesh, and J. W. Ager, "Efficient photovoltaic current generation at ferroelectric domain walls," *Physical Review Letters*, vol. 107, p. 126805, Sep 2011.

[34] S. Liu, F. Zheng, N. Z. Koocher, H. Takenaka, F. Wang, and A. M. Rappe, "Ferroelectric domain wall induced band gap reduction and charge separation in organometal halide perovskites," *The Journal of Physical Chemistry Letters*, vol. 6, no. 4, pp. 693–699, 2015.

[35] L. Feigl, P. Yudin, I. Stolichnov, T. Sluka, K. Shapovalov, M. Mtebwa, C. S. Sandu, X.-K. Wei, A. K. Tagantsev, and N. Setter, "Controlled stripes of ultrafine ferroelectric domains," *Nature Communications*, vol. 5, 2014.

[36] A. Crassous, T. Sluka, A. K. Tagantsev, and N. Setter, "Polarization charge as a reconfigurable quasi-dopant in ferroelectric thin films," *Nature Nanotechnology*, vol. 10, pp. 614–618, 2015.

Bibliography

[37] L. McGilly, P. Yudin, L. Feigl, A. Tagantsev, and N. Setter, "Controlling domain wall motion in ferroelectric thin films," *Nature Nanotechnology*, vol. 10, pp. 145–150, 2015.

[38] F. Kulcsar, "Electromechanical properties of lead titanate zirconate ceramics modified with certain three-or five-valent additions," *Journal of the American Ceramic Society*, vol. 42, no. 7, pp. 343–349, 1959.

[39] F. Kulcsar, "Electromechanical properties of lead titanate zirconate ceramics modified with tungsten and thorium," *Journal of the American Ceramic Society*, vol. 48, no. 1, p. 54, 1965.

[40] R. Gerson, "Variation in ferroelectric characteristics of lead zirconate titanate ceramics due to minor chemical modifications," *Journal of Applied Physics*, vol. 31, pp. 188 –194, jan 1960.

[41] R. Gerson and H. Jaffe, "Electrical conductivity in lead titanate zirconate ceramics," *Journal of Physics and Chemistry of Solids*, vol. 24, no. 8, pp. 979–984, 1963.

[42] E. T. Keve, K. L. Bye, P. W. Whipps, and A. D. Annis, "Structural inhibition of ferroelectric switching in triglycine sulphate additives," *Ferroelectrics*, vol. 3, no. 1, pp. 39–48, 1972.

[43] P. Lambeck and G. Jonker, "The nature of domain stabilization in ferroelectric perovskites," *Journal of Physics and Chemistry of Solids*, vol. 47, no. 5, pp. 453 – 461, 1986.

[44] W. L. Warren, K. Vanheusden, D. Dimos, G. E. Pike, and B. A. Tuttle, "Oxygen vacancy motion in perovskite oxides," *Journal of the American Ceramic Society*, vol. 79, no. 2, pp. 536–538, 1996.

[45] L. X. Zhang and X. Ren, "*In situ* observation of reversible domain switching in aged Mn-doped $BaTiO_3$ single crystals," *Physical Review B*, vol. 71, p. 174108, May 2005.

[46] Y. A. Genenko and D. C. Lupascu, "Drift of charged defects in local fields as aging mechanism in ferroelectrics," *Physical Review B*, vol. 75, p. 184107, May 2007.

[47] Y. A. Genenko, "Space-charge mechanism of aging in ferroelectrics: An analytically solvable two-dimensional model," *Physical Review B*, vol. 78, p. 214103, Dec 2008.

[48] Z. Feng and X. Ren, "Striking similarity of ferroelectric aging effect in tetragonal, orthorhombic and rhombohedral crystal structures," *Physical Review B*, vol. 77, p. 134115, Apr 2008.

[49] U. Robels and G. Arlt, "Domain wall clamping in ferroelectrics by orientation of defects," *Journal of Applied Physics*, vol. 73, no. 7, pp. 3454–3460, 1993.

[50] L. Zhang, E. Erdem, X. Ren, and R.-A. Eichel, "Reorientation of ($M_{Ti}^{''}$ - V_O) defect dipoles in acceptor-modified $BaTiO_3$ single crystals: An electron paramagnetic resonance study," *Applied Physics Letters*, vol. 93, no. 20, p. 202901, 2008.

78

[51] L. Jin, *Broadband Dielectric Response in Hard and Soft PZT*. PhD thesis, Thesis No. 4988, EPFL, 2011.

[52] K. Carl and K. H. Hardtl, "Electrical after-effects in Pb(Ti, Zr)O_3 ceramics," *Ferroelectrics*, vol. 17, no. 1, pp. 473–486, 1977.

[53] X. Ren, "Large electric-field-induced strain in ferroelectric crystals by point-defect-mediated reversible domain switching," *Nature Materials*, vol. 3, no. 2, pp. 91–94, 2004.

[54] V. Postnikov, V. Pavlov, and S. Turkov, "Internal friction in ferroelectrics due to interaction of domain boundaries and point defects," *Journal of Physics and Chemistry of Solids*, vol. 31, no. 8, pp. 1785 – 1791, 1970.

[55] W. L. Warren, D. Dimos, B. A. Tuttle, R. D. Nasby, and G. E. Pike, "Electronic domain pinning in Pb(Zr,Ti)O_3 thin films and its role in fatigue," *Applied Physics Letters*, vol. 65, no. 8, pp. 1018–1020, 1994.

[56] L. He and D. Vanderbilt, "First-principles study of oxygen-vacancy pinning of domain walls in PbTiO_3," *Physical Review B*, vol. 68, p. 134103, Oct 2003.

[57] M. Takahashi, "Space charge effect in lead zirconate titanate ceramics caused by the addition of impurities," *Japanese Journal of Applied Physics*, vol. 9, no. 10, pp. 1236–1246, 1970.

[58] P. Jakes, E. Erdem, R.-A. Eichel, L. Jin, and D. Damjanovic, "Position of defects with respect to domain walls in Fe^{3+}-doped Pb[Zr$_{0.52}$Ti$_{0.48}$]O_3 piezoelectric ceramics," *Applied Physics Letters*, vol. 98, no. 7, p. 072907, 2011.

[59] M. I. Morozov and D. Damjanovic, "Charge migration in Pb(Zr,Ti)O_3 ceramics and its relation to ageing, hardening, and softening," *Journal of Applied Physics*, vol. 107, no. 3, p. 034106, 2010.

[60] H. Mestric, R.-A. Eichel, K.-P. Dinse, A. Ozarowski, J. van Tol, and L. C. Brunel, "High-frequency electron paramagnetic resonance investigation of the Fe^{3+} impurity center in polycrystalline PbTiO_3 in its ferroelectric phase," *Journal of Applied Physics*, vol. 96, no. 12, pp. 7440–7444, 2004.

[61] R.-A. Eichel, P. Erhart, P. Träskelin, K. Albe, H. Kungl, and M. J. Hoffmann, "Defect-Dipole Formation in Copper-Doped PbTiO_3 Ferroelectrics," *Physical Review Letters*, vol. 100, p. 095504, Mar 2008.

[62] Y. Gao, K. Uchino, and D. Viehland, "Time dependence of the mechanical quality factor in "hard" lead zirconate titanate ceramics: Development of an internal dipolar field and high power origin," *Japanese Journal of Applied Physics*, vol. 45, no. 12, pp. 9119–9124, 2006.

[63] L. Zhang and X. Ren, "Aging behavior in single-domain Mn-doped $BaTiO_3$ crystals: Implication for a unified microscopic explanation of ferroelectric aging," *Physical Review B*, vol. 73, p. 094121, Mar 2006.

[64] M. Morozov, *Softening and hardening transitions in ferroelectric Pb(Zr,Ti)O$_3$ ceramics*. PhD thesis, Thesis No. 3368, EPFL, 2005.

[65] M. Morozov, D. Damjanovic, and N. Setter, "The nonlinearity and subswitching hysteresis in hard and soft PZT," *Journal of the European Ceramic Society*, vol. 25, no. 12, pp. 2483 – 2486, 2005.

[66] Q. Tan, J.-F. Li, and D. Viehland, "Ferroelectric behaviours dominated by mobile and randomly quenched impurities in modified lead zirconatetitanate ceramics," *Philosophical Magazine Part B*, vol. 76, no. 1, pp. 59–74, 1997.

[67] M. I. Morozov and D. Damjanovic, "Hardening-softening transition in Fe-doped $Pb(Zr,Ti)O_3$] ceramics and evolution of the third harmonic of the polarization response," *Journal of Applied Physics*, vol. 104, no. 3, p. 034107, 2008.

[68] L. Eyraud, B. Guiffard, L. Lebrun, and D. Guyomar, "Interpretation of the Softening Effect in PZT Ceramics Near the Morphotropic Phase Boundary," *Ferroelectrics*, vol. 330, no. 1, pp. 51–60, 2006.

[69] S. Gottschalk, H. Hahn, A. G. Balogh, W. Puff, H. Kungl, and M. J. Hoffmann, "A positron lifetime study of lanthanum and niobium doped $Pb(Zr_{0.6}Ti_{0.4})O_3$," *Journal of Applied Physics*, vol. 96, no. 12, pp. 7464–7470, 2004.

[70] P. Hohenberg and W. Kohn, "Inhomogeneous electron gas," *Physical Review*, vol. 136, no. 3B, p. B864, 1964.

[71] W. Kohn and L. J. Sham, "Self-consistent equations including exchange and correlation effects," *Physical Review*, vol. 140, no. 4A, p. A1133, 1965.

[72] P. A. Dirac, "Note on exchange phenomena in the thomas atom," in *Mathematical Proceedings of the Cambridge Philosophical Society*, vol. 26, pp. 376–385, Cambridge Univ Press, 1930.

[73] D. M. Ceperley and B. Alder, "Ground state of the electron gas by a stochastic method," *Physical Review Letters*, vol. 45, no. 7, p. 566, 1980.

[74] S. Vosko, L. Wilk, and M. Nusair, "Accurate spin-dependent electron liquid correlation energies for local spin density calculations: a critical analysis," *Canadian Journal of Physics*, vol. 58, no. 8, pp. 1200–1211, 1980.

[75] J. P. Perdew and A. Zunger, "Self-interaction correction to density-functional approximations for many-electron systems," *Physical Review B*, vol. 23, no. 10, p. 5048, 1981.

[76] L. A. Cole and J. Perdew, "Calculated electron affinities of the elements," *Physical Review A*, vol. 25, no. 3, p. 1265, 1982.

[77] J. P. Perdew and Y. Wang, "Accurate and simple analytic representation of the electron-gas correlation energy," *Physical Review B*, vol. 45, no. 23, p. 13244, 1992.

[78] J. P. Perdew and Y. Wang, "Accurate and simple analytic representation of the electron-gas correlation energy," *Physical Review B*, vol. 45, no. 23, p. 13244, 1992.

[79] J. P. Perdew, K. Burke, and M. Ernzerhof, "Generalized gradient approximation made simple," *Physical Review Letters*, vol. 77, no. 18, p. 3865, 1996.

[80] J. P. Perdew, A. Ruzsinszky, G. I. Csonka, O. A. Vydrov, G. E. Scuseria, L. A. Constantin, X. Zhou, and K. Burke, "Restoring the density-gradient expansion for exchange in solids and surfaces," *Physical Review Letters*, vol. 100, no. 13, p. 136406, 2008.

[81] D. Chadi and M. L. Cohen, "Special points in the Brillouin zone," *Physical Review B*, vol. 8, no. 12, p. 5747, 1973.

[82] H. J. Monkhorst and J. D. Pack, "Special points for Brillouin-zone integrations," *Physical Review B*, vol. 13, no. 12, p. 5188, 1976.

[83] R. Cohen and H. Krakauer, "Lattice dynamics and origin of ferroelectricity in $BaTiO_3$: Linearized-augmented-plane-wave total-energy calculations," *Physical Review B*, vol. 42, no. 10, p. 6416, 1990.

[84] R. E. Cohen, "Origin of ferroelectricity in perovskite oxides," *Nature*, vol. 358, no. 6382, pp. 136–138, 1992.

[85] D. Singh and L. Boyer, "First principles analysis of vibrational modes in $KNbO_3$," *Ferroelectrics*, vol. 136, no. 1, pp. 95–103, 1992.

[86] R. E. Cohen and H. Krakauer, "Electronic structure studies of the differences in ferroelectric behavior of $BaTiO_3$ and $PbTiO_3$," *Ferroelectrics*, vol. 136, no. 1, pp. 65–83, 1992.

[87] R. Resta, M. Posternak, and A. Baldereschi, "Towards a quantum theory of polarization in ferroelectrics: The case of $KNbO_3$," *Physical Review Letters*, vol. 70, no. 7, p. 1010, 1993.

[88] M. Posternak, R. Resta, and A. Baldereschi, "Role of covalent bonding in the polarization of perovskite oxides: the case of $KNbO_3$," *Physical Review B*, vol. 50, no. 12, p. 8911, 1994.

[89] D. J. Singh, "Stability and phonons of $KTaO_3$," *Physical Review B*, vol. 53, no. 1, p. 176, 1996.

[90] D. J. Singh, "Density functional studies of $PbZrO_3$, $KTaO_3$ and $KNbO_3$," *Ferroelectrics*, vol. 194, no. 1, pp. 299–322, 1997.

Bibliography

[91] I. Inbar and R. E. Cohen, "Origin of ferroelectricity in $LiNbO_3$ and LiTaO3," *Ferroelectrics*, vol. 194, no. 1, pp. 83–95, 1997.

[92] R. King-Smith and D. Vanderbilt, "A first-principles pseudopotential investigation of ferroelectricity in barium titanate," *Ferroelectrics*, vol. 136, no. 1, pp. 85–94, 1992.

[93] R. King-Smith and D. Vanderbilt, "First-principles investigation of ferroelectricity in perovskite compounds," *Physical Review B*, vol. 49, no. 9, p. 5828, 1994.

[94] A. García and D. Vanderbilt, "First-principles study of stability and vibrational properties of tetragonal $PbTiO_3$," *Physical Review B*, vol. 54, no. 6, p. 3817, 1996.

[95] R. Resta, "Theory of the electric polarization in crystals," *Ferroelectrics*, vol. 136, no. 1, pp. 51–55, 1992.

[96] R. Resta, "Macroscopic polarization in crystalline dielectrics: the geometric phase approach," *Reviews of Modern Physics*, vol. 66, pp. 899–915, Jul 1994.

[97] R. King-Smith and D. Vanderbilt, "Theory of polarization of crystalline solids," *Physical Review B*, vol. 47, no. 3, p. 1651, 1993.

[98] W. Zhong, R. King-Smith, and D. Vanderbilt, "Giant LO-TO splittings in perovskite ferroelectrics," *Physical Review Letters*, vol. 72, no. 22, p. 3618, 1994.

[99] P. Ghosez, X. Gonze, and J.-P. Michenaud, "Role of the coulomb interaction on the ferroelectric instability of barium titanate," *Ferroelectrics*, vol. 186, no. 1, pp. 73–76, 1996.

[100] R. Resta and S. Sorella, "Many-body effects on polarization and dynamical charges in a partly covalent polar insulator," *Physical Review Letters*, vol. 74, no. 23, p. 4738, 1995.

[101] R. Resta, "Role of covalence and of correlation in the dielectric polarization of oxides," *Ferroelectrics*, vol. 194, no. 1, pp. 1–9, 1997.

[102] C. Park and D. Chadi, "Microscopic study of oxygen-vacancy defects in ferroelectric perovskites," *Physical Review B*, vol. 57, no. 22, p. R13961, 1998.

[103] Y. Yao and H. Fu, "Charged vacancies in ferroelectric $PbTiO_3$: Formation energies, optimal fermi region, and influence on local polarization," *Physical Review B*, vol. 84, p. 064112, Aug 2011.

[104] T. Shimada, T. Ueda, J. Wang, and T. Kitamura, "Hybrid Hartree-Fock density functional study of charged point defects in ferroelectric $PbTiO_3$," *Physical Review B*, vol. 87, p. 174111, May 2013.

[105] H. Meštrić, R.-A. Eichel, T. Kloss, K.-P. Dinse, S. Laubach, S. Laubach, P. C. Schmidt, K. A. Schönau, M. Knapp, and H. Ehrenberg, "Iron-oxygen vacancy defect centers in $PbTiO_3$: Newman superposition model analysis and density functional calculations," *Physical Review B*, vol. 71, p. 134109, Apr 2005.

[106] P. Erhart, R.-A. Eichel, P. Träskelin, and K. Albe, "Association of oxygen vacancies with impurity metal ions in lead titanate," *Physical Review B*, vol. 76, p. 174116, Nov 2007.

[107] J. Padilla, W. Zhong, and D. Vanderbilt, "First-principles investigation of 180° domain walls in BaTiO$_3$," *Physical Review B*, vol. 53, no. 10, p. R5969, 1996.

[108] M. Tanaka and G. Honjo, "Electron optical studies of barium titanate single crystal films," *Journal of the Physical Society of Japan*, vol. 19, no. 6, pp. 954–970, 1964.

[109] L. Bulaevskii and V. Ginzburg, "Temperature dependence of the shape of the domain wall in ferromagnetics and ferroelectrics," *Sov. Phys. JETP*, vol. 18, pp. 530–535, 1964.

[110] S. Pöykkö and D. Chadi, "Ab initio study of 180 domain wall energy and structure in PbTiO$_3$," *Applied Physics Letters*, vol. 75, p. 2830, 1999.

[111] J. C. Wojdeł, P. Hermet, M. P. Ljungberg, P. Ghosez, and J. Íñiguez, "First-principles model potentials for lattice-dynamical studies: general methodology and example of application to ferroic perovskite oxides," *Journal of Physics: Condensed Matter*, vol. 25, no. 30, p. 305401, 2013.

[112] B. Meyer and D. Vanderbilt, "*Ab initio* study of ferroelectric domain walls in PbTiO$_3$," *Physical Review B*, vol. 65, p. 104111, Mar 2002.

[113] S. Stemmer, S. K. Streiffer, F. Ernst, and M. Rühle, "Atomistic structure of 90° domain walls in ferroelectric PbTiO$_3$ thin films," *Philosophical Magazine A*, vol. 71, no. 3, pp. 713–724, 1995.

[114] J. Seidel, L. W. Martin, Q. He, Q. Zhan, Y.-H. Chu, A. Rother, M. Hawkridge, P. Maksymovych, P. Yu, M. Gajek, *et al.*, "Conduction at domain walls in oxide multiferroics," *Nature Materials*, vol. 8, no. 3, pp. 229–234, 2009.

[115] A. Lubk, S. Gemming, and N. Spaldin, "First-principles study of ferroelectric domain walls in multiferroic bismuth ferrite," *Physical Review B*, vol. 80, no. 10, p. 104110, 2009.

[116] J. Seidel, P. Maksymovych, Y. Batra, A. Katan, S.-Y. Yang, Q. He, A. P. Baddorf, S. V. Kalinin, C.-H. Yang, J.-C. Yang, *et al.*, "Domain wall conductivity in La-doped BiFeO$_3$," *Physical Review Letters*, vol. 105, no. 19, p. 197603, 2010.

[117] S. Farokhipoor and B. Noheda, "Conduction through 71 domain walls in BiFeO$_3$ thin films," *Physical Review Letters*, vol. 107, no. 12, p. 127601, 2011.

[118] J. Guyonnet, I. Gaponenko, S. Gariglio, and P. Paruch, "Conduction at domain walls in insulating Pb(Zr$_{0.2}$Ti$_{0.8}$)O$_3$ thin films," *Advanced Materials*, vol. 23, no. 45, pp. 5377–5382, 2011.

[119] M. Y. Gureev, A. K. Tagantsev, and N. Setter, "Head-to-head and tail-to-tail 180 domain walls in an isolated ferroelectric," *Physical Review B*, vol. 83, no. 18, p. 184104, 2011.

[120] X. Wu and D. Vanderbilt, "Theory of hypothetical ferroelectric superlattices incorporating head-to-head and tail-to-tail 180° domain walls," *Physical Review B*, vol. 73, no. 2, p. 020103, 2006.

[121] K. Rahmanizadeh, D. Wortmann, G. Bihlmayer, and S. Blügel, "Charge and orbital order at head-to-head domain walls in $PbTiO_3$," *Physical Review B*, vol. 90, no. 11, p. 115104, 2014.

[122] P. Paruch, T. Giamarchi, and J.-M. Triscone, "Domain wall roughness in epitaxial ferroelectric $PbZr_{0.2}Ti_{0.8}O_3$ thin films," *Physical Review Letters*, vol. 94, no. 19, p. 197601, 2005.

[123] C. Becher, L. Maurel, U. Aschauer, M. Lilienblum, C. Magén, D. Meier, E. Langenberg, M. Trassin, J. Blasco, I. P. Krug, *et al.*, "Strain-induced coupling of electrical polarization and structural defects in $SrMnO_3$ films," *Nature Nanotechnology*, vol. 10, pp. 661–665, 2015.

[124] A. Von Hippel, "Ferroelectricity, domain structure, and phase transitions of barium titanate," *Reviews of Modern Physics*, vol. 22, no. 3, p. 221, 1950.

[125] G. Shirane and A. Takeda, "Phase transitions in solid solutions of $PbZrO_3$ and $PbTiO_3$ (i) small concentrations of $PbTiO_3$," *Journal of the Physical Society of Japan*, vol. 7, no. 1, pp. 5–11, 1952.

[126] G. Shirane, K. Suzuki, and A. Takeda, "Phase transitions in solid solutions of $PbZrO_3$ and $PbTiO_3$ (ii) x-ray study," *Journal of the Physical Society of Japan*, vol. 7, no. 1, pp. 12–18, 1952.

[127] E. Sawaguchi, "Ferroelectricity versus antiferroelectricity in the solid solutions of $PbZrO_3$ and $PbTiO_3$," *Journal of the Physical Society of Japan*, vol. 8, no. 5, pp. 615–629, 1953.

[128] B. Jaffe, R. Roth, and S. Marzullo, "Piezoelectric properties of lead zirconate-lead titanate solid-solution ceramics," *Journal of Applied Physics*, vol. 25, no. 6, pp. 809–810, 1954.

[129] M. Hammer and M. J. Hoffmann, "Detailed X-ray diffraction analyses and correlation of microstructural and electromechanical properties of La-doped PZT ceramics," *Journal of Electroceramics*, vol. 2, no. 2, pp. 75–84, 1998.

[130] M. Hammer and M. J. Hoffmann, "Sintering model for mixed-oxide-derived lead zirconate titanate ceramics," *Journal of the American Ceramic Society*, vol. 81, no. 12, pp. 3277–3284, 1998.

[131] A. Safari and E. K. Akdoğan, *Piezoelectric and acoustic materials for transducer applications*. Springer, 2008.

[132] R. Whatmore, "Pyroelectric devices and materials," *Reports on progress in physics*, vol. 49, no. 12, p. 1335, 1986.

[133] H. Takeuchi, S. Jyomura, E. Yamamoto, and Y. Ito, "Electromechanical properties of (Pb,Ln)(Ti,Mn)O ceramics (Ln= rare earths)," *The Journal of the Acoustical Society of America*, vol. 72, p. 1114, 1982.

[134] P. Erhart, P. Träskelin, and K. Albe, "Formation and switching of defect dipoles in acceptor-doped lead titanate: A kinetic model based on first-principles calculations," *Physical Review B*, vol. 88, p. 024107, Jul 2013.

[135] A. Nowick and W. Heller, "Dielectric and anelastic relaxation of crystals containing point defects," *Advances in Physics*, vol. 14, no. 54, pp. 101–166, 1965.

[136] G. Henkelman, B. P. Uberuaga, and H. Jónsson, "A climbing image nudged elastic band method for finding saddle points and minimum energy paths," *The Journal of Chemical Physics*, vol. 113, p. 9901, 2000.

[137] G. Dai, P. Lu, X. Huang, Q. Liu, and W. Xue, "A study of Pb vacancies and Pb-O vacancy pairs in doped $Pb_{0.85}Sr_{0.15}(Zr_{0.55}Ti_{0.45})O_3$ ceramics by positron annihilation," *Journal of Materials Science: Materials in Electronics*, vol. 2, no. 3, pp. 164–170, 1991.

[138] E. Cockayne and B. P. Burton, "Dipole moment of a Pb-O vacancy pair in $PbTiO_3$," *Physical Review B*, vol. 69, p. 144116, Apr 2004.

[139] S. Pöykkö and D. J. Chadi, "First principles study of Pb vacancies in $PbTiO_3$," *Applied Physics Letters*, vol. 76, no. 4, pp. 499–501, 2000.

[140] R. A. Mackie, A. Peláiz-Barranco, and D. J. Keeble, "Vacancy defects in $PbTiO_3$ and lanthanide-ion-doped $PTiO_3$: A study of positron lifetimes," *Physical Review B*, vol. 82, p. 024113, Jul 2010.

[141] R.-A. Eichel, H. Mestric, H. Kungl, and M. J. Hoffmann, "Multifrequency electron paramagnetic resonance analysis of polycrystalline gadolinium-doped $PbTiO_3$—charge compensation and site of incorporation," *Applied Physics Letters*, vol. 88, no. 12, p. 122506, 2006.

[142] L. Jin, Z. He, and D. Damjanovic, "Nanodomains in Fe^{+3}-doped lead zirconate titanate ceramics at the morphotropic phase boundary do not correlate with high properties," *Applied Physics Letters*, vol. 95, no. 1, p. 012905, 2009.

[143] D. Lee, R. K. Behera, P. Wu, H. Xu, Y. Li, S. B. Sinnott, S. R. Phillpot, L. Chen, and V. Gopalan, "Mixed Bloch-Néel-Ising character of 180 ferroelectric domain walls," *Physical Review B*, vol. 80, no. 6, p. 060102, 2009.

[144] R. K. Behera, C.-W. Lee, D. Lee, A. N. Morozovska, S. B. Sinnott, A. Asthagiri, V. Gopalan, and S. R. Phillpot, "Structure and energetics of 180° domain walls in $PbTiO_3$ by density functional theory," *Journal of Physics: Condensed Matter*, vol. 23, no. 17, p. 175902, 2011.

[145] M. Taherinejad, D. Vanderbilt, P. Marton, V. Stepkova, and J. Hlinka, "Bloch-type domain walls in rhombohedral $BaTiO_3$," *Physical Review B*, vol. 86, no. 15, p. 155138, 2012.

Bibliography

[146] G. Sághi-Szabó, R. E. Cohen, and H. Krakauer, "First-principles study of piezoelectricity in PbTiO$_3$," *Physical Review Letters*, vol. 80, no. 19, p. 4321, 1998.

[147] A. A. Mostofi, J. R. Yates, Y.-S. Lee, I. Souza, D. Vanderbilt, and N. Marzari, "Wannier90: A tool for obtaining maximally-localised Wannier functions," *Computer Physics Communications*, vol. 178, no. 9, pp. 685–699, 2008.

[148] P. Yudin, A. Tagantsev, and N. Setter, "Bistability of ferroelectric domain walls: Morphotropic boundary and strain effects," *Physical Review B*, vol. 88, no. 2, p. 024102, 2013.

[149] J. Frantti, "Notes of the recent structural studies on lead zirconate titanate," *The Journal of Physical Chemistry B*, vol. 112, no. 21, pp. 6521–6535, 2008.

[150] H. Fu and R. E. Cohen, "Polarization rotation mechanism for ultrahigh electromechanical response in single-crystal piezoelectrics," *Nature*, vol. 403, no. 6767, pp. 281–283, 2000.

[151] D. Damjanovic, "A morphotropic phase boundary system based on polarization rotation and polarization extension," *Applied Physics Letters*, vol. 97, no. 6, p. 062906, 2010.

[152] Z. Li, M. Grimsditch, X. Xu, and S.-K. Chan, "The elastic, piezoelectric and dielectric constants of tetragonal PbTiO$_3$ single crystals," *Ferroelectrics*, vol. 141, no. 1, pp. 313–325, 1993.

[153] A. Kalinichev, J. Bass, B. Sun, and D. Payne, "Elastic properties of tetragonal PbTiO$_3$ single crystals by Brillouin scattering," *Journal of Materials Research*, vol. 12, no. 10, pp. 2623–2627, 1997.

[154] G. Arlt and H. Neumann, "Internal bias in ferroelectric ceramics: Origin and time dependence," *Ferroelectrics*, vol. 87, no. 1, pp. 109–120, 1988.

[155] J. Scott and M. Dawber, "Oxygen-vacancy ordering as a fatigue mechanism in perovskite ferroelectrics," *Applied Physics Letters*, vol. 76, no. 25, pp. 3801–3803, 2000.

[156] W. A. Saidi, J. M. P. Martirez, and A. M. Rappe, "Strong reciprocal interaction between polarization and surface stoichiometry in oxide ferroelectrics," *Nano Letters*, vol. 14, no. 11, pp. 6711–6717, 2014.

[157] Z. Alahmed and H. Fu, "First-principles determination of chemical potentials and vacancy formation energies in PbTiO$_3$ and BaTiO$_3$," *Physical Review B*, vol. 76, p. 224101, Dec 2007.

[158] L. Hong, A. Soh, Q. Du, and J. Li, "Interaction of O vacancies and domain structures in single crystal BaTiO$_3$: Two-dimensional ferroelectric model," *Physical Review B*, vol. 77, no. 9, p. 094104, 2008.

[159] A. Chandrasekaran, D. Damjanovic, N. Setter, and N. Marzari, "Defect ordering and defect–domain-wall interactions in PbTiO$_3$: A first-principles study," *Physical Review B*, vol. 88, no. 21, p. 214116, 2013.

[160] M. Dawber and J. Scott, "Fatigue and oxygen vacancy ordering in thin-film and bulk single crystal ferroelectrics," *Integrated Ferroelectrics*, vol. 32, no. 1-4, pp. 259–266, 2001.

[161] E. Eliseev, A. Morozovska, G. Svechnikov, V. Gopalan, and V. Y. Shur, "Static conductivity of charged domain walls in uniaxial ferroelectric semiconductors," *Physical Review B*, vol. 83, no. 23, p. 235313, 2011.

[162] E. A. Eliseev, A. N. Morozovska, G. S. Svechnikov, P. Maksymovych, and S. V. Kalinin, "Domain wall conduction in multiaxial ferroelectrics," *Physical Review B*, vol. 85, no. 4, p. 045312, 2012.

[163] E. A. Eliseev, A. N. Morozovska, Y. Gu, A. Y. Borisevich, L.-Q. Chen, V. Gopalan, and S. V. Kalinin, "Conductivity of twin-domain-wall/surface junctions in ferroelastics: Interplay of deformation potential, octahedral rotations, improper ferroelectricity, and flexoelectric coupling," *Physical Review B*, vol. 86, no. 8, p. 085416, 2012.

[164] A. N. Morozovska, R. K. Vasudevan, P. Maksymovych, S. V. Kalinin, and E. A. Eliseev, "Anisotropic conductivity of uncharged domain walls in BiFeO$_3$," *Physical Review B*, vol. 86, no. 8, p. 085315, 2012.

[165] P. Maksymovych, J. Seidel, Y. H. Chu, P. Wu, A. P. Baddorf, L.-Q. Chen, S. V. Kalinin, and R. Ramesh, "Dynamic conductivity of ferroelectric domain walls in BiFeO$_3$," *Nano Letters*, vol. 11, no. 5, pp. 1906–1912, 2011.

[166] N. Balke, B. Winchester, W. Ren, Y. H. Chu, A. N. Morozovska, E. A. Eliseev, M. Huijben, R. K. Vasudevan, P. Maksymovych, J. Britson, *et al.*, "Enhanced electric conductivity at ferroelectric vortex cores in BiFeO$_3$," *Nature Physics*, vol. 8, no. 1, pp. 81–88, 2012.

[167] P. Maksymovych, A. N. Morozovska, P. Yu, E. A. Eliseev, Y.-H. Chu, R. Ramesh, A. P. Baddorf, and S. V. Kalinin, "Tunable metallic conductance in ferroelectric nanodomains," *Nano Letters*, vol. 12, no. 1, pp. 209–213, 2012.

[168] C.-L. Jia, S.-B. Mi, K. Urban, I. Vrejoiu, M. Alexe, and D. Hesse, "Atomic-scale study of electric dipoles near charged and uncharged domain walls in ferroelectric films," *Nature Materials*, vol. 7, pp. 57–61, Jan. 2008.

[169] Y. Tang, Y. Zhu, Y. Wang, W. Wang, Y. Xu, W. Ren, Z. Zhang, and X. Ma, "Atomic-scale mapping of dipole frustration at 90° charged domain walls in ferroelectric PbTiO$_3$ films," *Scientific Reports*, vol. 4, 2014.

[170] R. Waser, T. Baiatu, and K.-H. Härdtl, "DC Electrical Degradation of Perovskite-Type Titanates: II, Single Crystals," *Journal of the American Ceramic Society*, vol. 73, no. 6, pp. 1654–1662, 1990.

Bibliography

[171] R. Waser, "Bulk conductivity and defect chemistry of acceptor-doped strontium titanate in the quenched state," *Journal of the American Ceramic Society*, vol. 74, no. 8, pp. 1934–1940, 1991.

[172] W. Liu and C. A. Randall, "Thermally stimulated relaxation in Fe-Doped $SrTiO_3$ Systems: II. Degradation of $SrTiO_3$ Dielectrics," *Journal of the American Ceramic Society*, vol. 91, no. 10, pp. 3251–3257, 2008.

[173] Y. Cao, J. Shen, C. Randall, and L. Chen, "Phase-field modeling of switchable diode-like current-voltage characteristics in ferroelectric $BaTiO_3$," *Applied Physics Letters*, vol. 104, no. 18, p. 182905, 2014.

[174] A. Biancoli, C. M. Fancher, J. L. Jones, and D. Damjanovic, "Breaking of macroscopic centric symmetry in paraelectric phases of ferroelectric materials and implications for flexoelectricity," *Nature Materials*, vol. 14, no. 2, pp. 224–229, 2015.

[175] R. Lohkämper, H. Neumann, and G. Arlt, "Internal bias in acceptor-doped $BaTiO_3$ ceramics: Numerical evaluation of increase and decrease," *Journal of Applied Physics*, vol. 68, no. 8, pp. 4220–4224, 1990.

[176] S. Pöykkö and D. J. Chadi, "Dipolar defect model for fatigue in ferroelectric perovskites," *Physical Review Letters*, vol. 83, pp. 1231–1234, Aug 1999.

[177] J. Carrasco, F. Illas, N. Lopez, E. Kotomin, Y. F. Zhukovskii, R. A. Evarestov, Y. A. Mastrikov, S. Piskunov, and J. Maier, "First-principles calculations of the atomic and electronic structure of F centers in the bulk and on the (001) surface of $SrTiO_3$," *Physical Review B*, vol. 73, no. 6, p. 064106, 2006.

[178] P. Ghosez, E. Cockayne, U. V. Waghmare, and K. M. Rabe, "Lattice dynamics of $BaTiO_3$, $PbTiO_3$, and $PbZrO_3$: A comparative first-principles study," *Physical Review B*, vol. 60, pp. 836–843, Jul 1999.

[179] H. Wieder, "Electrical behavior of barium titanate single crystals at low temperatures," *Physical Review*, vol. 99, no. 4, p. 1161, 1955.

[180] C. Brennan, "Model of ferroelectric fatigue due to defect/domain interactions," *Ferroelectrics*, vol. 150, no. 1, pp. 199–208, 1993.

[181] A. Alkauskas, P. Broqvist, and A. Pasquarello, "Defect energy levels in density functional calculations: Alignment and band gap problem," *Physical Review Letters*, vol. 101, no. 4, p. 046405, 2008.

[182] H.-P. Komsa, T. T. Rantala, and A. Pasquarello, "Finite-size supercell correction schemes for charged defect calculations," *Physical Review B*, vol. 86, p. 045112, Jul 2012.

[183] I. Grinberg, D. V. West, M. Torres, G. Gou, D. M. Stein, L. Wu, G. Chen, E. M. Gallo, A. R. Akbashev, P. K. Davies, *et al.*, "Perovskite oxides for visible-light-absorbing ferroelectric and photovoltaic materials," *Nature*, vol. 503, no. 7477, pp. 509–512, 2013.

Curriculum vitae and publications

Name: Anand

Surname: Chandrasekaran

Date of birth: 19 August 1988

Nationality: Indian

Education

2011 – 2015   PhD Student, Theory and Simulation of Materials (THEOS)/Ceramics Laboratory (LC), École Polytechnique Fédérale de Lausanne, Switzerland

2006-2011   Bachelors and Masters in Metallurgical and Materials Engineering, Indian Institute of Technology Madras, Chennai, India

Conference talks and posters

1. German Physical Society meeting (DPG), Regensburg, Germany, March 2013 – "Defect ordering in $PbTiO_3$"

2. ISAF-IEEE meeting, Prague , Czech Republic, July 2013 – "Defect ordering in $PbTiO_3$"

3. German Physical Society meeting (DPG), March, Dresden, Germany, March 2014 – "Bloch walls in $PbTiO_3$"

4. PSI-K conference, San Sebastien, Spain, September, 2015 –"Defect/domain wall interactions in $PbTiO_3$"

Poster awards

1. Best poster award EDMX Research Day, EPFL, Switzerland, September 2013 -"Defect ordering in $PbTiO_3$"

2. Best poster award, "Nothing is perfect – the quantum mechanics of defects", Ascona, Monte Verità, Switzerland, 2015 – "Defect/domain wall interactions in $PbTiO_3$"

Schools attended

1. Hermes summer school on materials modelling and science communication, London, UK, July, 2012

2. Psi-k/CECAM/CCP9 Biennial Graduate School in Electronic-Structure Methods, Oxford, UK, September, 2013

Publications

1. "Defect ordering and defect-domain wall interactions in $PbTiO_3$: A first-principles study", Anand Chandrasekaran, Dragan Damjanovic, Nava Setter and Nicola Marzari, *Physical Review B , 88, 214116 (2013)*

2. "Oxygen vacancies interactions and 180° charged domain walls in $BaTiO_3$", Anand Chandrasekaran, Dragan Damjanovic, Nava Setter and Nicola Marzari, *Submitted to Applied Physics Letters*

3. "Asymmetric structure of 90° domain walls and interactions with defects in $PbTiO_3$", Anand Chandrasekaran, Dragan Damjanovic, Nava Setter and Nicola Marzari, *To be submitted, December 2015*